Microgravity Scaling Theory Experiment

MISTE

Science Requirements Document

October 18, 2000

MICROGRAVITY SCALING THEORY EXPERIMENT
SCIENCE REQUIREMENTS DOCUMENT

Approved by:

Bradley Carpenter
Lead Enterprise Scientist
NASA Microgravity Research Division
(HQ, Code UG)

Concurred:

Martin Barmatz

Dr. Martin Barmatz
Principal Investigator
MISTE Experiment
Section 354, Jet Propulsion Laboratory

Melora Larson

Dr. Melora Larson
Project Scientist, LTMPF M1 Mission
Low Temp. Science and Engineering Group
Section 354, Jet Propulsion Laboratory

Ulf Israelsson

Dr. Ulf E. Israelsson
Fundamental Physics Discipline Scientist
Space and Earth Science Programs Directorate
Jet Propulsion Laboratory

Mark C. Lee

Dr. Mark Lee
Fundamental Physics Enterprise Scientist
NASA Microgravity Research Division
(HQ, Code UG)

John Pensinger
Program Manager, LTMPF
Space and Earth Science Programs Directorate
Jet Propulsion Laboratory

Fred O'Callaghan
Program Manager, SSFE Office
Space and Earth Science Programs Directorate
Jet Propulsion Laboratory

Prepared by: M. Barmatz
Jet Propulsion Laboratory
California Institute of Technology
October 18, 2000

JPL Document # D-17083

Table of Contents

EXECUTIVE SUMMARY *3*

1. INTRODUCTION *5*

1.1. Critical Phenomena/Liquid-Gas Critical Point 5
1.2. Need for Microgravity 12

2. EXPERIMENT OBJECTIVES *18*

2.1. Measurements of the Critical Amplitudes and Exponents 19
2.2. Test of the Homogeneity Postulate and Scaled Equation-of-State 21

3. SCIENCE REQUIREMENTS *22*

3.1. Experimental Cell 24
3.2. Temperature Sensor 26
3.3. Density Sensor 27
3.4. Pressure Sensor 28
3.5. In-Situ Fluid Transfer System 29
3.6. Determination of Critical Density and Temperature 31
3.7. Equilibrium Time Constants and Density Stratification 33
3.8. Charged-Particle and Vibration Environment 35
3.9. Heat Capacity Measurement 43
3.10. Susceptibility Measurement 48

4. EXPERIMENT TIMELINE AND DATA ACQUISITION *55*

4.1. Measurement Plan 55
4.2. Data Requirements 57
4.3. Mission Success Criteria 58

5. REFERENCES *59*

6. APPENDICES *62*

A. Equations-of-State 62
B. Analysis of Susceptibility Measurements 72
C. Density Stratification 82

EXECUTIVE SUMMARY

The goal of the MISTE (MIcrogravity Scaling Theory Experiment) is to provide a stringent test of scaling theory predictions for critical behavior near a liquid-gas critical point both in the asymptotic and crossover regions. The introduction of the homogeneous postulate for the singular part of thermodynamic quantities has led to a set of scaling relations between the critical exponents that describe the expected leading and confluent power law divergences. The application of Renormalization Group (RG) theory to the study of critical points has provided a fundamental justification for the scaling relations. This RG theory has been used to calculate accurate values of the critical exponents and universal asymptotic amplitude ratios for a wide range of universality classes. The most recently calculated values for these exponents are believed to be highly accurate, and a majority of the scientific community is confident that these predictions correctly describe the asymptotic behavior of these systems. However, the situation is less well understood regarding the asymptotic amplitude ratios and the behavior in the crossover region where critical fluctuations no longer dominate the behavior of the system.

The last several decades have witnessed widespread efforts to test theoretical predictions near critical points. In the early years emphasis was placed on theoretical and experimental studies of the liquid-gas critical point because of the fact that this system permitted the measurement of a wide variety of thermophysical properties within the critical region. This is in contrast to the lambda point in liquid ^{4}He, where certain thermophysical quantities, such as the order parameter and its conjugate field, are not physically accessible because of the quantum-mechanical nature of the superfluid wave function. Unfortunately, the liquid-gas critical point is subject to limitations resulting from the effects of gravity. In this system, gravity couples directly to the order parameter, which is the difference between the system's density and the critical density. In the earth's gravitational field, gravity induces a density stratification in a fluid layer of finite vertical height, and this stratification interferes with precision measurements close to the transition. For example, measurements along the critical isochore, even in a small vertical height cell of 0.05 cm, are affected by gravity within a reduced temperature of $|t| \equiv |(T-T_c)/T_c| \leq 10^{-4}$. The asymptotic region, where the leading singular term dominates the divergence of thermophysical properties, occurs in the same reduced temperature range. The overlap of these two regions has severely limited the experimentalist's ability to accurately test theoretical predictions. It is for these reasons that MISTE was proposed to perform a set of thermodynamic measurements very close to the liquid-gas critical point of ^{3}He in a microgravity environment.

The MISTE flight experiment plans to perform specific heat at constant volume, C_V, isothermal susceptibility, χ_T, and *PVT* measurements in the same experimental cell. This approach will minimize previous systematic errors, associated with performing various thermodynamic measurements in different apparatuses, by determining a self-consistent set of critical-point parameters (P_c, ρ_c, and T_c). In the microgravity experiment, we propose to extend the same thermodynamic measurements preformed on the ground to the region closer to the transition. Our objective is to obtain gravity-free measurements at least two decades in reduced temperature closer to the transition than can be obtained on the ground. This measurement region will still be bracketed by gravity rounding close to the transition, and a departure from the asymptotic critical behavior with crossover into the classical regime farther away from the transition. Measurements along the theoretically important critical isochore and critical isotherm will be emphasized. The quality of the data very close to the transition will be tested by comparing the critical exponents α, γ, and δ obtained from a best-fit procedure with theoretical scaling predictions. Then the leading asymptotic critical amplitudes of C_V and χ_T measured along critical paths will be determined while fixing the critical exponents.

The microgravity experiments should permit an accurate determination of the nonuniversal asymptotic critical amplitudes associated with the ^{3}He liquid-gas critical point. Knowledge of these asymptotic amplitudes can then be used to test universal amplitude ratio predictions as well as provide a more accurate analysis of crossover measurements farther away from the transition. This analysis of measurements throughout the critical region should permit a stringent test of the predictions of recent crossover theories. In addition, the specific heat and susceptibility data coupled with the *PVT* data will be used to test recent theoretical predictions for the scaled equation-of-state in both the asymptotic and crossover regions. The measurements obtained from MISTE will also serve as a guide to those who are engaged in further development of crossover models.

The singularities of thermophysical quantities in the critical region lead to a “critical slowing down” effect. The consequence of this effect is that the time to reach thermodynamic equilibrium becomes very long as the critical point is approached. Because of this effect, a long-duration flight experiment will be necessary to accurately measure the proposed thermodynamic quantities in the critical region. The estimated time to perform these measurements is much longer than can be provided by the Space Shuttle and will require the use of the International Space Station for 3 to 5 months.

During the last several years, ground-based studies in the critical region of ^{3}He were performed at the Jet Propulsion Laboratory to validate the precision of the proposed experimental techniques for achieving the objectives of the MISTE flight experiment. The results of these studies and the status of our scientific readiness for flight are presented. The science requirements for the flight experiment and any additional planned ground-based science and engineering studies are also discussed.

1. INTRODUCTION

In this section we present a brief introduction to critical phenomena, the importance of the liquid-gas critical point in testing theories, and the motivation for performing experiments in microgravity.

1.1 Critical Phenomena/Liquid-Gas Critical Point

Phase transitions are ubiquitous in nature and the investigation of these phenomena is important in understanding the nature of the universe. A significant subset of all phase transitions is the continuous or "critical point" phase transition. Critical points differ from first–order transitions in several respects. In the first place there is no discontinuity in the first derivatives of the thermodynamic potentials. One such discontinuity is associated with latent heat. Furthermore, continuous phase transitions do not exhibit irreversibility in the form of hysteresis. A key feature of the continuous phase transition is scale-invariance, which implies continuity between large and small scales associated with the transition. Scale-invariance occurs in many systems that are still not completely understood, such as the universe at the onset of the big bang as currently envisioned by cosmologists, the clustering of galaxies, massless fields in elementary particle physics, the distribution of earthquakes, and turbulence in fluids and plasmas. In each of these examples there is a wide range of scales over which some phenomena vary as a power law of the scale. The Renormalization Group (RG) theory [1] is the most successful approach thus far developed to derive and explore the relations between the characteristics of a system as viewed on different length scales.

Critical phenomena, associated with continuous phase transitions, can be described on a variety of levels [2,3]. We will discuss these levels in the context of thermophysical behavior near the liquid-gas critical point. First, there is the fact that thermophysical quantities exhibit power law behavior near critical points. This power law behavior depends on the paths approaching the critical point as shown in Figure 1. For example, the isothermal susceptibility diverges as $\chi_T \propto \Gamma_0^+ t^{-\gamma}$ along the path of the critical isochore, $\rho = \rho_c$, above the transition and as $\chi_T \propto \Gamma_0^- t^{-\gamma'}$ along the coexistence curve below the transition. $\Gamma_0^\pm$ are the leading asymptotic critical amplitudes, with the superscript ± defining the single (+) or two-phase (–) regions. By contrast, the constant-volume specific heat takes on the asymptotic power law form of $C_V \propto A_0^+ t^{-\alpha}$ along the critical isochore above T_c and $C_V \propto A_0^- t^{-\alpha'}$ below T_c. Here the quantities α α', γ, and γ' are known as critical exponents. Along the critical isotherm, $T = T_c$, the variation of pressure with density is given by $\Delta P \propto D\Delta\rho|\Delta\rho|^{\delta-1}$ where $\Delta P = (P - P_c)/P_c$ is the reduced pressure, $\Delta\rho = (\rho - \rho_c)/\rho_c$ is the reduced density and δ is the critical exponent that describes this singular behavior. In the two-phase region, the coexistence curve can be described as $\Delta\rho_{L,V} \equiv (\rho_{L,V} - \rho_c)/\rho_c \propto B_0(-t)^\beta$, where L and V correspond to the liquid and vapor phases respectively. The latest RG predictions for the critical exponents obtained from a 7-loop calculation [4] are [1]

---

[1] High-temperature series [5] predicts $\alpha = 0.105 \pm 0.007$ and $\gamma = 1.2395 \pm 0.0004$.

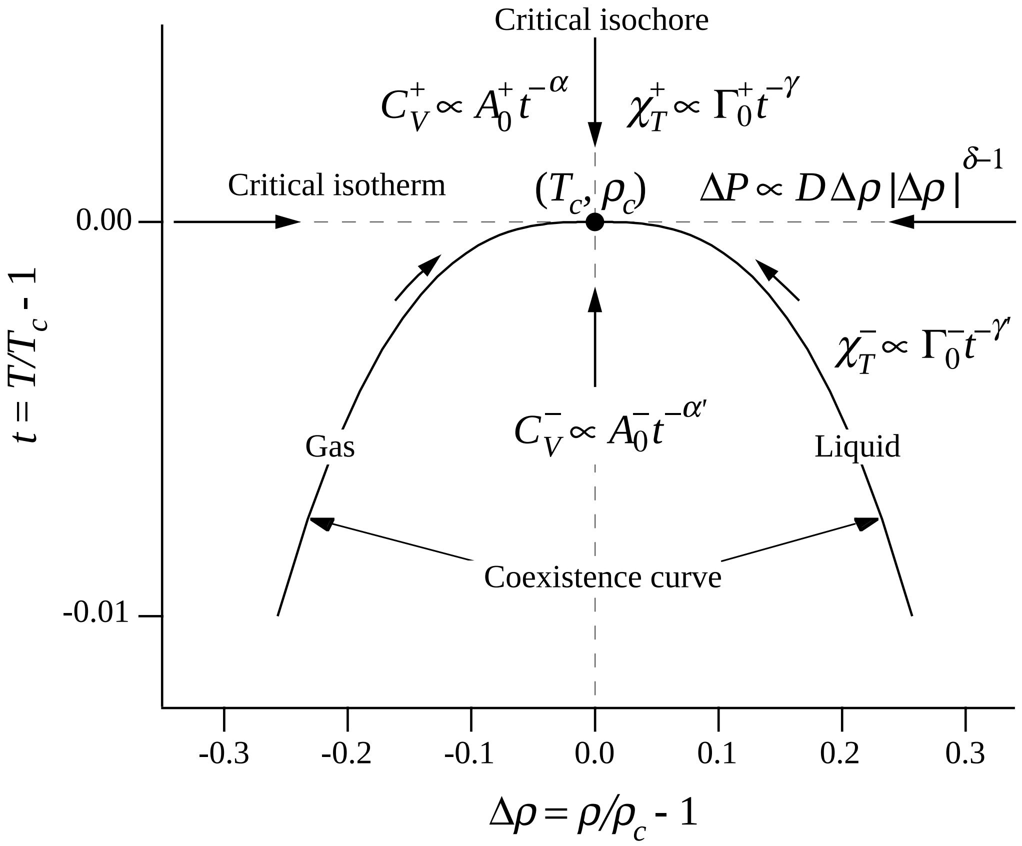
Critical isochore
$C_V^+ \propto A_0^+ t^{-\alpha}$
$\chi_T^+ \propto \Gamma_0^+ t^{-\gamma}$
Critical isotherm
(T_c, ρ_c)
$\Delta P \propto D \Delta\rho\, |\Delta\rho|^{\delta-1}$
0.00
-0.01
$t = T/T_c - 1$
$\chi_T^- \propto \Gamma_0^- t^{-\gamma'}$
$C_V^- \propto A_0^- t^{-\alpha'}$
Gas
Liquid
Coexistence curve
-0.3
-0.2
-0.1
0.0
0.1
0.2
0.3
$\Delta\rho = \rho/\rho_c - 1$

Fig. 1. Schematic representation of the critical region in the T, ρ plane.

$$\alpha = 0.109 \pm 0.004, \tag{1}$$

$$\gamma = 1.2396 \pm 0.0013, \tag{2}$$

$$\delta = 4.8055 \pm 0.0119, \tag{3}$$

$$\beta = 0.3258 \pm 0.0014, \tag{4}$$

with $\alpha = \alpha'$ and $\gamma = \gamma'$. In addition, the RG approach is able to calculate values for a number of universal asymptotic amplitude ratios. The amplitude ratios that are important for the MISTE flight experiment are [6]:

$$A_0^+ / A_0^- = 0.523 \pm 0.009$$[2]

$$\Gamma_0^+ / \Gamma_0^- = 4.95 \pm 0.15$$

$$\alpha A_0^+ \Gamma_0^+ / B_0^2 = 0.0581 \pm 0.0010$$

$$D \Gamma_0^+ B_0^{\delta-1} = 1.57 \pm 0.23 \tag{5}$$

The experimentally observed power law singularities in critical phenomena led to the formulation of the homogeneity postulate [3]. This postulate assumes that the singular part of diverging thermodynamic properties is a generalized function of the reduced temperature and reduced density. This hypothesis is intimately linked to the scaled equation-of-state (see

---

[2] A 3-D analysis yields $A_0^+ / A_0^- = 0.537 \pm 0.019$ [4].

Appendix A). Various researchers have developed scaled equations-of-state based on the RG [7]. These equations-of-state, which are meant to apply in the asymptotic critical region, have the expected scaling form, and they also make specific predictions for the curves on which thermodynamic functions will lie as one measures them along trajectories in the phase diagram. The best current predictions [7] for the equation-of-state of the liquid-gas system based on RG methods are not as precise as the results for critical exponents.

The homogeneity postulate leads to relations between critical exponents at the next level of critical phenomena. These relations are called scaling laws. This postulate claims that only two critical exponents are independent. A well-known scaling law example is the relation

$$\alpha + 2\beta + \gamma = 2. \tag{6}$$

This scaling relation allows one to determine the critical exponent β if the values of α and γ are already known.

Finally, there are the hyperscaling relations, in which the critical exponents are predicted to depend in specified ways on the behavior of spatial correlations in the system and on the system's spatial dimensionality d. An example of a hyperscaling law is

$$\delta = \frac{d+2-\eta}{d-2+\eta} \; . \tag{7}$$

The exponent η describes the power-law behavior of the two-point correlation function (a fluctuation-response relation) at the critical point. It has the value

$$\eta = 0.0335 \pm 0.0025 \tag{8}$$

obtained from a 7-loop calculation [4]. Another typical hyperscaling relation, namely the Josephson's relation, is given by

$$\alpha = 2 - d\nu, \tag{9}$$

where ν is the critical exponent for the correlation length, $\xi \propto t^{-\nu}$ with the value

$$\nu = 0.6304 \pm 0.0013 \tag{10}$$

obtained from a 7-loop calculation [4]. Using the fundamental relationship between the susceptibility and the correlation function and Eq. (7), we arrive at another hyperscaling relation

$$\gamma = \nu(2 - \eta). \tag{11}$$

By combining Eqs. (9) and (11), one obtains

$$\frac{2-\alpha}{\gamma} = \frac{d}{2-\eta} = 1.52555 \pm 0.00194 \; , \tag{12}$$

which is evaluated for a liquid-gas critical point using Eq. (8) and d = 3. The substitution of η in Eq. (12) and using Eq. (7) leads to the following scaling relation between α, γ, and δ,

$$\frac{2-\alpha}{\gamma} = \frac{\delta+1}{\delta-1} \; . \tag{13}$$

At all three levels of critical phenomena (power laws, scaling relations, and hyperscaling relations), the RG theory supplies the intellectual justification for observed and conjectured relationships. In fact, the formulation of the RG theory [1] presupposes the existence of the above three classes of phenomena. At this time, both theoreticians and experimentalists widely believe in the validity of RG predictions for the asymptotic behavior in most, if not all, systems exhibiting critical-point behavior. The experimental analysis of the C_V and χ_T data obtained from MISTE can be used to estimate the three asymptotic exponents α, γ, and δ. A test of the quality of the MISTE data in the asymptotic region will come from a comparison to the theoretical predictions given in Eqs. (1 - 3) and Eq. (13). Furthermore, the analysis of the MISTE data will provide more accurate values for the leading asymptotic critical amplitudes that can be used to test the theoretical amplitude ratio predictions given in Eq. (5).

An exact determination of the asymptotic region cannot be made theoretically because the leading critical amplitudes are system dependent, and there are additional correction-to-scaling confluent singularities that also contain system-dependent amplitudes. Furthermore, most experimental measurements performed on the ground appear to be outside the asymptotic region. Because of these facts, the theoretical community has used RG theory to develop confluent singularity corrections to the asymptotic behavior [8-11]. In real fluids, other nonasymptotic corrections due to liquid-vapor asymmetry in the coexistence curve [12] and analytic background terms also come into play. Taking into account these correction-to-scaling terms leads to the following theoretical expressions:

$$C_V^{\pm^*} \equiv \left(T_c\rho_c/P_c\right)C_V^{\pm} = A_0^{\pm}\,|\,t\,|^{-\alpha}\left[1+A_1^{\pm}\,|\,t\,|^{\Delta_s}+\ldots\right]+A_a^{\pm}\,|\,t\,|^{\gamma-2\alpha}+B_{sh} \tag{14}$$

$$\chi_T^{\pm^*} \equiv \left(P_c/\rho_c^2\right)\chi_T^{\pm} = \Gamma_0^{\pm}\,|\,t\,|^{-\gamma}\left[1+\Gamma_1^{\pm}\,|\,t\,|^{\Delta_s}+\ldots\right]+\Gamma_a^{\pm}\,|\,t\,|^{-\alpha}+B_\chi \tag{15}$$

$$\left(\Delta\rho^*\right)_{cxc} \equiv \left(\rho_{L,V}-\rho_c\right)/\rho_c = \pm B_0\,|\,t\,|^{\beta}\left[1+B_1\,|\,t\,|^{\Delta_s}+\ldots\right]+B_a t\,|\,t\,|^{-\alpha} \tag{16}$$

where B_{sh} and B_χ are background terms and B_a is the coefficient of the singular diameter of the coexistence curve [13],

$$\left(\rho_L+\rho_V\right)/2\rho_c = B_a t\,|\,t\,|^{-\alpha}\,. \tag{17}$$

The confluent singularity expansion in the brackets, commonly referred to as the Wegner expansion, includes a new independent universal correction-to-scaling exponent [10,11], $\Delta_s = 0.52 \pm 0.03$. It is generally assumed that the first Wegner correction-to-scaling terms, $A_1^{\pm}$, $\Gamma_1^{\pm}$, and B_1 cover the experimental range $10^{-3} \leq |t| \leq 10^{-2}$. In the case of the specific heat, the background term consists of two terms [14,15]:

$$B_{sh} = B_{cr} + B_{sh0}\,, \tag{18}$$

where B_{cr} is a constant, fluctuation-induced term associated with the critical singularity in C_V and B_{sh0} is the specific heat analytic background term. It is important to note that in ^{3}He, Brown and Meyer [16] found that the total background term B_{sh} is 0.0 ± 0.5, while in SF_6 that term is 19.92 ± 0.2 [17]. Thus, it appears that for ^{3}He, the critical part of the background is essentially equal and opposite to the analytic part. There is also a higher-than-linear term in the analytic expansions that is associated with the asymmetry in the coexistence curve. However, the coexistence curve of ^{3}He is the most symmetric of all the pure fluids [18], the rectilinear diameter being ~ 30 times smaller than the room-temperature critical-point fluids CO_2, SF_6, and Xe. Thus, we expect the magnitude of this asymmetric term to be small for the case of ^{3}He and it was not included in Eq. (16).

The system-dependent correction-to-scaling amplitudes also enter into universal amplitude ratios [11,19]

$$A_1^+ / \Gamma_1^+ = 0.9 \pm 0.1 \tag{19}$$

$$B_1^+ / \Gamma_1^+ = 0.8 \pm 0.2 \tag{20}$$

and [20]

$$-A_a^+ \Gamma_0^+ = A_0^+ \Gamma_a^+ = (1-\alpha)^2 B_a^2 . \tag{21}$$

It is clear from Eqs. (14 - 16) that there are a large number of adjustable parameters that need to be defined experimentally. Even with high-precision ground-based data, the ability to define these parameters is limited. By going to a microgravity environment, it is possible to obtain a sufficient amount of new data closer to the transition to permit a determination of the asymptotic critical parameters and amplitudes without considering data in the crossover region. In this way, the data farther away from the transition in the crossover region can then be analyzed using a reduced number of adjustable parameters.

In principle, the Wegner expansion can define the crossover from the asymptotic scaling region to classical mean field behavior. However, it is impractical to experimentally measure the amplitudes associated with higher-order Wegner terms. Because of this, other theoretical approaches have been studied to define crossover behavior. See Appendix A for a more detailed discussion of the presently available crossover models. Most of these approaches are based on the RG theory. Of particular interest to the MISTE experiment is the field-theoretical RG theory based on the ϕ^4 model developed by V. Dohm and coworkers [21]. This model extends the Ginzburg-Landau-Wilson theory by including critical fluctuations. This field-theoretical approach has successfully been applied to the case of the lambda point [22], which is in the $O(2)$ universality class. Recently, theoretical expressions have also been developed [23] to apply this technique to the $O(1)$ universality class that contains the liquid-gas critical point.

The experimental systems best suited for the verification of critical phenomena theories are critical points in fluids. This is because measurements in solids are compromised by the inhomogeneities that are inevitably incorporated into them. By contrast, in fluids such imperfections are averaged away. Because of this, the most accurate and definitive determination of critical point properties are those that have been achieved in fluids. The most studied fluid critical points are the lambda transition in liquid helium and the liquid-gas critical point, which is present in all single-component fluids. With regard to the testing of critical point theories, it is important to understand the differences between these two systems. The simple liquid-gas system and superfluid helium represent two examples of so-called $O(n)$ models. The liquid-gas system is in the $O(1)$ universality class, while the lambda point is governed by the physics of the $O(2)$ model. For all its experimental advantages, such as minimal gravity effect and ideal thermal properties, the lambda point suffers from the shortcoming that the order parameter is a macroscopic wave function, and the thermodynamic field that couples directly to it (the analog of an external magnetic field in the case of a ferromagnet) does not exist. For example, there is no simple way to physically manipulate the superfluid wave function in such a way as to extract the discontinuity that is associated with the exponent β. Because of this, many scaling relations can never be tested at the lambda point. By contrast, all fields can be experimentally realized and manipulated in the case of the liquid-gas system, the order parameter of which is the difference between the system's density and the critical density. This allows for a systematic and complete investigation of the phase diagram in the vicinity of the critical point.

Table I. The critical exponents, obtained from the measurements of various simple fluids [24].

Exponents	Xe	SF_6	CO_2
α	0.11	0.08	0.10
β	0.329	0.321	0.321
γ	1.23	1.28	1.24
δ	4.74	4.99	4.85
η	0.05	-0	-0
T_c (˚C)	16.56	45.55	30.99

In the '70s, Moldover and others [24] carried out experimental measurements on various simple fluids near their respective critical points and obtained the experimental values of the critical exponents listed in Table I. These updated experiments removed earlier discrepancies between the critical exponents of the Ising model and experimental measurements. The convergence of these experimental results and theoretical predictions played an important role in the widespread acceptance of the RG predictions of asymptotic behavior. Indeed, the most often quoted theoretical values for critical exponents are those obtained through RG calculations (as opposed, for example, to the analysis of high-temperature series).

The opportunity to perform low temperature measurements in a microgravity environment has led to a renewed interest in testing critical phenomena theories. We have proposed the use of ^{3}He for studies in space. There are many advantages for choosing ^{3}He for future microgravity studies. First, ^{3}He has an extraordinarily symmetric coexistence curve. The rectilinear diameter of ^{3}He is the smallest among all the simple fluids [18]; thus, it most closely approaches the simplest models for the equation-of-state. Secondly, at low temperatures, all impurities are frozen out except ^{4}He, which is less than 1 part per million for commercially available ^{3}He gas. Probably the most important reason for considering ^{3}He is the fact that its liquid-gas critical point is very close to the lambda point. Over the last several decades, an advanced SQUID-based, high-resolution thermometer (HRT) was developed to perform microgravity measurements within a nanodegree (nK) of the lambda transition. We are now using this HRT technique to study the ^{3}He liquid-gas critical point. It is also important to note that at the ^{3}He critical point, $(T_c/P_c)(\partial P/\partial T)_V \sim 3.4$. Thus, a temperature resolution of even $\delta T/T \sim 10^{-8}$ will only introduce a pressure variation of $\delta P/P \sim 3\times10^{-8}$. This pressure variation will permit pressure measurements with much higher resolution than were attainable in previous studies where only microdegree resolution was achievable. Also, ^{3}He has the lowest temperature liquid-gas critical point of any fluid. Thus, there is the possibility that quantum effects may influence the system-dependent critical amplitudes and range of crossover behavior near the transition [25]. An additional motivation for choosing the ^{3}He critical point is the extensive ground-based studies of the static and dynamic properties carried out primarily by Horst Meyer's group at Duke University. In the '70s, his group systematically measured the thermodynamic properties of ^{3}He near its liquid-gas critical point [16,18,26]. One possible disadvantage for choosing ^{3}He is the strong gravity effect for this transition. However, as will be seen, the proposed microgravity experiment will significantly reduce the effect of gravity to such an extent that sensor resolution will actually be the limiting factor in obtaining data close to the transition.

1.2 Need For Microgravity

As we have seen, the consensus among most theoreticians and experimentalists is that the theoretically calculated asymptotic critical exponents are essentially correct. However, because of gravitational effects, ground-based measurements do not sufficiently extend into the asymptotic region to accurately determine the leading nonuniversal critical amplitudes. Without accurate knowledge of these leading amplitudes, it is very difficult to test models of the equation-of-state. Precision experimental measurements [24] have demonstrated that true asymptotic critical behavior often occurs only when the critical temperature is approached along the critical isochore within $|t| \leq 10^{-4}$. Unfortunately, the hydrostatic pressure in a liquid is not constant in a gravitational field and near the critical point, a gravity-induced density stratification becomes important for most measurements within $|t| \leq 10^{-4}$. Thus, gravity effects have precluded detailed experimental studies in the asymptotic region near liquid-gas critical points. The ability to perform measurements in a microgravity environment now make it possible to obtain data significantly closer to the transition; this will provide a more stringent test of asymptotic scaling theory as well as improve our understanding of theoretical predictions of crossover behavior.

Figure 2 illustrates the expected density profiles in a 0.05 cm high cell (present ground-based MISTE cell height) and a 4 cm high cell (nominal MISTE flight cell height) for various reduced temperatures with $\rho_{\text{avg}} = \rho_c$. The calculation uses the restricted cubic model with the latest parameters for ^{3}He [27]. As the temperature approaches its critical value, only the density at the middle of the cell remains at ρ_c. In 1g the density stratification, [ρ(bottom) - ρ(top)]/ρ(middle) is approximately 6% in a cell of height 0.05 cm at $t = 10^{-5}$ while in 3μg (expected Space Station environment) it is less than 0.7% in a cell of height 4 cm at $t = 10^{-7}$.

The variation in local density leads to a variation in local susceptibility, defined as $\chi_T \equiv \rho^2\kappa_T$, where κ_T is the isothermal compressibility. The susceptibility $\chi_T = \rho(\partial\rho/\partial P)_T = -(\partial\rho/\partial z)_T/g$, where the equation $(\partial P/\partial z)_T = -\rho g$ is used under the hydrostatic equilibrium condition. We define this "vertical" variation as $\Delta\chi_T = [\chi_T(\text{bottom}) - \chi_T(\text{mid})]/\chi_T(\text{mid})$, which is also a function of t, h, and g. The deviation of local density ρ (from ρ_c) also leads to a decrease in local specific heat $C_V(z)$. However, the situation is more complicated for the specific heat than for the susceptibility since the specific heat measurement introduces a temperature change that in turn can lead to a change in the density stratification. Figure 3 shows the calculated average specific heat for the ground-based cell of height 0.05 cm and the proposed flight cell of maximum effective height 4 cm (see Sec. 3.1) under both 1g and 3μg. In the presence of a gravitational field, the specific heat shows an initial increase as the transition is approached and then a severe rounding as the local specific heat and density stratification alter their respective dominant roles. The deviation from the specific heat of a homogeneous fluid is defined as $\Delta C_V = [C_V(\text{avg}) - C_V(\rho_c)]/C_V(\rho_c)$, which is a function of reduced temperature t, cell height h, and gravity g. For the present ground-based cell with height of 0.05 cm, the deviation in the measured C_V from $C_V(\rho_c)$ is greater than 1% for reduced temperatures less than $t_{\text{min}} = 1.6\times10^{-4}$ in 1g, while $t_{\text{min}} = 7\times10^{-7}$ for a 4 cm high cell in 3μg.

We see from Fig. 3 that ideally there are about two and a half additional decades in reduced temperature available for microgravity measurements. Under the right conditions, the

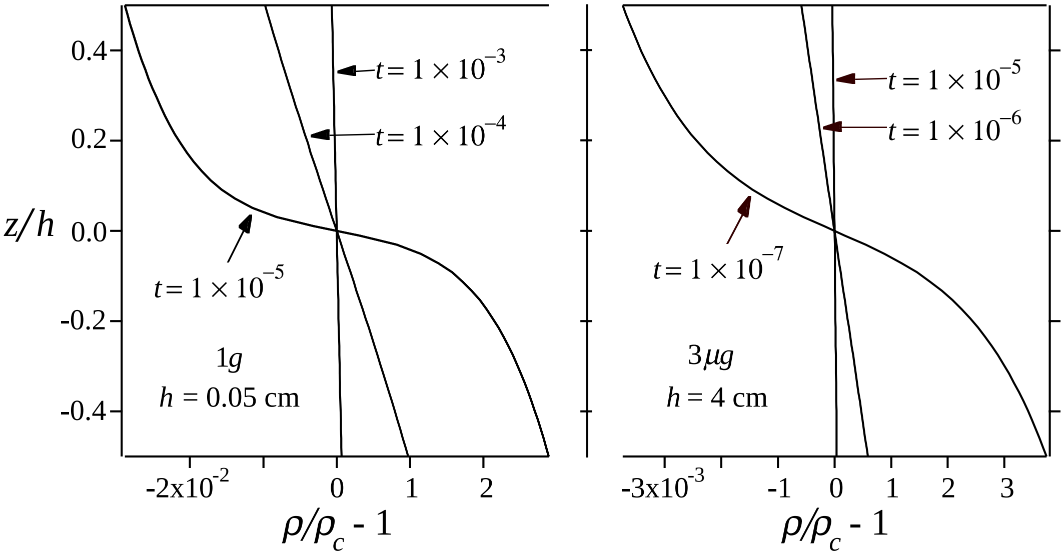

Fig. 2. Density profiles in 1*g* and 3μ*g* for a ^{3}He cell of height *h* = 0.05 cm and 4 cm respectively at $\rho_{\text{avg}} = \rho_c$. The *z* coordinate is in the direction opposite gravity.

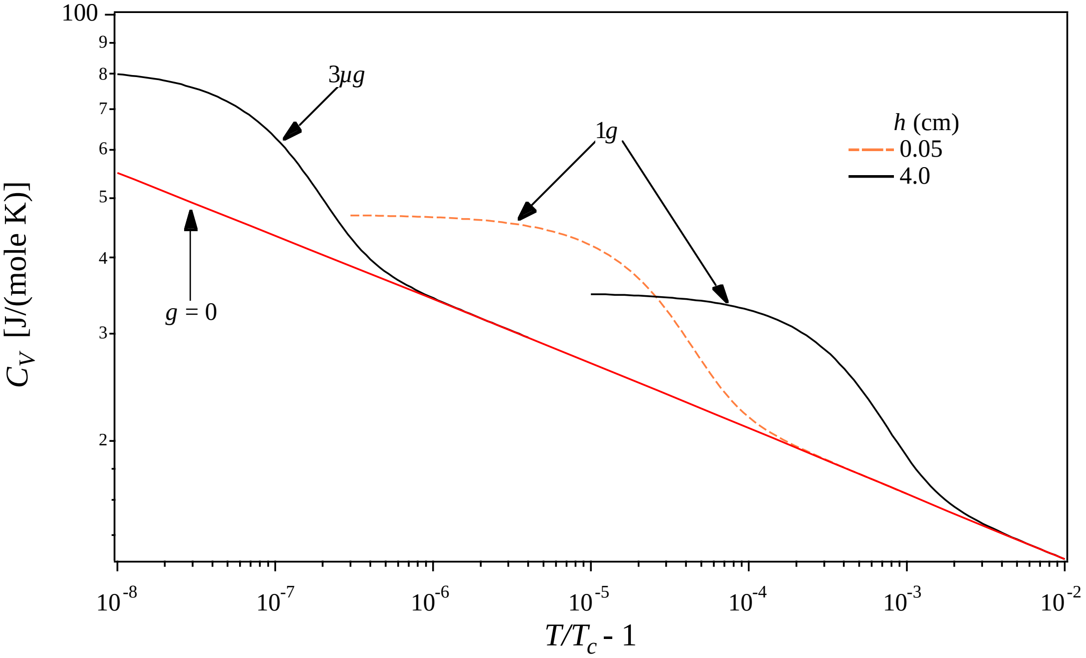

Fig. 3. The averaged specific heat at constant volume in 1*g* and 3μ*g* for a ^{3}He cell of 0.05 cm (dashed) and 4 cm (solid) height. Note the averaged C_V is proportional to the temperature derivative of the total entropy.

gravity–induced ΔC_V deviation expected in microgravity could be corrected using theory. This correction procedure is usually hampered by the fact that one does not have accurate a priori knowledge of the asymptotic critical amplitudes needed to precisely define equation-of-state parameters. However, an analysis of microgravity measurements could sufficiently validate equation-of-state models so that these models could be used to account for at least the initial gravity corrections.

Moldover et al. [28] have derived gravity-dependent expressions for calculating the reduced temperature, t_{min}, along the critical isochore and reduced density, $\Delta\rho_{\mathrm{min}}$, along the critical isotherm below which ΔC_V, $\Delta\chi_T$, and $[\Delta\rho(\mathrm{bottom}) - \Delta\rho(\mathrm{top})]/\Delta\rho(\mathrm{middle})$ are larger than a specified percentage. Their expressions show that t_{min} and $\Delta\rho_{\mathrm{min}}$ are functions of the product of (gh). We have applied the restricted cubic model with the latest parameters [27] for the ^{3}He critical point to calculate these deviations directly for various relevant dimensions, gravitational fields, and reduced temperatures. The results are shown in Figure 4. Figure 4a shows measurements along the critical isochore, and Fig. 4b shows measurements along the critical isotherm. The dashed lines separate the regions for deviations smaller than and larger than 1%. The horizontal lines correspond to the ground-based cell height, proposed flight cell height, and capacitor density sensor gap. The dotted line shows the temperature dependence of the correlation length. The height of the experimental cell and sensors are significantly greater than the correlation length to avoid finite size effects. Figures 4a and 4b are useful in estimating the expected gravity effect in proposed MISTE flight cells of various heights. We list in Table II the numerical values of the intersections of the dashed lines and relevant experimental dimensions (horizontal lines). These values are consistent with the ones calculated using the simple expressions by Moldover et al. [28].

The results shown in Figs. 2, 3, 4, and in Table II clearly demonstrate the need and the advantages of a low-gravity environment for performing accurate thermodynamic measurements along the critical isochore and critical isotherm in the asymptotic region near the critical point. Straub et al. measured the specific heat C_V of SF_6 at the critical density during the German Spacelab Mission D-2 in 1993 [17]. They extended the data range to $|t| = 3\times10^{-6}$ (a one and a half decade improvement) before gravity effects became important. The fit of the asymptotic experimental data over the range of $3\times10^{-6} \le |t| \le 1.6\times10^{-4}$ yielded $\alpha = \alpha' = 0.1105\ {+0.025}/{-0.027}$ and $A_0^- / A_0^+ = 1.919\ {+0.24}/{-0.27}$, which provided improved agreement with the RG predictions.

Table II. Calculated t_{min} ($\rho = \rho_C$) and $\Delta\rho_{\mathrm{min}}$ ($T = T_C$) for a gravity-induced 1% variation in various thermodynamic measurements in ^{3}He for $h = 0.05$ cm in 1g and $h = 4$ cm in 3μg.

t_{min}			$\Delta\rho_{\mathrm{min}}$	
Quantity	1g	**3μg**	1g	**3μg**
Specific Heat	1.6×10^{-4}	**7.4×10^{-7}**	-	-
Susceptibility	2.5×10^{-4}	**1.1×10^{-6}**	8.6×10^{-2}	**1.3×10^{-2}**
Susceptibility *	5.5×10^{-5}	**1.5×10^{-8}**	5.1×10^{-2}	**2.7×10^{-3}**
Density	1.8×10^{-4}	**1.7×10^{-8}**	7.6×10^{-2}	**1.4×10^{-2}**

* For capacitor density sensor gap $d = 5\times10^{-3}$ cm.

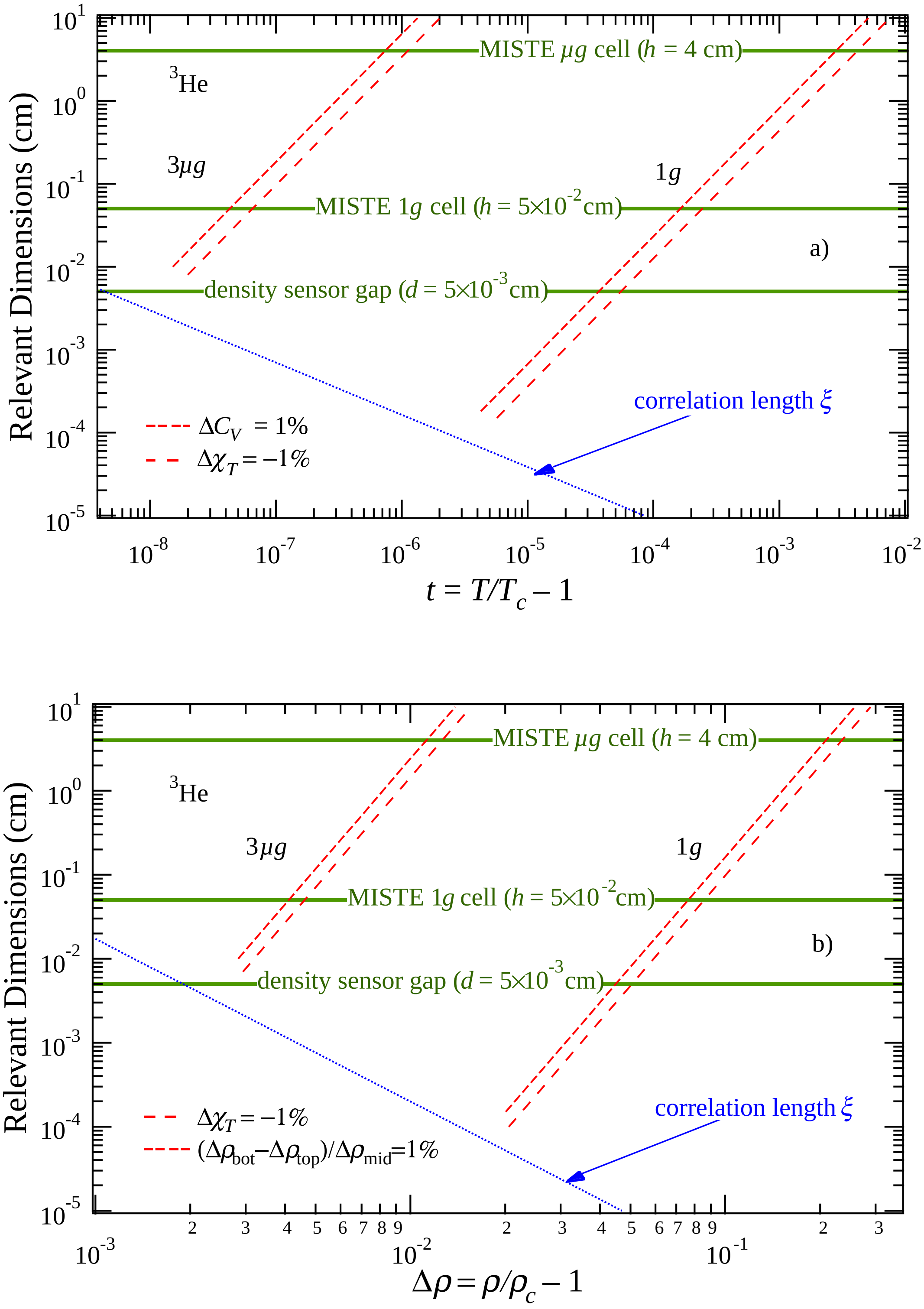

Fig. 4. a) 1% variation in C_V and χ_T in 1g and 3μg for $\rho_{\text{avg}} = \rho_c$. b) 1% variation in local $\Delta\rho$ and χ_T in 1g and 3μg along the critical isotherm.

Since the critical point can be approached closer under microgravity, a more accurate determination of the critical parameters P_c, ρ_c, and T_c is expected. In most experiments, these critical parameters are obtained by adjusting them in a least-square fit of one of the measured thermodynamic parameters. Gravity considerably reduces the accuracy of this determination and thus affects the accuracy to which the critical amplitudes can be determined. For $|t| \geq 10^{-4}$, one must also include the higher-order corrections-to-scaling terms. This introduces additional parameters that must be determined from fits to data and again leads to a less precise test of theory. By extending the experimental range closer to the transition, the asymptotic nonuniversal critical amplitudes could be determined with higher accuracy. Then the measurements farther from the transition can be analyzed to determine the crossover nonuniversal critical amplitudes using a reduced number of adjustable parameters.

Figure 5 shows another way to visualize the benefits of performing measurements in microgravity. The boundary for the asymptotic region (solid curve) was obtained from the restricted cubic model [27] assuming that along the critical isochore, higher-order terms in the susceptibility contribute a 1% correction to the leading asymptotic divergent term at $t = 10^{-4}$. The boundary for the earth's gravity-affected region (dot-dashed curve) was similarly obtained for a cell height of 0.05 cm assuming a 1% gravity correction at $t = 2\times10^{-4}$ along the critical isochore. The dashed curve is the coexistence curve. We see from Fig. 5 that along the critical isotherm ($t = 0$), gravity effects on the ground limit ^{3}He critical point measurements to $|\Delta\rho| \geq$ 3.8%. The MISTE flight experiment will be able to perform measurements throughout the

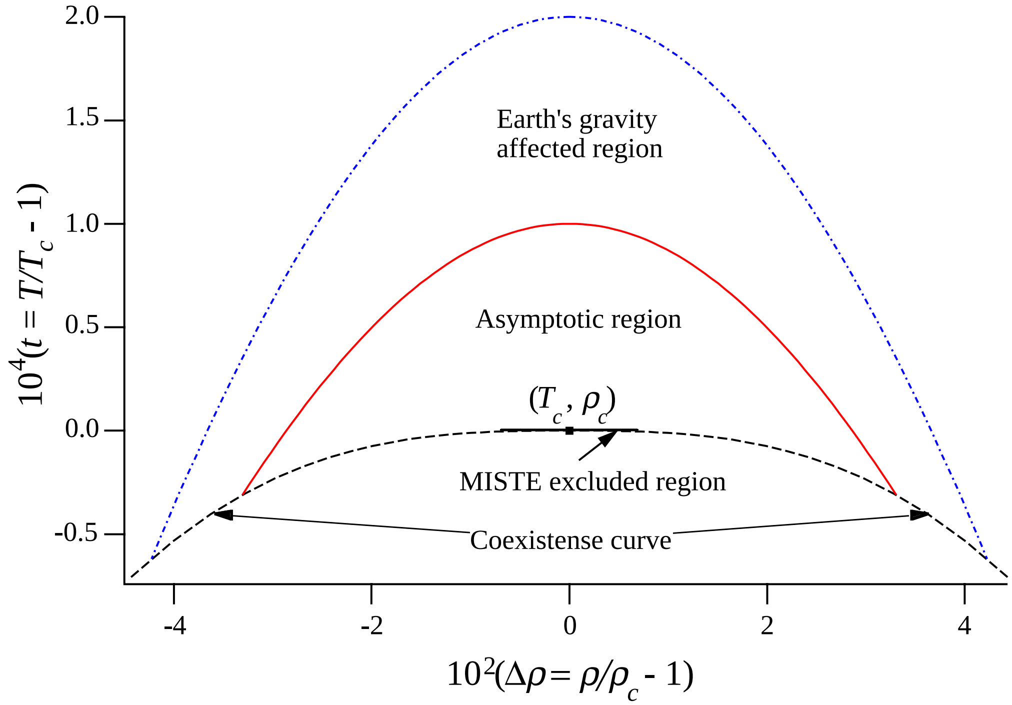

Fig. 5. Illustration of the earth's gravity-affected region, asymptotic region, and MISTE excluded region (thin, small, horizontal line) in the one-phase region near the ^{3}He critical point.

single–phase region except in an experimentally inaccessible region approximated by the small horizontal line very near the critical point ($t \leq 10^{-6}$, $\Delta\rho \leq 0.01$). The limiting effect of gravity shown in this figure clearly demonstrates the advantages of performing measurements in a microgravity environment. It is important to note that the “critical slowing down” effect leads to very long equilibration times as the critical point is approached. Thus, a long duration space flight will be needed to perform the wide variety of experiments being proposed. A detailed discussion of the expected relaxation times is given in subsection 3.7.

To summarize, the ^{3}He liquid-gas critical point is an ideal system to perform measurements in microgravity to test the predictions of the RG and the general notion of power laws and scaling. As a consequence, a microgravity investigation will constitute the most severe test of the validity of predictions regarding critical point behavior. Models and insights based on scaling now pervade physics, and the calculation techniques based on the RG are widespread. Scaling and RG theory have conditioned the way in which physicists and other scientists view the world. It is important to validate the RG asymptotic predictions as well as predictions for the crossover region.

2. EXPERIMENT OBJECTIVES

The main objective of the MISTE flight experiment is to test the scaling predictions of critical phenomena theories near the liquid-gas critical point by measuring with high precision several thermodynamic properties in the same experiment. The specific objectives of the experiment are:

1. Perform measurements of the specific heat at constant volume, C_V, in the single-phase region along isochores ($|\Delta\rho| \leq 10^{-1}$) over the reduced temperature range of $10^{-6} \leq t \leq 10^{-1}$. In the two-phase region, measurements will be performed over the reduced temperature range of $10^{-5} \leq -t \leq 10^{-1}$. The data along the critical isochore, within the experimentally determined asymptotic region, will be used to determine the leading critical amplitudes $A_0^{\pm}$ and background term B_{sh}.
2. Perform measurements of the susceptibility, χ_T, over the reduced temperature ranges $10^{-6} \leq t \leq 10^{-1}$ above T_c, and $10^{-5} \leq -t \leq 10^{-3}$ below T_c. The data along the critical isochore and coexistence curve, within the experimentally determined asymptotic region, will be used to determine the leading critical amplitudes $\Gamma_0^{\pm}$. The data along the coexistence curve will also be used to determine the leading critical amplitude B_0.
3. Perform susceptibility measurements along isotherms over the reduced density range of $10^{-2} \leq |\Delta\rho| \leq 10^{-1}$. The data along the critical isotherm, within the experimentally determined asymptotic region, will be used to determine the leading critical amplitude D_0.
4. Test theoretical predictions for the asymptotic scaled equation-of-state from C_V, χ_T, and *PVT* measurements obtained throughout the asymptotic critical region.
5. Test theoretical predictions for crossover models using the asymptotic critical amplitudes determined from this microgravity experiment and data obtained outside the asymptotic region.

The extent of the asymptotic region along the various critical paths will be experimentally determined from a χ^2, goodness of fit, to the theoretically predicted functional forms. This approach will be similar to the one used by Haupt and Straub [17] to analyze the microgravity measurements of C_V near the critical point in SF_6. The experimental data within these asymptotic regions will initially be used to evaluate the goodness of the data by showing that the critical exponents α, γ, and δ obtained from a best-fit procedure are consistent with theoretical scaling predictions. In the MISTE ground-base program, precision specific heat and susceptibility measurements will also be performed in the crossover region farther away from the critical point. These ground-based data will be combined with the flight data to obtain a better fundamental understanding of critical behavior throughout the critical region and to permit a thorough test of theoretical predictions.

The main systematic errors associated with attaining the MISTE objectives are expected to result from performing measurements along the paths that deviate slightly from the critical paths (the critical isochore or isotherm). In the following subsection, we discuss the requirements needed to minimize these systematic errors.

2.1 Measurements of the Critical Amplitudes and Exponents

A. Specific Heat Along Critical Isochore

In the asymptotic regime, the temperature dependence of the specific heat is sensitive to being off the critical density. Figure 6a shows the expected specific heat, C_V, as a function of reduced temperature for the near-critical isochores $\Delta\rho = \rho/\rho_c - 1 = 5\times10^{-4}$ and 10^{-3}. The deviation of C_V from the critical isochore behavior along these paths is shown in Fig. 6b. The calculations used the Ginzburg-Landau-Wilson Hamiltonian for the liquid-gas universality class $O(1)$ [29]. The resultant predictions are consistent with calculations using the restricted cubic model. One can obtain an effective critical exponent and critical amplitude from a fit of the theoretically simulated "data" to the expected critical asymptotic power law expression. Using this fitting procedure, the resultant critical exponent α is estimated to shift by -0.14 and -0.55%, while the critical amplitude A_0^+ shifts by 0.15 and 0.59% for isochores that are 0.05 and 0.1% away from the critical isochore, respectively. This analysis leads to the requirement that the critical isochore must be determined to within ~ 0.1% to keep off-criticality errors below 1% in determining α and A_0^+. The MISTE requirement for C_V is that it must be measured with an accuracy greater than 1% and the reduced temperature must be measured with a resolution of 10^{-8} K in a 1 Hz bandwidth for $|t| \geq 10^{-6}$. This level of precision in both heat capacity and reduced temperature measurements has already been experimentally achieved (see subsections 3.2

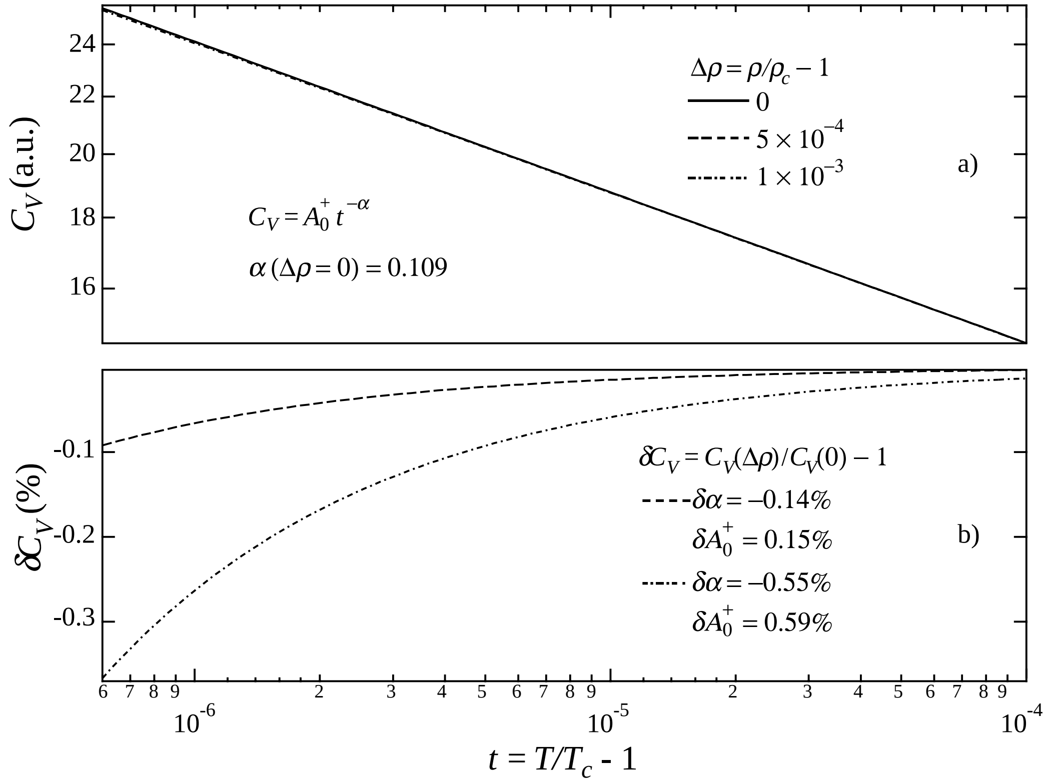

Fig. 6. Calculation of the effective critical exponent α and critical amplitude A_0^+ for C_V along near-critical isochore paths. a) is a log-log plot of the expected C_V along several isochore paths. b) shows the deviation from the critical isochore.

and 3.9).

Besides the C_V measurements in the single-phase region, additional C_V measurements are planned in the two-phase region over the reduced temperature range $10^{-5} < -t < 10^{-1}$. These additional measurements will be used to determine the critical amplitude A_0^-. The experimentally obtained critical amplitudes above and below the transition can also be used to test the critical amplitude ratio A_0^+ / A_0^- against theory.

B. Susceptibility Along Critical Isochore

A similar model calculation was also performed to show the deviation of χ_T from critical isochore behavior (see Fig. 7). Using this fitting procedure, the effective exponent γ is estimated to shift by -0.11 and -0.44%, while the critical amplitude Γ_0^+ shifts 1.3 and 5.5% for isochores that are 0.05 and 0.1% away from the critical isochore, respectively. These results for χ_T indicate that in order to obtain an experimental accuracy of ≤ 1% in the critical exponent γ, the critical density must to be determined within ≤ 0.1%, which is the same conclusion arrived at for the specific heat measurements. However, being off criticality leads to a larger systematic error in the susceptibility critical amplitude because of the stronger divergence.

C. Susceptibility Along Critical Isotherm

In Appendix B, we show that susceptibility measurements along the critical isotherm satisfy the expression $\chi_T \propto |\Delta\rho|^{-(\delta - 1)}$. For calculation purposes, we estimate that the experimentally

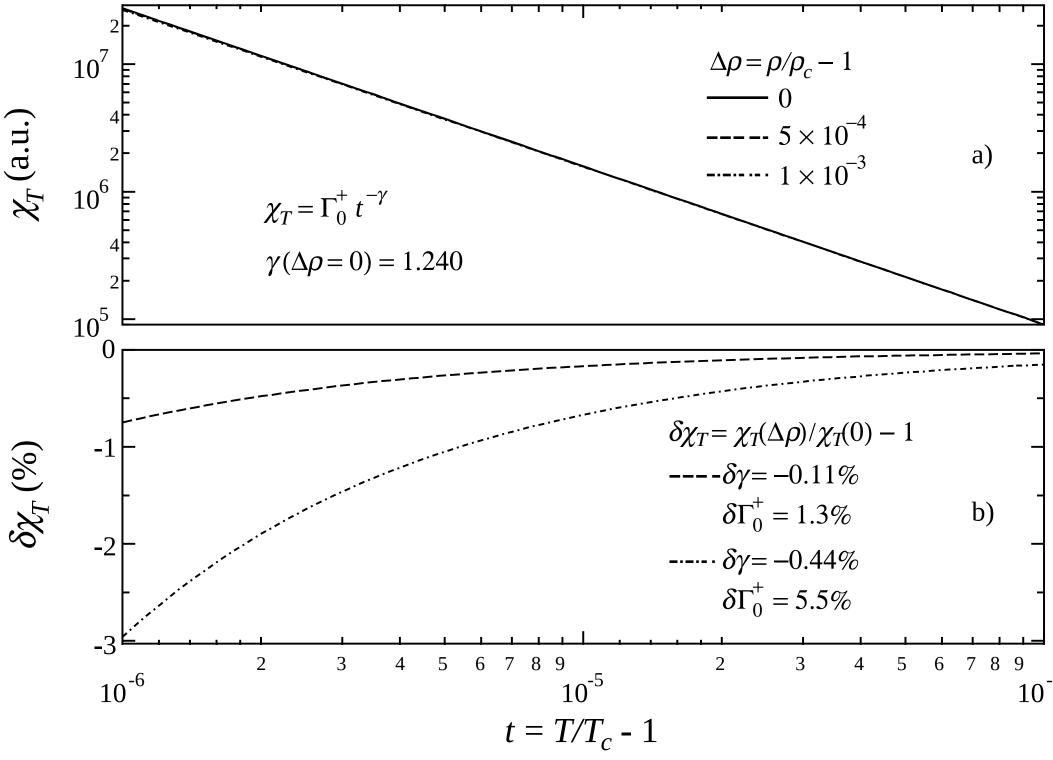

Fig. 7. Calculation of effective critical exponent γ and critical amplitude Γ_0^+ for the susceptibility, χ_T, along near-critical isochore paths.

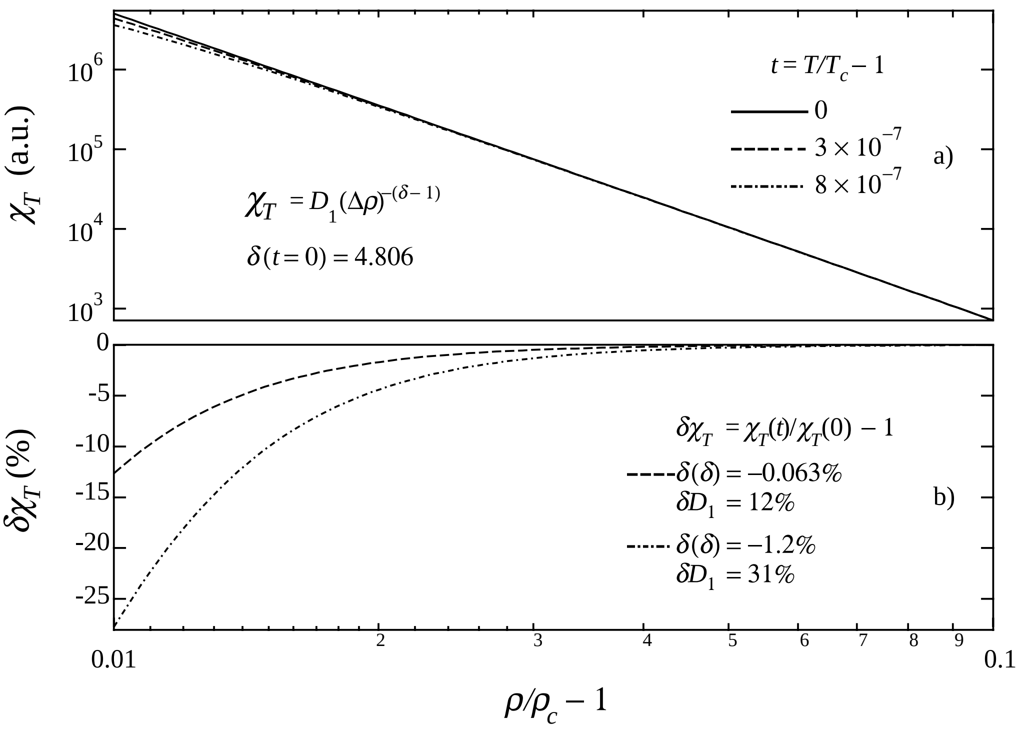

Fig. 8. Calculation of the effective critical exponent δ and critical amplitude D_1 for χ_T along near critical isotherm paths.

accessible asymptotic range along the critical isotherm will be $10^{-2} \leq |\Delta\rho| \leq 10^{-1}$. Figure 8 shows the calculated χ_T as a function of $\Delta\rho$ for two near-critical isotherms. The effective exponent δ is estimated to shift from the critical isotherm value by -0.06 and -1.2%, while the critical amplitude D_1 shifts by 12 and 31% for near-critical isotherms having reduced temperatures of $t = 3\times10^{-7}$ and 8×10^{-7}, respectively. The critical amplitude D can be determined from the expression $D = \delta/D_1$. This analysis leads to the requirement that the critical isotherm must be determined to within a reduced temperature of $t \leq 8\times10^{-7}$ to minimize the systematic error in δ to ~ 1%. Again, because of the strong divergence, one must get very close to the critical temperature to minimize uncertainties in the critical amplitude.

2.2 Test of the Homogeneity Postulate and Scaled Equation-of-State

The measurements of C_V, χ_T, and *PVT* in the asymptotic region along families of near-critical isochore and isotherm trajectories will be plotted as a function of appropriately scaled variables. The results are expected to lie on universal curves, as a consequence of the scaling configuration of the equation-of-state (see Appendix A). The display of the experimental data on universal curves will permit an investigation of the homogeneity postulate that is the basis for the self-consistency of the scaling approach. The precise shape of the various universal curves follow from the specific form of the equation-of-state. A more detailed discussion of the various predicted forms for the equation-of-state is given in Appendix A.

3. SCIENCE REQUIREMENTS

The overall science requirements are organized into ten major subsections and are discussed below. A summary of all the requirements is provided in Tables III and IV. Since the parameter values listed in the tables are often the result of optimization studies, a failure to meet any one of them may be offset to some degree by tightening the requirement in other areas. Ground-based studies were performed to demonstrate that the proposed measurement techniques have the required sensitivity to attain the flight experimental objectives. Temperature, density, and pressure sensors were fabricated and tested in an experimental cell designed to minimize gravity effects on the ground. These studies have validated the experimental measurement approaches required to perform specific heat and susceptibility measurements to the precision needed by the flight experiment. The science requirements are based on the objective of measuring the specific heat and susceptibility in the single-phase region to better than 1% resolution down to $t = 10^{-6}$.

A detailed analysis was performed on various factors influencing the measurement techniques in a microgravity environment to determine the science requirements for the flight experiment. These analyses assume that the main sources of possible errors come from (a) systematic errors due to being slightly off the critical isochore or critical isotherm, previously discussed in Section 2, (b) random errors associated with experimental measurement uncertainties, (c) density stratification in the cell due to temperature gradients, (d) long relaxation times associated with density equilibration, (e) cosmic ray heating and (f) heating, and density stratification due to vibrations.

The main measurement requirements that were determined for the flight experiment from these analyses are:

(a) The specific heat at constant volume is required to be measured along the critical isochore to better than 1% resolution over the reduced temperature ranges $10^{-6} \leq t \leq 10^{-1}$ in the single-phase region and $10^{-5} \leq -t \leq 10^{-1}$ in the two-phase region. The critical isochore is required to be determined to within 0.1%.

(b) The susceptibility is required to be measured to better than 1% resolution over the reduced temperature range $10^{-6} \leq t \leq 10^{-1}$ along the critical isochore and over the reduced temperature range $10^{-5} \leq -t \leq 10^{-3}$ along the coexistence curve. The critical isochore is required to be determined to within 0.1%.

(c) The susceptibility is required to be measured along the critical isotherm to better than 1% resolution over the reduced density range $10^{-2} \leq |\Delta\rho| \leq 10^{-1}$. The critical isotherm is required to be determined to within $t \leq 8\times10^{-7}$.

Table III. Summary of MISTE Science Requirements

Parameter	Goal	Requirement
Temperature Sensors		
Resolution in 1 Hz bandwidth at T_c in °K	10^{-9}	10^{-8}
Drift rate (K/s)	3×10^{-14}	10^{-13}
Pressure Sensors		
Resolution in 1Hz bandwidth at 1.1 bar	3×10^{-8}	4×10^{-7}
Drift rate (bar/s)	10^{-13}	4×10^{-12}
Range (bar)	3	3
Density Sensor		
Resolution in 1Hz bw at ρ_c (0.014 mole/cc)	10^{-6}	5×10^{-6}
Absolute drift rate ($\delta\rho/\rho_c$ per second)	3×10^{-10}	10^{-9}
Sample		
^{4}He impurity (PPM)	0.01	0.1
Heat capacity measurement		
Energy pulse resolution (%)	0.05	0.1
Temperature step resolution at $t = 10^{-6}$ (%)	0.1	1
Stray heat input (W)	5×10^{-9}	5×10^{-8}
Critical isochore determination ($\lvert\rho/\rho_c - 1\rvert$)	5×10^{-4}	10^{-3}
Measurement Range		
Single Phase		
Inner/Outer limit ($t = T/T_c - 1$)	$10^{-7} < t < 10^{-1}$	$10^{-6} < t < 10^{-1}$
Two Phase		
Inner/Outer limit ($t = T/T_c - 1$)	$5\times10^{-6} < \lvert t\rvert < 1\times10^{-1}$	$10^{-5} < \lvert t\rvert < 10^{-1}$
Susceptibility Measurement		
Isochore Measurement Range		
Outer limit ($T/T_c - 1$)	10^{-1}	10^{-1}
Inner limit ($T/T_c - 1$)	6×10^{-7}	10^{-6}
Critical isochore determination ($\lvert\rho/\rho_c - 1\rvert$)	5×10^{-4}	10^{-3}
Isotherm Measurement Range		
Outer limit $\lvert\rho/\rho_c - 1\rvert$	2×10^{-1}	10^{-1}
Inner limit $\lvert\rho/\rho_c - 1\rvert$	7×10^{-3}	10^{-2}
Critical isotherm determination ($T/T_c - 1$)	3×10^{-7}	8×10^{-7}

Table IV. Summary of MISTE Flight Environmental Requirements

Parameter	Goal	Requirement
Acceleration Environment		
DC	$\leq 3\ \mu g$	$\leq 5\ \mu g$
The total integrated acceleration spectrum over the range 10^{-3} Hz < frequency < 500 Hz	$\leq 750\ \mu g$ rms	$\leq 1500\ \mu g$ rms
Charged Particle Environment		
Charged-Particle heating rate (pW/gram copper)		
Inside Equatorial Band (|latitude| < 30°)	< 0.5	0.5 – 3.0
Outside Equatorial Band (|latitude| > 30°)	< 5	< 15

3.1 Experimental Cell

Figure 9a shows a schematic of the ground-based MISTE experimental cell. This cell, designed to measure specific heat C_V and susceptibility χ_T, was made of oxygen-free high-conductivity (OFHC) copper. The sample space had a flat disk shape with a height of 0.05 cm and a diameter of 11.2 cm. The small cell height minimized the effect of gravity on the ground. The cell was thermally isolated from a surrounding shield stage with an effective thermal resistance of $R \sim 10^4$ K/W. A high-resolution $GdCl_3$ magnetic susceptibility thermometer ($\delta T/T_c = 3\times10^{-10}$ resolution) measured the cell temperature. A heater, wrapped on a copper rod, was attached to the cell. A heat pulse was generated from this heater for the specific heat measurements. In the case of the susceptibility measurements, a feedback loop was used to regulate the cell temperature within several nK. A low-temperature manual valve was attached directly to the top of the cell. The fill line behind the valve was pumped out after the cell was filled with high-purity ^{3}He. A Straty-Adams capacitive type gauge ($\delta P/P_c = 4\times10^{-7}$ resolution) was positioned at the center of the cell to measure the pressure in the sample. One plate of this capacitive gauge was a flexible diaphragm that sensed pressure changes in the sample. A capacitor for measuring density ($\delta\rho/\rho_c = 3\times10^{-6}$ resolution), with essentially rigid plates having a ~ 50 μm gap, was also located in the middle of the fluid layer. This capacitor determined the sample density using the Clausius-Mossotti equation and also measured the susceptibility very near the critical point using an electrostrictive technique. The cell also contained three leveling capacitors (not shown in Fig. 9a) that will be discussed in subsection 3.6. An advantage of this cell design is the ability to perform continuous in-situ *PVT* measurements in addition to the specific heat and susceptibility measurements.

The MISTE flight experimental cell, shown in Fig. 9b, will have the same basic features as the cylindrical ground-based cell; however, the geometry will be designed to minimize the effects of microgravity and thermal equilibration time. The candidate flight cell design is a cylindrical cell having dimensions of ~ 5 cm in diameter by 4 cm in height that will provide ~ 8 times the sample mass of the present ground-based cell to increase the accuracy of the heat capacity measurements. The flight cell will have ~ 50 plates (0.5 mm thick) with holes in them and 50

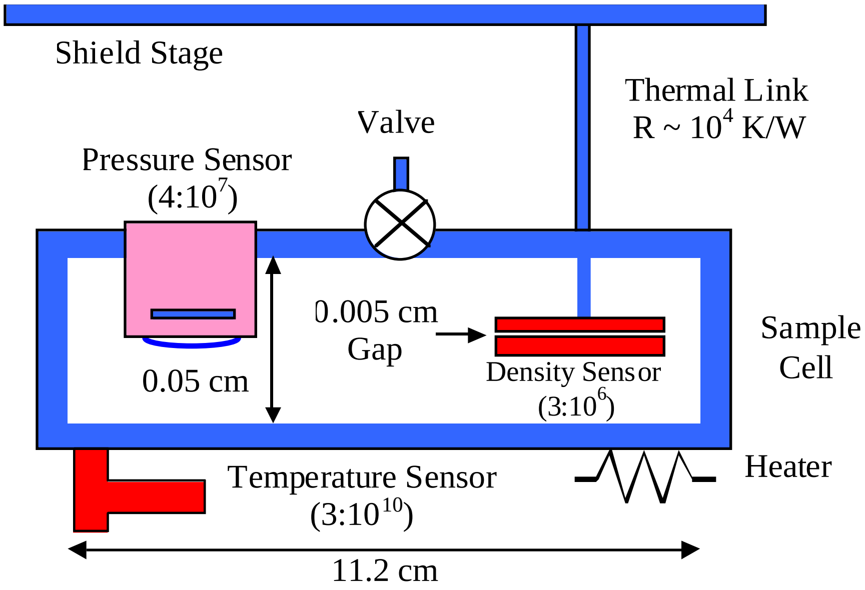
Shield Stage
Thermal Link
R ~ 10^4 K/W
Valve
Pressure Sensor
(4:10^7)
0.005 cm
Gap
Sample
Cell
0.05 cm
Density Sensor
(3:10^6)
Temperature Sensor
(3:10^10)
Heater
11.2 cm

Fig. 9a. Schematic of the ground-based experimental cell.

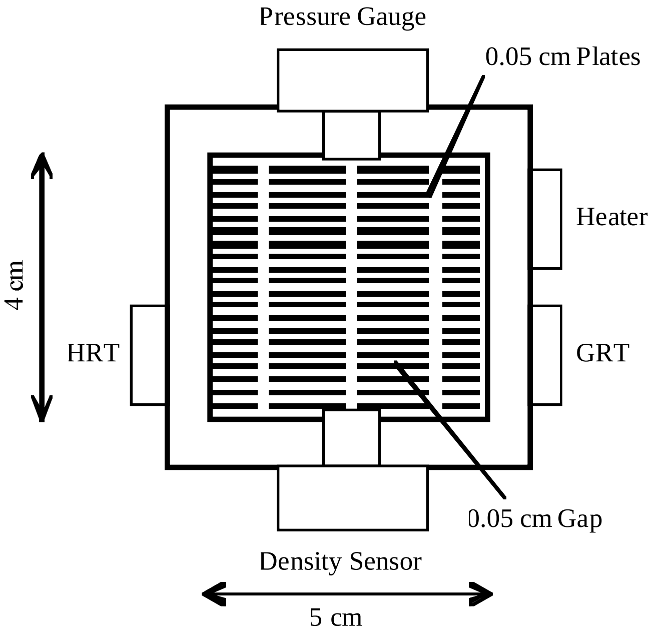
Pressure Gauge
0.05 cm Plates
Heater
4 cm
HRT
GRT
0.05 cm Gap
Density Sensor
5 cm

Fig. 9b. Schematic of the flight experimental cell.

spacers (0.5 mm) both made of thermally conducting material and symmetrically situated in the cell. The fluid layers sandwiched within the plates will be equal to or less than 0.05 cm so that the effective thermal time constant will be comparable to that obtained in the ground-based cell. The flight cell will use two sets of sensors similar to the ones described above (see Appendix C for a discussion of the two density sensors). We will also evaluate using plates and spacers that are ~ 0.25 mm thick to further reduce the thermal time constant.

A. Gravity Effects on International Space Station

The gravity effect is still an important factor in designing the measurement cell for the flight experiment. The orientation of the cell relative to the net acceleration vector can have significant consequences on the performance of this experiment. The experimental probe will be positioned along the axis of the Low Temperature Microgravity Physics Facility (LTMPF). The LTMPF in turn will be attached to one of the ports of the Japanese Experiment Module-Exposed Facility (JEM-EF) located on the International Space Station (ISS). At this time, the LTMPF M1 facility is scheduled to be located in port 2 of the JEM-EF. An analysis of the expected gravity vector has been performed for all of the potentially available ports on the JEM-EF. It is expected that during the LTMPF M1 flight, the magnitude of the net acceleration vector for port 2 will be ~ 2.9 μg with a stability of ~ 0.1 μg. Assuming the axis of the LTMPF is along the port 2 axis, the net acceleration vector will point in a direction that is $\approx 45°$ with respect to the MISTE probe axis and will have a stability of ~ 2.4° during each orbit. These results are essentially valid for all the available JEM-EF ports. This information is encouraging in that the acceleration magnitude and direction will be relatively constant over a time scale of many days.

Assuming the orientation of the net acceleration vector remains approximately constant during the LTMPF mission, the MISTE cell axis should be oriented at a fixed angle relative to the probe axis so that the cell axis is along the net acceleration vector. The motivation for considering the candidate flight cell geometry is the possibility that the actual location of the LTMPF might change. An oriented flight cell with a height of ~ 4 cm will have a 1% microgravity effect on the specific heat in a 3 μg environment at a reduced temperature of $t \sim 7\times10^{-7}$ (see Fig. 4a).

3.2 Temperature Sensor

One of the flight experimental objectives will be to measure the heat capacity along the critical isochore over the reduced temperature range of $10^{-6} \le t \le 10^{-1}$. When using the pulse technique for measuring C_V, the temperature step should be small compared with the reduced temperature to minimize nonlinear effects. To achieve a 1% resolution in the temperature at $t \sim 10^{-6}$, we require the temperature resolution to be 10^{-8} K, while the MISTE experimental goal is to achieve a resolution of 10^{-9} K in temperature in a 1 Hz bandwidth. Since measurements of C_V and χ_T will be taken near the critical point over a period of several months, we define the requirement for the drift rate of the thermometer to be $\le 10^{-13}$ K/s.

Previous flight experiments (LPE and CHeX) have successfully used a magnetic susceptibility thermometer based on a SQUID magnetometer. This type of high-resolution thermometer (HRT) showed a resolution of better than a nK (10^{-9} K) at the lambda point in microgravity. A miniaturized HRT, shown schematically in Fig. 10, has been developed to work at the ^{3}He critical point [30]. The active element of the thermometer is a $GdCl_3$ paramagnetic salt with a transition temperature of 2.2 K. The salt is thermally anchored to an OFHC copper body that is attached to the experimental cell. The signal from a superconducting pickup coil is fed to the SQUID magnetometer and a superconducting magnetic shield surrounds the thermometer. A pair of SmCo magnets generates a field strength of approximately 200 Oe at the salt that optimizes the thermometer drift and sensitivity performance. Figure 11 shows the resolution

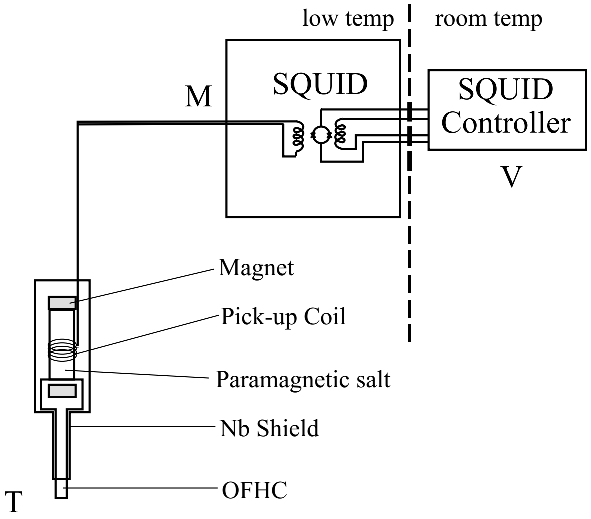

Fig. 10. Schematic drawing of a miniature high resolution thermometer.

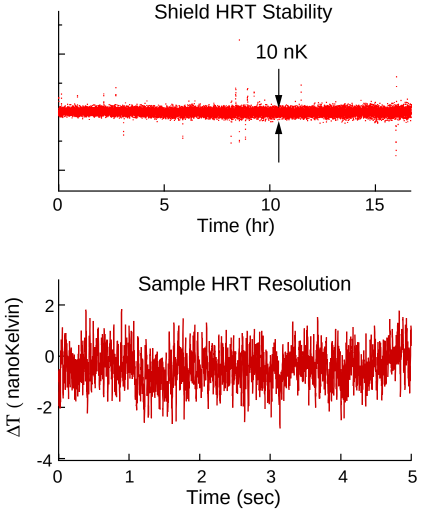

Fig. 11. Resolution of a typical $GdCl_3$ thermometer.

obtained for a $GdCl_3$ thermometer on the shield and sample stages in the ground-based system. The required temperature resolution was also demonstrated in C_V measurements using the heat pulse technique (see subsection 3.9). An absolute drift measurement test was performed using a similar HRT thermometer. This test showed that the required drift rate was met.

A commercially available germanium resistance thermometer (GRT) measured with a resistance bridge system can resolve $\approx 10^{-7}$ K using a power dissipation of 0.03 to 0.3μW. We plan to use a GRT for performing C_V measurements with at least a 1% precision for $t > 10^{-4}$.

3.3 Density Sensor

The fluid density will be determined by measuring the ^{3}He dielectric constant using a capacitor. The measured dielectric constant is then converted to density via the Clausius-Mossotti (C-M) equation.[1] The critical density needs to be determined within 0.1% in order to minimize systematic errors in the asymptotic critical exponents and critical amplitudes. The required density resolution is $\delta\rho/\rho = 10^{-5}$ to resolve the difference between two densities by 0.1%. However, the required density resolution is driven by the electrostriction technique. For this technique, a density resolution of $\delta\rho/\rho = 5\times10^{-6}$ is required to attain a 1% uncertainty in the density difference of $\delta\rho/\rho = 5\times10^{-4}$ that is needed for a 1% susceptibility measurement (see Appendix B). Furthermore, this required resolution must be met under the condition that the excitation voltage on the capacitor be less than 1V rms in order to reduce the systematic error caused by the nonlinear effect in the χ_T measurement. Since, in the electrostrictive technique, a typical density difference ($\delta\rho/\rho = 5\times10^{-4}$) will be established over a time period comparable to the fluid relaxation time (~ 1 hour close to the transition), we define the requirement for the capacitor drift rate ($\delta\rho/\rho$ per second) to be $\leq 10^{-9}$. The drift rate of the present capacitor has been verified to be ~ 1.2×10^{-10}, which meets the flight requirement.

---

[1] There are a few important issues regarding the use of the C-M relationship near the critical point experiments. The fundamental assumption behind the C-M equation is that the polarizability of the molecules in the fluid is unchanged by neighboring molecules. This is certainly true far away from the critical point where fluctuation effects are negligible. However, one could expect nontrivial correction terms to appear near the critical point where the effects of density fluctuations are nonnegligible. These effects have been studied both experimentally and theoretically near liquid-gas critical point of ^{3}He [31]. From a practical point of view the C-M relation has been found to be valid even in the critical region.

The capacitor used in the present ground-based experiment had one electrode made of a BeCu disk and another one made of a copper-coated sapphire disk. The sapphire disk was bonded to the cell boundary to quickly conduct away any heat generated in the capacitor gap. The BeCu disk was suspended from the sapphire disk and immersed in ^{3}He fluid. This arrangement minimized any pressure effect on the capacitance measurement. The capacitor gap was 50 μm. Another nearly identical capacitor was mounted outside the cell in vacuum as a reference. A seven-digit ratio transformer, lock-in amplifier and ×10 preamplifier formed the capacitance bridge. For the ground-based measurements, the bridge was operated at ~ 2700 Hz using a 14.7 V excitation voltage across the ratio transformer and a lock-in time constant of 0.3 s. The offset voltage from the lock-in was monitored by a computer and used to interpolate the capacitance ratio beyond the seventh digit. We can resolve $\delta\rho/\rho \sim 3\times10^{-6}$ with this ratio transformer-based capacitance system. For the flight system, further improvements are planned to achieve the same sensitivity using a minimum AC excitation voltage of ~ 1V. A design similar to the binary ratio transformer successfully developed for the Critical Viscosity of Xenon (CVX) experiment [32] is being considered. Two capacitive density sensors with different gap dimensions will be used for the flight experiment in order to correct for surface interaction effects (see Appendix C).

3.4 Pressure Sensor

A Straty-Adams type capacitive pressure gauge [33] has been fabricated to measure the in-situ sample pressure in the ground-based cell. The gauge used a small portion of the cell boundary as a flexible diaphragm that moved in response to a pressure change. A plate was attached to the diaphragm, and a capacitor was formed using a second plate held in close proximity. The ground-based pressure gauge has a sensitivity of $\delta P/P \approx 4\times10^{-7}$. This pressure resolution can be further improved by reducing the pressure sensor diaphragm thickness and the capacitor gap. The high-precision pressure gauge will mainly be used to measure *PVT* isotherms, from which the susceptibility and critical density can be determined. These isotherm measurements take several hours requiring a drift rate for the pressure gauge ~ 4×10^{-12} bar/s that has been demonstrated experimentally.

A pressure resolution of $\delta P/P \leq 10^{-10}$ would be needed to determine the susceptibility to 1% at $t \leq 10^{-6}$ from a *PVT* measurement (see Fig. B2 in Appendix B). This sensitivity is difficult to achieve using a conventional pressure sensor. The ultimate factor limiting the pressure resolution comes from the coupling of a pressure fluctuation to a temperature fluctuation in a constant volume experiment. The requirement for a temperature resolution of $\delta T/T = 10^{-8}$ limits the requirement for the pressure resolution to be 3×10^{-8}. Either one of the two flight high–precision pressure gauges will be used to calibrate the density sensors used for the electrostrictive technique in the region where the two techniques overlap farther away from the critical point.

A commercially available self-balancing capacitor bridge was used to measure the pressure sensor in the ground-based studies. However, for flight we plan to use a ratio transformer-based capacitance bridge identical to the one planned for the density measurements.

3.5 In-Situ Fluid Transfer System

The flight experiment will require a fluid transfer system to change the density in the cell. This system must allow the density to be changed between fixed values for measurements along isochores, and it must also be capable of slowly ramping the density for isotherm measurements. Initial ground experiments used a stepper-motor actuated piston at room temperature to perform these tasks. Such a system is not ideal for the flight experiment, so an in-situ sample transfer system based on a charcoal sorption pump was devised. A schematic diagram of the proposed flight system is shown in Fig. 12. This system has a low-temperature valve that is closed during constant density measurements or opened during density sweeps or other adjustments. With the valve open, the amount of helium in the cell can be controlled over a wide range (± 10%) by heating the sorption pump to a temperature of about 30K. The regulated heat sink protects the carefully regulated lower stages from the hot gas that flows from the sorption pump. This heat sink and another on a small valve stage are held above the cell temperature to avoid condensation and phase boundaries in the transfer lines. A prototype system of this kind was used extensively in ground-based measurements and has performed well.

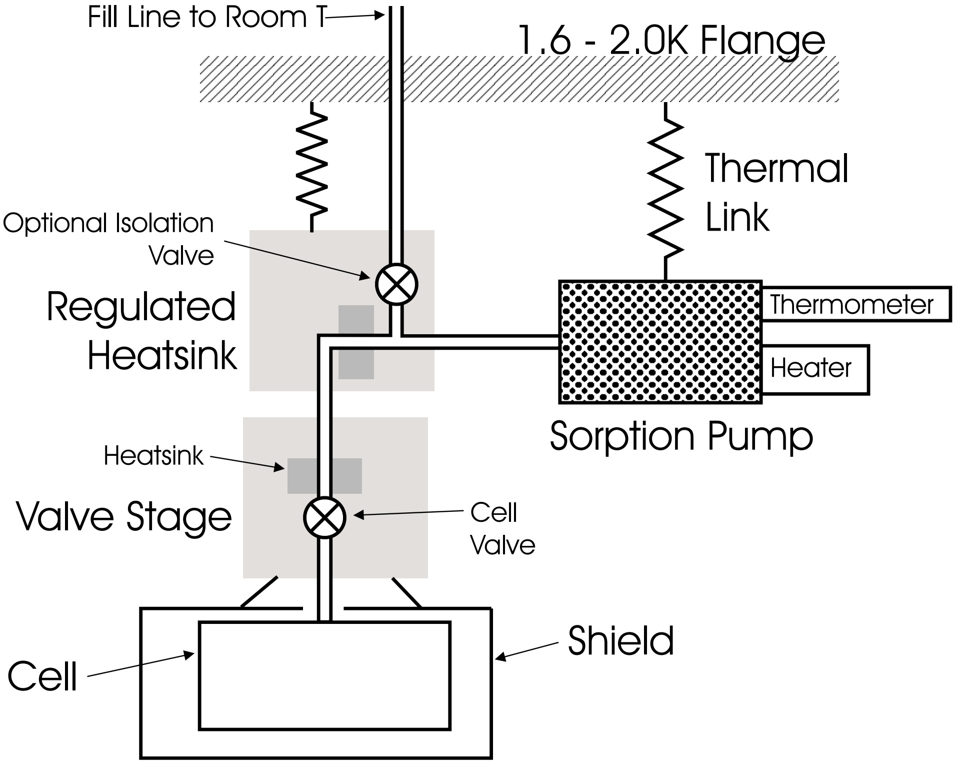

Fig. 12. Schematic of in-situ fluid transfer system.

The proposed flight in-situ system has one valve that needs to be remotely controllable on-orbit. This is the valve that isolates the cell from the sorption system for constant-volume specific heat and electrostriction measurements. It will be opened and closed at least 25 times during the flight. Our baseline plan is to use a valve being developed in cooperation with Mission Research Corporation (MRC), which is a smaller version of an MRC valve, planned for use in the LTMPF. An alternative choice is a pressure-actuated valve of the previously flown Lambda Point Experiment type. The valve leak rate requirement is $< 10^{-6}$ std-cc helium/s. This leak rate is needed to maintain the density constant to 0.02% over a 1 month period, which is the maximum expected on-orbit time for runs at a given fixed density. This requirement can be relaxed somewhat because the sample density will be continuously monitored, and re-filling the cell is also possible. The requirement that the preflight filling density not change by more than 0.1% over a 6 month launch campaign gives about the same leak rate requirement. The constant volume measurements with the most restrictive density requirements will be performed at the beginning of the data-taking period to minimize any adverse effects associated with a possible degradation of valve performance.

The pressure to actuate the valve will be provided by a hot-volume system filled with ^{3}He. The use of ^{3}He prevents superfluid thermal shorts to colder parts of the LTMPF cryoprobe. A similar system was previously used to actuate a low-temperature valve [34], and as a backup procedure the gas supply available on the LTMPF facility could be used for the valve actuation. Another valve may also be needed to isolate the low-temperature sample handling system from the fill line to room temperature. This valve would also be pressure actuated, but it would only need to be actuated a few times on the ground for initial sample filling. The leak rate requirements on this valve are much less restrictive than for the cell valve since the isolation valve is only used to protect the system from fluctuations caused by bath temperature variations or other disturbances. This valve is not presently used in ground experiments, and the actual need for it in the flight experiment is being evaluated.

3.6 Determination of Critical Density and Temperature

A precise determination of the critical density and temperature is crucial to the success of this experiment. To obtain the stated objectives, the critical density must be determined to within 0.1% and the critical temperature to within $t = 8\times10^{-7}$. Measurements along several near-critical isochores and isotherms are planned for the MISTE flight experiment to accurately determine the critical parameters. An additional factor that is important for ground-based measurements is the need to make sure the cell is level to minimize the effective vertical height. A leveling concept was used that matched the cell angle to that of a free, horizontal, liquid surface. There are three equally spaced leveling capacitors that have their electrodes flush with the top and bottom surfaces of the cell. After the cell was initially filled to approximately the critical density, it was cooled into the two-phase region to $t \sim -10^{-3}$. The capacitors were then calibrated in the liquid and gas phases by tilting the dewar support. With this calibration, the capacitors could be used to determine the liquid level with respect to the cell bottom. Leveling was accomplished by again slightly tilting the dewar support to make the liquid levels equal. In practice, this leveling method can resolve changes in angle of less than a micron in height across the width of the cell. However, due to slight geometric imperfections in the cell, we only expect the absolute leveling to be accurate to about 25 μm (~ 0.01°) over the cell diameter. Variations in the cell level over time due to helium bath level changes and other effects is less than 15 μm.

In the present ground-based studies, a near-critical density was experimentally obtained by measuring the pressure-density curve for an isotherm slightly above the critical isotherm and just outside the gravity-affected region. This was achieved by initially overfilling the cell and then regulating the cell slightly above the critical temperature. Fluid was then slowly leaked out of the cell while maintaining a constant temperature. Figure 13 is an example of the resultant pressure-density curve obtained for an isotherm at a reduced temperature of 6×10^{-4}. This curve has an inflection point that is associated with the inverse of the maximum of the susceptibility, $\chi_T = \rho^2\kappa_T = \rho(\partial\rho/\partial P)_T$. The maximum of χ_T versus ρ defines the critical density for isotherms close to the critical point. This approach is particularly valid for ^{3}He, which has an extraordinarily symmetric coexistence curve with the smallest rectilinear diameter among all the simple fluids [18]. The raw data were smoothed and the smoothed data were used to calculate the experimental χ_T. The calculated χ_T derived from the slope of the P-ρ curve near the inflection point is shown in the insert in Fig. 13. The density corresponding to the maximum in χ_T was taken as ρ_c and was determined to within 0.1%, which is the requirement for performing specific heat and susceptibility measurements along the critical isochore. Once this critical density was determined, the experimental cell was refilled again and sealed at the capacitance value corresponding to ρ_c.

Once the critical isochore is determined, accurate measurements of the specific heat and susceptibility can be made along this path. An initial estimate of the critical temperature can be made by locating the specific heat peak from measurements in both the single and two-phase regions. In this approach, the specific heat is measured during a slow cooling drift run in which successive heat pulses are applied. The critical temperature will be determined from the abrupt increase in the relaxation time of pulsed C_V measurements as the fluid crosses from the single- to

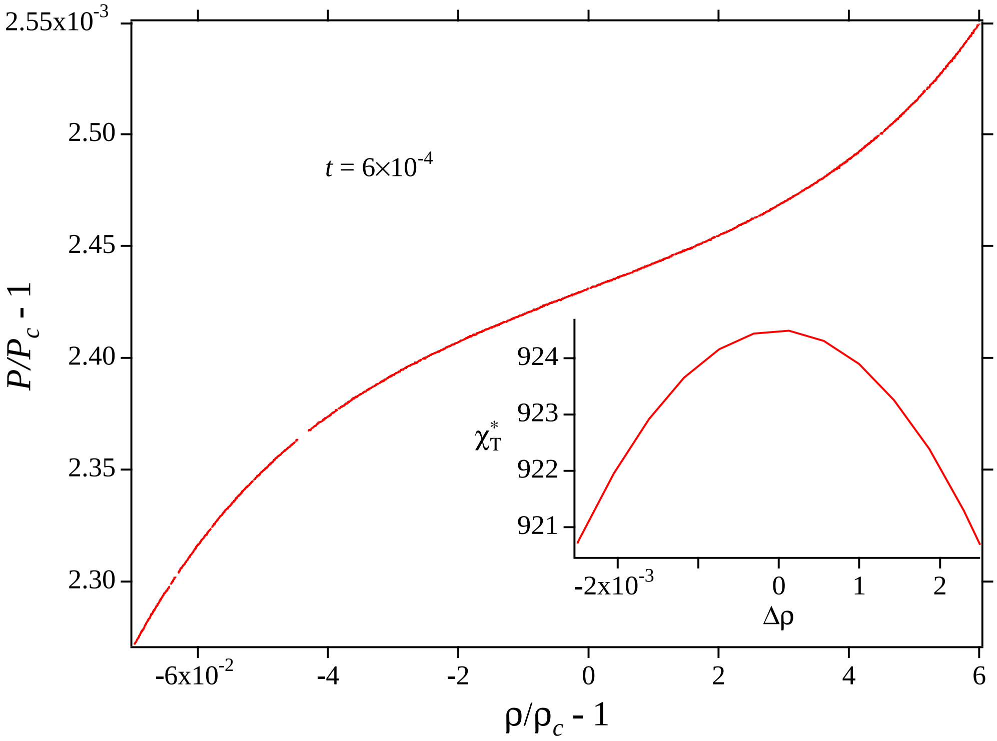

Fig. 13. Pressure-density curve at a reduced temperature $t = 6\times10^{-4}$ in the single-phase region. $\chi_T^* = (P_c/\rho_c^2)\chi_T$ is dimensionless.

two-phase region (see Fig. 17 and Ref. [16]). In the single-phase region, a temperature gradient is established almost instantly after a heat pulse due to the strong piston effect (see subsection 3.7). In the two-phase region, the relaxation time in the asymptotic region is expected to divergence as $\sim t^{-\gamma/2}$ [27]. The large discontinuity in the measurable relaxation time should be easily observed [16]. On the ground, these quantities will experience significant rounding near the transition due to a gravity-induced density stratification starting at $t \approx 10^{-4}$ (see Figs. 3 and 4 and Table II). However, in a microgravity environment we expect a 1% C_V rounding at $t \sim 7\times10^{-7}$ for the proposed flight cell of maximum height 4 cm.

A second method for determining T_c comes from a slow cooling drift run for measuring the susceptibillity using the electrostriction approach. By performing these measurements with a small, constant DC bias, one continuously obtains a characteristic signature of the susceptibility as the system crosses over into the two-phase region. The critical temperature is related to the peak in the data. This susceptibility approach should be more sensitive than the specific approach because of the stronger divergence in the susceptibility. A consistency check on the determination of T_c can be made by performing both the specific heat and susceptibility measurements during the same cooling drift run. A final consistency check will come from the value of T_c determined from fitting the measured C_V and χ_T along the critical isochore.

A. ^{4}He Impurity in ^{3}He Sample

Since the liquid-gas critical temperature of ^{3}He is very low (3.3 K), the only nonfreezing impurity at this temperature is ^{4}He. Horst Meyer's group at Duke University has studied the thermodynamic properties of ^{3}He-^{4}He mixtures near the liquid-gas critical point over a number of years. A review is given in Ref. [36]. In the presence of a ^{4}He impurity in a ^{3}He sample, the divergence of the susceptibility will be the same as that for pure ^{3}He along a constant concentration susceptibility path that is not the same as an isochore path. Since the MISTE flight experiment will follow the paths of the critical isochore and isotherm to approach the critical point, a crossover to a mixture behavior in the compressibility measurement is of concern. The crossover temperature is approximately $t_{s1} \approx [A_0 X(1 - X)]^{1/\gamma}$, where X is the molar concentration of ^{4}He in ^{3}He. For $t >> t_{s1}$, the susceptibility divergence is essentially that of a pure fluid, and the systematic error caused by a ^{4}He impurity in determining γ or Γ_0^+ is negligible. Using the parameters of the ^{3}He-^{4}He mixture provided in Ref. [36], one obtains $A_0 \approx 0.07$. The present MISTE experiment uses commercially available ^{3}He gas containing less than 1 ppm of ^{4}He, which implies $t_{s1} \leq 9\times10^{-7}$. In the MISTE flight experiment, the susceptibility will be measured over $10^{-6} \leq t \leq 10^{-1}$. Therefore we define the requirement for ^{4}He impurity in ^{3}He sample to be less than 0.1 ppm. A multiple distillation process can easily be performed to achieve this required purification. For specific heat at constant volume, a similar crossover to a mixture behavior occurs at a much smaller reduced temperature; hence, it is not of concern when the volume is constant.

Another effect of the ^{4}He impurity in ^{3}He sample is to shift the critical temperature upward by approximately 1 μK per ppm (^{4}He) from the value of a pure ^{3}He sample [26]. Since only the relative distance to the critical temperature needs to be measured precisely, the small shift in T_c due to a ^{4}He impurity is not of concern as long as the impurity remains constant during the flight experiment.

3.7 Equilibrium Time Constants and Density Stratification

The C_V and χ_T measurements are performed in the presence of disturbances (such as a heat pulse or pressure change) applied to the ^{3}He fluid system. These disturbances produce temperature and density inhomogeneities in the system. The equilibration processes associated with the way these inhomogeneities decay to a steady-state condition near a liquid-gas critical point have been studied extensively [27,35].

The MISTE experiment will be performed in a constant-volume cell. In this case there are two time scales that characterize the equilibration process in the single-phase region ($T > T_c$). One of the time constants is the "piston time," and it is expressed as [37]

$$\tau_1 = \left(\frac{h}{C_P / C_V - 1} \right)^2 \frac{1}{D_T}, \tag{22}$$

where h is the cell height, D_T is the thermal diffusivity, and C_P and C_V are specific heats of constant pressure and constant volume. At a small reduced temperature near the critical point, the density change within the surface boundary layer can be very sizable just after a temperature disturbance at the boundary. For this case, the piston time scale is modified and has the form

$$\tau_1 \approx \left(\frac{\langle C_V \rangle}{(C_P)_b} \right)^2 \frac{h^2}{(D_T)_b} \quad \text{at small } t, \tag{23}$$

where the values of C_P and D_T are calculated at the boundary and C_V is spatially averaged. The second time scale is the diffusive relaxation time,

$$\tau = \left(\frac{h}{2\pi} \right)^2 \frac{1}{D_T}. \tag{24}$$

From time τ_1 to τ, the temperature inhomogeneity equilibrates in a power-law fashion. After time τ, the remaining temperature inhomogeneity (usually undetectable) and sizable density inhomogeniety (the result of the divergent thermal expansion coefficient) relax diffusively.

Figure 14 shows the expected temperature-dependent behavior in microgravity for the two time scales. The solid line corresponds to the diffusive relaxation time that diverges as the critical point is approached. The piston time scale, given by the dashed line, approaches zero as the critical point is approached. In a real fluid system very near the critical point, τ_1 is expected to be larger than the values shown in Fig. 14 due to nonlinear effects. We have performed model calculations to determine the optimum drift rate to limit the density inhomogeneity to < 0.1% from its mean throughout the cell. For the ground-based cell of 0.05 cm height, the optimum drift rate is $\leq 3\times10^{-4}$ K/hr. Since the flight cell will have the same fluid height between plates we expect the same optimum drift will be valid.

In the case of isothermal susceptibility measurements, the cell will be controlled at a higher

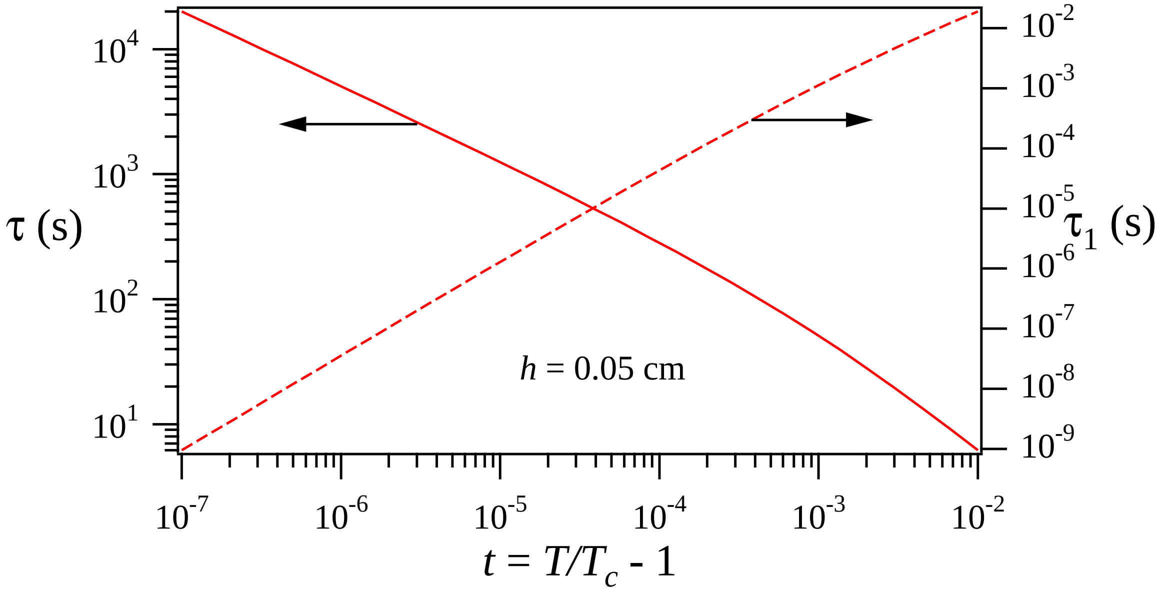

Fig. 14. The piston time and diffusive relaxation time versus reduced temperature at the critical density.

temperature than the surrounding shield stage. The cell heater will be wound around the thermal contacts connecting the cell to the shield in such a way as to minimize a temperature gradient within the cell wall. On the other hand, for the heat capacity measurement using a cooling-drift technique, heat must be removed from the cell as its temperature free-falls towards the shield temperature. This heat flow could produce a temperature gradient in the cell wall since its thermal conductivity is not infinitely large. Such a temperature gradient in the cell wall between the closest and furthermost points to the thermal contacts would induce a corresponding density inhomogeneity in the sample both in the single and two-phase regions. We are addressing this issue both theoretically and experimentally. A detailed 3-D finite-element thermal model study of the behavior of the proposed flight cell in the single-phase is now in progress. For this model study, we assume an OFHC copper thermal conductivity of 6 W/cm K and a maximum heat input of 1 μW that is an order of magnitude larger than for C_V pulse and χ_T measurements. This model should provide us with the spatial and temporal profiles of the temperature, density, and pressure within the cell for various initial conditions.

In the two-phase region, the time constant associated with a change in temperature will be much longer due to mass transfer (release of latent heat) between phases at the phase boundary. It is very difficult to model this two-phase equilibrium process. However, insight into this time constant issue will be obtained by experimentally measuring the equilibrium time constant and temperature gradient in a prototype flight cell with its copper plates both along and normal to the gravitational field. The shape of the phase boundary is significantly different for these two orientations. The results from the modeling study and ground-based measurements will support the determination of the design and ultimate orientation of the flight cell.

3.8 Charged-Particle and Vibration Environment

A. Charged-Particle Environment

At this time, reliable data on the expected radiation environment on the ISS are not available. However, the bulk heating effect by charged particle fluxes through a part of the ISS orbit has been recently estimated [38]. The model calculation used the LPE (Lambda Point Experiment) heating data for comparison and calibration. Away from the South Atlantic Anomaly (SAA) the heating is mainly due to galactic cosmic rays (GCR). The model can estimate heating effects due to the GCR within 50% in an equatorial band covering about 60% of the area swept by the station. Away from the equatorial band, the estimation of GCR is less accurate. Due to the lack of data at this time, it is not trivial to predict accurately the cosmic ray heating throughout the entire ISS orbit. However, the model can still conservatively estimate the heating effect when the orbit is away from the SAA and still within an equatorial band. Initial estimates are for a 15 - 20 minutes SAA duration in these bands that occurs twice during a given orbit (~ 90 min). The heating effect within an equatorial band is effectively independent of latitude. The GCR level within a band of -20° < latitude < 20° is less than 0.5 pW/gm (Cu). Outside this band (higher latitude), the heating level varies up to ~ 15 pW/gm depending on the latitude.

The model estimates less than ~ 0.5 pW/gm (Cu) from GCR within an equatorial band at the solar minimum year (2007, altitude ~ 370 km). It is assumed that this heating rate leads to

~ 1.5 nW of heat leak to a 3 kg copper sample cell. This heating effect will be negligible during isothermal experiments (*PVT* or electrostriction technique) that are planned for measuring the susceptibility along various critical paths. However, if the heat capacity is measured using a cooling drift technique, the heating due to the cosmic ray will impact the measurement to varying degrees depending on the position of the orbit. Model calculations indicate that a cooling drift rate of approximately -0.3 mK/hr is required over the range $10^{-6} < |t| < 10^{-3}$ to maintain an accumulated density gradient of less than 0.1% within an internal cell having 0.05 cm plate spacing. For this cooling rate, approximately 1.5 μW would be extracted from the sample cell (~ 0.5 mole of sample) for approximately 3 hours to finish a drift heat capacity run. Within an equatorial band, this cooling rate is well above the cosmic ray heating. Even outside these bands the effect will be negligible, and this small effect could be removed in the analysis by using charged particle monitoring data. However, inside the SAA, the cosmic ray heating effect will not be negligible for this technique. The expected high heating rate in the SAA will limit the available time of the drift heat capacity measurement during the orbit and will require a well-defined data acquisition scenario.

In the earlier CHeX flight experiment, the effect of the cosmic ray heating was shown to be minimal when the adiabatic heat pulse technique was used to measure the specific heat. This experiment required more sensitive heat control than will be needed by MISTE. Most of the flight heat capacity measurements will be performed within $10^{-6} < |t| < 10^{-1}$ using a heat pulse technique. Inside an equatorial band the cosmic ray heating effect can be roughly estimated. A total of 1.8 μJ of energy will be deposited into the copper sample cell if we assume a 20 minute duration in this band with 1.5 nW of heating. This will heat up the sample (0.5 mole) by about 6×10^{-8} K during the experimental measurements. This heating rate is negligible for the heat capacity data between $10^{-6} < |t| < 10^{-1}$. It is important to note that both adiabatic pulse and cooling drift measurements further away from the asymptotic region could be performed even within the SAA. For example, the 3 kg copper sample cell would be exposed to ~ 1.5 μW assuming the heating rate in the SAA is ~ 500 pW/gm. This effect would be negligible for heat capacity measurements outside the asymptotic critical region ($t > 10^{-4}$).

So far we have only estimated the uniform heating effect of cosmic rays on the sample cell. It is also important to estimate the local heating effect in the *PVT* sensors on the sample cell. This local heating can produce a nonisothermal boundary condition that could lead to a density gradient in the sample. Let us first consider a high-resolution thermometer using a $GdCl_3$ salt (~ 0.3 gm) and having ~ 9 K/W thermal link to the cell. These conditions would only produce ~ 1 nK offset at the maximum heating rate in the SAA. Thus, in this case there would be very little thermal gradient along the entire cell and a negligible systematic error in the temperature measurement. The pressure and density sensors used in present experiments mainly consists of materials with relatively high thermal conductivity (mostly BeCu, Cu, and sapphire); these materials should not contribute to a thermal gradient problem. For high-precision measurements in the equatorial band we must be able to recover quickly from the SAA heating effects during an orbit. The calculations above predict a 1.5 μW heating effect when passing through the SAA. This level of heating can easily be controlled to maintain the MISTE cell at the temperatures required for performing measurements at the conclusion of an SAA encounter.

The low-earth-orbit neutron environment and its effect on ^{3}He have also been studied [38]. The preliminary results show that the neutron heating of the sample in the proposed MISTE flight cell geometry is less than 0.1 nK in the SAA. Although the heating effect is negligible, the ionization caused by the products of the neutron or charged particle-induced nuclear reaction may increase the electrical conductivity of a ^{3}He sample. This may degrade the performance of density measurements where an electric field is present in the capacitor sensor. A recent flight experiment using xenon near the critical point [32] showed a slight degradation of the signal due to this effect in SAA. Unlike the heating effect due to neutrons, which leads to a systematic density inhomogeneity, this ionization effect can be minimized by data averaging.

Another possible radiation effect is related to the MISTE density sensor. During electrostriction measurements the density sensor capacitor contains ^{3}He subjected to a large electric field. The field is 100 times less than the dielectric breakdown strength of the helium during ground experiments, however the charged particles in the Space Station environment may considerably reduce the breakdown threshold. The MISTE team is collaborating with JPL radiation effects experts to evaluate this possible problem and to set up an experimental ground-based test to determine the magnitude of this effect.

The analysis above is very conservative. The actual situation on the ISS flight is expected to be much less restrictive. A more precise data acquisition flight scenario will be developed as more accurate information is obtained on the expected radiation environment on the ISS. If additional information is not available before the flight, initial data acquisition runs will be performed early in the mission to directly evaluate the cosmic ray heating effect on thermodynamic measurements. This information will then be used to adjust the mission data acquisition scenario.

B. Vibration Environment

The Boeing Corporation has performed calculations of the vibration environment for various locations on the ISS. The LTMPF will be mounted on the Japanese Experimental Module (JEM). Estimates of the vibration levels expected for the LTMPF on the JEM are given in the LTMPF Science Requirements Envelope Document (SRED) [39]. In addition, we have performed a detailed analysis of the vibration effects on the measurement of the specific heat and susceptibility near a liquid-gas critical point [40]. There are several ways in which vibrations can be felt in the MISTE experimental configuration; the following text is a summary of the analysis that has been performed for the most significant of the known influences from the vibration spectrum. The analysis has been applied to the MISTE ground-based cell of height L = 0.05 cm and diameter D = 11.2 cm. Assuming that the flight cell will have plates that are separated by a gap $\leq L$ and a diameter $\leq D$, the analytical results should correspond to a worst-case scenario for the flight experiment.

Vibration Effects Analysis

Random accelerations lead to a variety of effects. In this analysis, we consider the consequences of random accelerations on (1) density fluctuations that result from random accelerations and the temperature variations induced by these density fluctuations, and (2) the temperature drift due to vibration-induced viscous heating. Before consideration of these various effects, we review a key property of the response of the experimental system to the vibrations to which it will be subjected in a microgravity environment.

AC Versus DC Response

AC accelerations give rise to transient effective gravitational forces that can be much larger in magnitude than the constant microgravity environment. These AC accelerations are not important for the MISTE experiment because of the way in which temperature and pressure differentials are equilibrated. In a constant-volume cell, the response to AC perturbations is adiabatic, rather than isothermal, if the frequency of the perturbations is sufficiently high. This fact has important effects on the magnitude of the response. For example, the adiabatic compressibility has the temperature dependence $t^{-\alpha}$, while the isothermal compressibility goes as $t^{-\gamma}$. The critical exponent α is a little greater than 0.1, while $\gamma \approx$ 1.24. Thus the isothermal compressibility is considerably greater than the adiabatic version of this response at small reduced temperatures.

The key to the response of the system lies in the crossover frequency, separating adiabatic from isothermal response. This frequency is governed by the diffusive process by which the temperature of the system is equilibrated. The formula for the crossover angular frequency, ω_c, is

$$\omega_c = \frac{1}{\tau_c} = \left(\frac{D_T}{\left(L / \pi\right)^2} \right), \tag{25}$$

where L corresponds to the smallest cylindrical cell dimension. The thermal diffusion constant, D_T for ^{3}He is given by

$$D_T = 3.99 \times 10^{-4} t^{0.75}\ \mathrm{cm}^2\ /\ \mathrm{s}. \tag{26}$$

If we assume $L = 5\times10^{-2}$ cm, then

$$\tau_c = 0.64 \times t^{-0.75}\ \mathrm{s}. \tag{27}$$

Figure 15 shows a log-log plot of the characteristic crossover angular frequency as a function of the reduced temperature, t. Note that at $t = 10^{-6}$, the crossover between AC and DC response is at about $\omega = 10^{-4}$ Hz. This is considerably below the lower threshold of vibrations that one expects to encounter on the ISS. Recall that a frequency of 10^{-4} Hz corresponds to a period of about three hours.

Fluctuations in the Density Resulting from Random Accelerations

Vibrations lead to fluctuations in the density of the ^{3}He sample. Because the compressibility of this system diverges at the critical point, this effect must be taken into account. After careful analysis [40], one finds for the fractional deviation in the density of the system

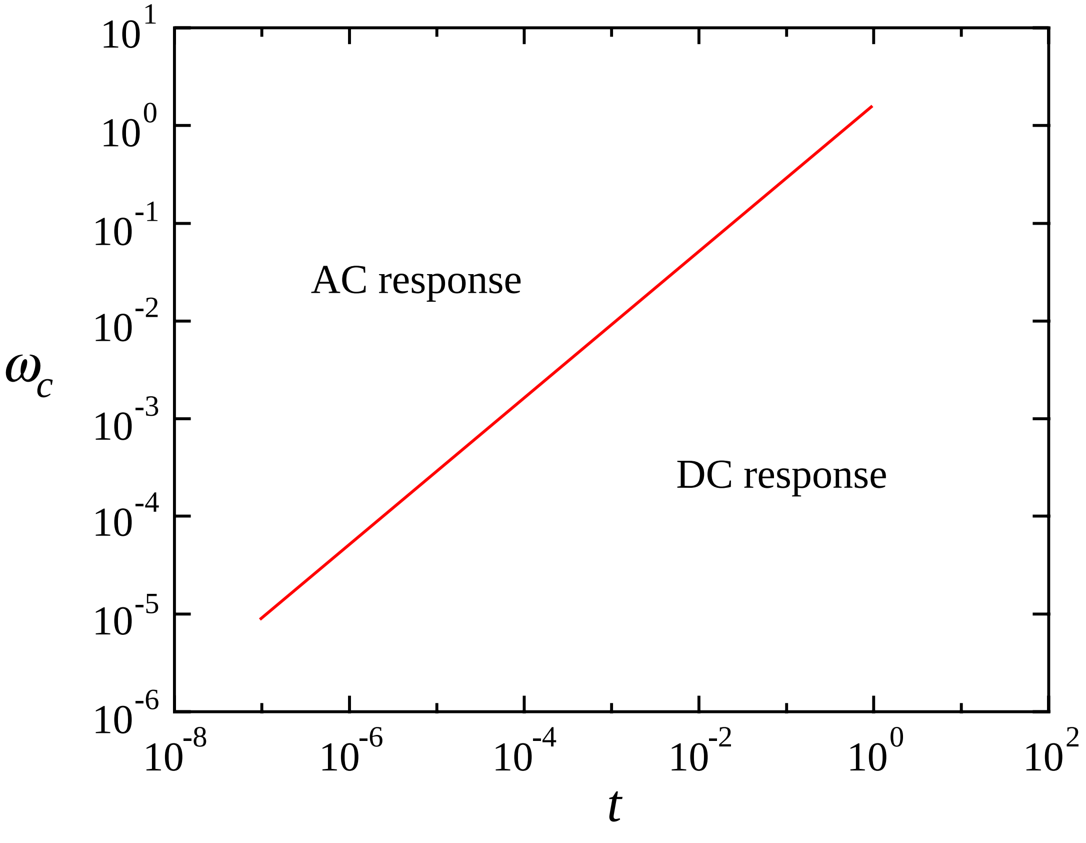

Fig. 15. Log-log plot of the characteristic crossover angular frequency ω between AC and DC responses.

$$\begin{aligned}\frac{\sqrt{\delta\rho^2}}{\rho_c} &= \frac{D}{C_S^2}\sqrt{\int_{-\infty}^{\infty}\langle a(\omega)a(-\omega)\rangle d\omega} \\ &= 1.1\times10^{-8}t^{-\alpha}\sqrt{\int_{-\infty}^{\infty}\langle a(\omega)a(-\omega)\rangle d\omega}\ ,\end{aligned} \tag{28}$$

where ρ_c is the critical density, C_s is the adiabatic sound velocity, and $a(\omega)a(-\omega)$ is the mean square acceleration per unit angular frequency. Because of the smallness of the critical exponent α, the fractional rms fluctuation in the density is very insensitive to the reduced temperature. For example, at $t = 10^{-7}$, $\delta\rho_{\mathrm{rms}}/\rho_c \sim 6.5\times10^{-8}\sqrt{\int_{-\infty}^{\infty}\langle a(\omega)a(-\omega)\rangle d\omega}$. If the fractional change in the density is to be less than one part in 10^4, then we have the following restriction on the integrated spectrum of vibrations:

$$\sqrt{\int_{-\infty}^{\infty}\langle a(\omega)a(-\omega)\rangle d\omega} < 1.54\times10^{3}\ \mathrm{cm/s^2}. \tag{29}$$

Given what will be established about the expected spectrum of random accelerations in the experimental module, we expect this restriction to lie well below the requirements on the LTMPF. This effect is negligible for the proposed flight measurements.

Variations in the Temperature Induced by Density Fluctuations

The temperature of the system is also affected by density fluctuations induced by random accelerations of the ^{3}He sample. The relationship between density and temperature changes arises from the fact that the response of the system to random effective g-forces is fundamentally adiabatic. We start with the statement that there is no change in entropy associated with fluctuations in the temperature and volume of a system in the canonical ensemble

$$\begin{aligned}0 &= \Delta S \\ &= \left(\frac{\partial S}{\partial T}\right)_V \Delta T + \left(\frac{\partial S}{\partial V}\right)_T \Delta V\ .\end{aligned} \tag{30}$$

This allows us to associate a linear temperature change with small deviations in the volume of the system:

$$\Delta T = \frac{T\dfrac{\partial P}{\partial T}}{\rho^2 c_V}\Delta\rho\ . \tag{31}$$

Using Eq. (28) for density fluctuations induced by random accelerations, we end up with the following expression for the rms deviation of the temperature from its average value due to the adiabatic response of the system to AC-effective g-forces:

$$\Delta T_{rms} = \sqrt{\langle \Delta T^2\rangle} = 1.27\times10^{-7}\sqrt{\int\langle a(\omega)a(-\omega)\rangle d\omega}\ , \tag{32}$$

where the acceleration is measured in cm/s^2. Suppose we require that the rms temperature fluctuation be less than five parts in 10^8, which represents an AC deviation in temperatures equal to the expected experimental error. Then, we must have

$$\int \langle a(\omega)a(-\omega)\rangle d\omega \le 0.155 \ \ \mathrm{cm}^2/\mathrm{s}^4 \, . \tag{33}$$

According to this inequality, the total rms value of the acceleration must be less than $\sqrt{0.155} = 0.394$ cm/sec^2 = 4.02×10^2 μ*g*.

It is important to note that the above inequality on vibrations associated with induced temperature fluctuations represents a worst-case scenario. The actual experimental measurements involve an average over time. This averaging will significantly ameliorate the effects of AC temperature fluctuations. An estimate of the time-averaging effect that assumes a vibration spectrum consistent with the estimated ISS environment indicates that the effective variations in temperature will be reduced by approximately two orders of magnitude in a plausible experimental scenario. Thus, random accelerations associated with AC temperature fluctuations must be less than 4×10^4 μ*g* after taking into account time averaging.

Temperature Drift Due to Vibration-Induced Viscous Heating: Shear Viscosity

The equation for the maximum time rate of change of the temperature due to experimental cell accelerations is [40]

$$\begin{aligned} \frac{dT}{dt} &= \frac{D^2\eta}{C_S^4 \rho_c c_P}\int_{-\infty}^{\infty} \omega^2 \langle a(\omega)a(-\omega)\rangle d\omega \\ &= 3.8\times10^{-32}\,\frac{\mathrm{K}}{\mathrm{sec}} \times t^{\nu(2-\eta-x_\eta)}\int_{-\infty}^{\infty} \omega^2 \langle a(\omega)a(-\omega)\rangle d\omega, \end{aligned} \tag{34}$$

where C_s is the adiabatic sound velocity, η is the shear viscosity, x_η is the critical exponent for the weak divergence of the shear viscosity, and $a(\omega)a(-\omega)$ is the mean square acceleration per unit angular frequency. This rate of temperature rise decreases as the critical point is approached. As will be made clear shortly, the rate of increase of the temperature predicted by the above expression is completely negligible over the experimental reduced temperature range $10^{-6} < |t| < 10^{-1}$.

Temperature Drift Due to Vibration-Induced Viscous Heating: Bulk Viscosity

Bulk viscosity effects impose one of the most stringent constraints on the spectrum of vibrations. In contrast to the shear viscosity, the bulk viscosity displays a strong divergence as the critical point is approached. The expression for the rate of temperature increase that results from "bulk" viscous heating reduces to

$$\frac{dT}{dt} \approx 4.48\times10^{-29}\,\frac{\mathrm{K}}{\mathrm{s}} \times t^{\gamma-2\alpha-2}\int \omega^2 \langle a(\omega)a(-\omega)\rangle d\omega \, . \tag{35}$$

This relationship is obtained by substituting the coefficient of bulk viscosity for the shear viscosity on the right-hand side of the first line of Eq. (34). The right-hand side of Eq. (35) diverges as $t \to 0$. At a reduced temperature of 10^{-7}, we obtain from this equation

$$\frac{dT}{dt} \approx 4.5\times10^{-22}\,\frac{\mathrm{K}}{\mathrm{s}}\int \omega^2 \langle a(\omega)a(-\omega)\rangle d\omega \, . \tag{36}$$

If we assume that the rate of temperature increase is to be no greater than 10^{-6} K per week, then the following inequality must hold:

$$\int \omega^2 \langle a(\omega) a(-\omega) \rangle d\omega \leq 3.67 \times 10^9 \ \mathrm{cm}^2 / \mathrm{s}^6. \tag{37}$$

Finally, we turn to the limits on the vibration spectrum contained in Eqs. (37) and (29). Given the restriction in Eq. (33), we see that Eq. (29) represents a less stringent requirement on the vibration environment. As for the inequality in Eq. (37), an upper limit on the integral on the left-hand side is obtained by multiplying the integral in Eq. (33) by the square of the largest expected angular frequency, $\omega_{\max} = 2\pi f_{\max}$, where $f_{\max}$ ~ 100 Hz is well above the expected peaks in the vibration spectrum. This multiplicative factor is 3.95×10^5 s^{-2}. Incorporating this upper limit into the inequality, we are left with the requirement that the total integrated weight of random accelerations must be less than ~ 10^5 μ*g*. This requirement, that comes from the bulk viscosity-induced temperature drift, is comparable to the one associated with random AC temperature variations (~ 0.4×10^5 μ*g*) and is about 90 times greater than the integrated acceleration spectrum of 510 μg that represents the requirements for the LTMPF [39]. Thus, the conclusion drawn from this vibration analysis is that the expected vibration environment on the LTMPF should not adversely affect the proposed MISTE experiment. We have defined the MISTE requirement to be ≤ 5 μ*g* at DC and ≤ 1500 μ*g* rms total integrated acceleration over the range $10^{-3} < f < 500$ Hz.

3.9 *Heat Capacity Measurement*

Science requirements for the heat capacity measurement along the critical isochore are developed in this subsection. The heat capacity data far away from the critical temperature have an uncertainty mainly due to the temperature scale. The thermodynamic temperature scale is not known to better than 0.1%; therefore, the absolute accuracy of the temperature measurements is limited at this level. Accuracy of data very close to the critical point will also be affected by non-instrumental factors such as the gravity effect (see Fig. 3), being slightly off the critical isochore (see Fig. 6), thermal equilibration times (see Fig. 14), and cosmic ray heating (see subsection 3.8). In this section we will discuss instrumental accuracy/uncertainty and thermal relaxation times.

We have evaluated the drift and heat pulse methods for measuring the specific heat. Figure 16a shows a cooling drift run along the critical isochore that is consistent with earlier measurements [16]. In this study [41], a radiation shield whose temperature was controlled slightly below the critical temperature surrounded the sample stage. The sample was initially regulated at a reduced temperature of ~ 3.5×10^{-4} above the transition. Then the sample was cooled to the shield temperature after removing the cell temperature regulation. These data were taken with an average cooling drift rate of 3×10^{-4} K/hr. For this drift rate the overall density inhomogeneity in the sample due to the "piston effect" [27], which is in addition to the gravity stratification, is estimated to be ≤ 0.1% in the single-phase region.

A log-log plot of the drift data is shown in Fig. 16b. This figure clearly shows the rounding effect due to the earth's gravitational field, which is consistent with the prediction given in Table II. The rounding of the data close to the transition is dependent on the cooling drift rate, average

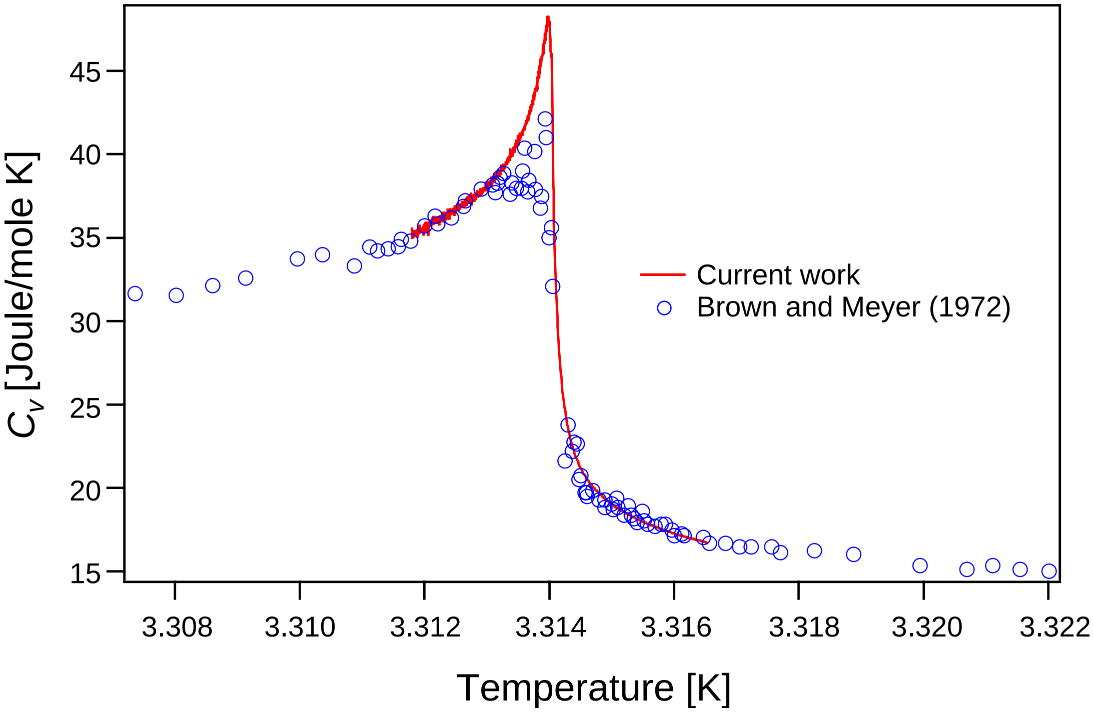

Fig. 16a. Cooling drift measurement of the heat capacity along the critical isochore.

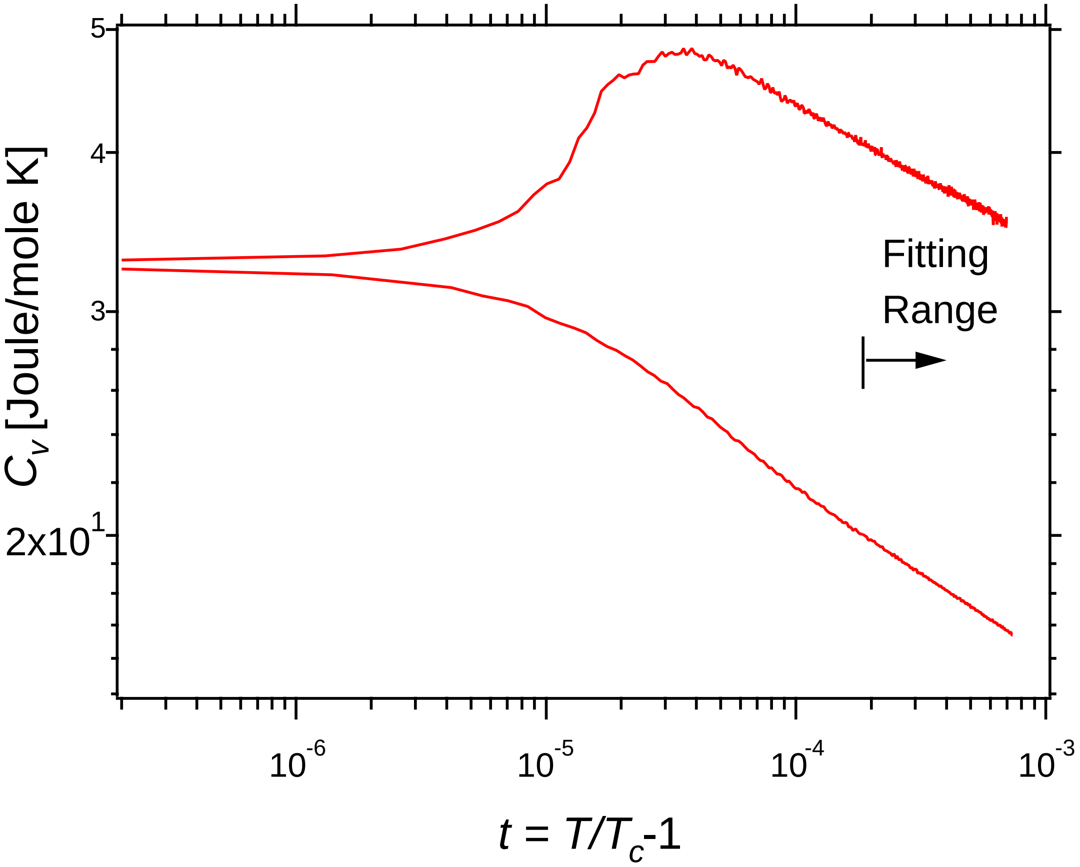

Fig. 16b. Log-log plot of heat capacity along the critical isochore.

density in the cell, and horizontal leveling of the cell. However, the 1% resolution in C_V within the single-phase region required for the flight experiment has been achieved. The drift method will be primarily used for measurements very close to the transition $t \leq 10^{-4}$. While these precision data were limited by gravity effects, we still performed a least square fit to the gravity free region. The fit to the data in the region $1.9\times10^{-4} < t < 7\times10^{-4}$, using the leading and first Wegner correction terms, yielded a leading asymptotic amplitude ratio $A_0^+/A_0^- = 0.509$ that is consistent with the theoretical value 0.523 within the combined uncertainties.

A second method that is planned for specific heat measurements throughout the critical region is the pulse technique. This method was successfully used in the LPE and CHeX experiments. Pulse measurements for ^{3}He near the critical point are shown in Fig. 17. The pulse heat used for both of these measurements was 2μJ. In each case, the temperature of the shield stage was initially controlled to keep the sample cell at a constant temperature before the pulse. At the pulse onset, the shield stage stopped controlling the sample cell and reverted to maintaining its own temperature constant. After a pulse, there is a dramatic difference in the transient temperature behavior between the single-phase and two-phase regions. The long time constant observed in the two-phase region is attributed to a redistribution of mass between the liquid and gas phases. The planned MISTE space flight cell, that is 8 times larger in volume than the ground-based cell, should lead to a further enhancement in the temperature stability. A complete

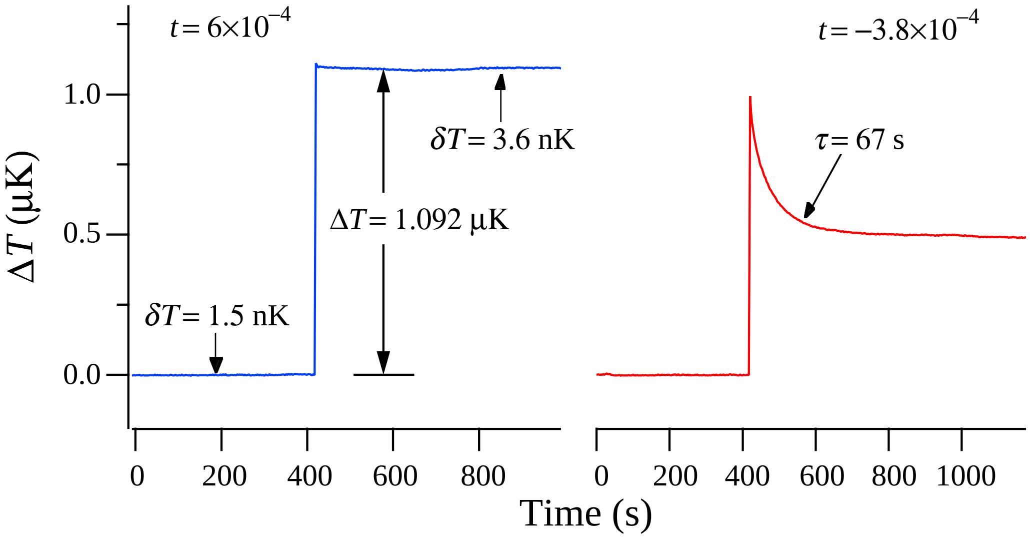

Fig. 17. Pulse measurements of the specific heat in both the one- and two-phase regions.

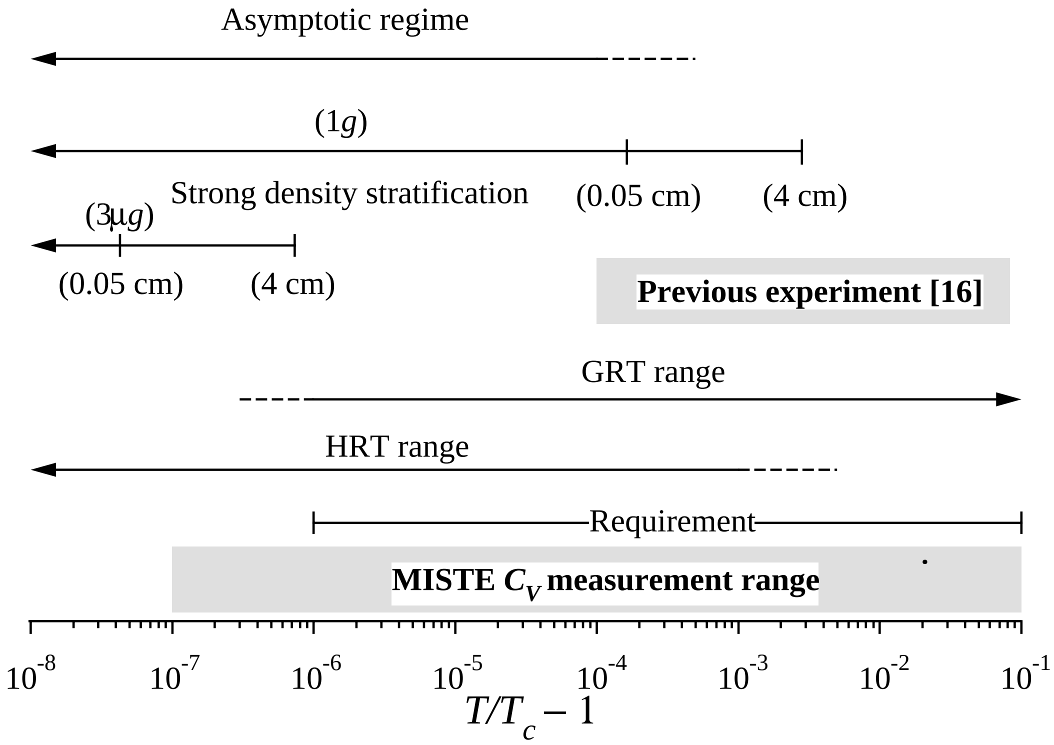

Asymptotic regime
(1g)
Strong density stratification
(0.05 cm)
(4 cm)
(3μg)
(0.05 cm)
(4 cm)
Previous experiment [16]
GRT range
HRT range
Requirement
MISTE C_V measurement range
10⁻⁸
10⁻⁷
10⁻⁶
10⁻⁵
10⁻⁴
10⁻³
10⁻²
10⁻¹
T/T_c − 1

Fig. 18. Factors affecting the measurement of specific heat at constant volume along the critical isochore for cell heights of 0.05 cm and 4 cm.

set of pulsed specific heat measurements along the critical isochore in the range $10^{-4} < t < 10^{-1}$ is now being carried out.

Figure 18 shows the important factors used in defining the C_V measurements. A 1% gravity effect on C_V measurements is shown for both a $1g$ and $3\mu g$ environment for the case of a cell of height 0.05 cm and a proposed flight cell of height 4 cm. The gravity free reduced temperature range is limited to $t > 7\times10^{-7}$ for the proposed 4 cm high flight cell. The graph also shows the range of application for GRT's and HRT's. Using HRT's allows 1% temperature measurements to be performed down to $t \sim 10^{-6}$. Analysis of previous ground-based C_V measurements [16] implies that the influence of confluent terms will be reduced to 1% at $t \approx 10^{-4}$. Thus, the experimental measurement range has the potential of covering at least two additional gravity-free decades.

The achievable C_V measurement range depends on how long it takes to reach thermodynamic equilibrium after a change in the system parameters. In estimating an effective equilibrium time constant, τ_2, one must take into account the "piston effect" [35] when performing measurements near a liquid-gas critical point. The "piston effect" applies to a sudden change in a constant volume cell with uniform temperature boundaries. This effect leads to a "critical speeding up" in the first stage of equilibration that usually lasts only a fraction of a second and produces almost complete temperature equilibration. However, the remaining small temperature gradient induces a measurable density gradient due to the diverging expansion coefficient. We have looked into the equilibration process for C_V measurement using the heat pulse technique. Using the theoretical models for the piston effect [27], we calculated the spatial and time profiles for temperature and density of ^{3}He under microgravity. This analysis showed that the effective relaxation time constant, τ_2, was very short (~ seconds even at $t = 10^{-7}$); thus, the measured specific heat is essentially the same as at the critical isochore.

We also plan to perform specific heat measurements in the two-phase region ($T < T_c$). In this region, a specific heat measurement should take a significantly longer time to reach final equilibrium (see Fig. 17). This is due to fluid mass moving across the meniscus and converting from one phase to another to accommodate the new equilibrium temperature. These effects will limit the ability to perform C_V measurements close to the critical point in the two-phase region. The stray heat associated with cosmic ray heating will also complicate the measurement of the specific heat because of the long equilibrium time. The pulse technique will be the primary method for measuring the specific heat in the two-phase region. Extrapolating experimental measurements of the time constant in the two-phase region to a microgravity environment yields a time constant of ~ 6 hours at $t = -10^{-5}$ for an effective cell height of 0.05 cm.

Taking all of the factors into account leads to a science requirement for measuring C_V to better than 1% in the single-phase range $10^{-6} \leq t \leq 10^{-1}$ and in the two-phase range $10^{-5} \leq -t \leq 10^{-1}$. In the remainder of this subsection we will discuss various factors that define the science requirements for performing the specific heat at constant volume experiments. For the flight experiment, we plan to emphasize the pulse technique over the drift technique. This decision is based on the adverse heating effects associated with cosmic rays (see subsection 3.8).

A. Heat Pulse

The accuracy of the heat pulse is an important factor for the C_V measurement. In order to be sure that the uncertainty in the measurement is not limited by the heat pulse measurement, we have chosen a goal of 0.05% for the accuracy of the pulse. The primary uncertainty in the pulse heat measurement is due to the measurement of the voltage applied to the heater and the pulse duration. It is anticipated that the LTMPF facility will provide instrumentation to achieve this requirement [39].

B. Temperature Step

The resolution of the temperature step height depends on the temperature range of the measurement. At $t = 10^{-6}$ we have a 1% requirement in the specific heat measurement. This is achievable using a temperature step height of $\Delta t = 10^{-7}$ that corresponds to $\Delta T = 3\times10^{-7}$ K. The 1% requirement in the temperature step is attained since we have a temperature resolution of ~ 1 nK. In most of the required experimental range ($10^{-5} \leq t \leq 10^{-1}$) the resolution will be much better than 1%.

C. Stray Heat Input

A 10^{-9} W stray heat input, specified in the LTMPF SRED, will cause a 2% error in the calculated heat capacity in the flight cell at the reduced temperature of $t \sim 10^{-7}$. However, in most cases ($10^{-6} \leq t \leq 10^{-1}$) the stray heat effect is negligible and will be averaged out by multiple runs in the single-phase region. The requirement for stray heat input is set at $< 5\times10^{-8}$ W.

3.10 Susceptibility Measurement

A. PVT Method

In preparation for the flight *PVT* measurements, we have developed an in-situ charcoal sorption pump for the ground-based studies (see Section 3.5). The pump is located on a separate thermal stage. Controlling the temperature (and thus the pressure) of the sorption pump varies the density of the sample. To obtain data along an isotherm, the sample stage is controlled at a desired temperature near the critical point while the sample is slowly removed from the cell by lowering the pressure in the sorption pump. This is accomplished by slowly reducing the sorption pump temperature from a nominal value (~ 20 K). When the temperature of the sorption pump reaches ~ 4 K, the sample density is approximately 20% below the critical value ($\Delta\rho \sim -0.2$). The cell can then be refilled to an initial density approximately 20% above the critical value ($\Delta\rho \sim 0.2$) by heating the sorption pump back to its nominal temperature. The P-ρ measurements are taken while the sample is being removed from the cell. Figure 19 shows an initial analysis of P-ρ measurements along several isotherms near the critical point in the range $-4.7\times10^{-3} < t < 3\times10^{-3}$. The density ramping rate was typically 5 - 10 hours for a given isotherm. The isotherms near the critical temperature were measured at several different ramping rates to insure quasi-thermodynamic equilibration. In the space flight experiment, different ramping rates will be used to find the optimal rate for temperatures very near the critical point.

For $T < T_c$, Fig. 19 clearly shows the phase boundary defining the coexistence curve. From

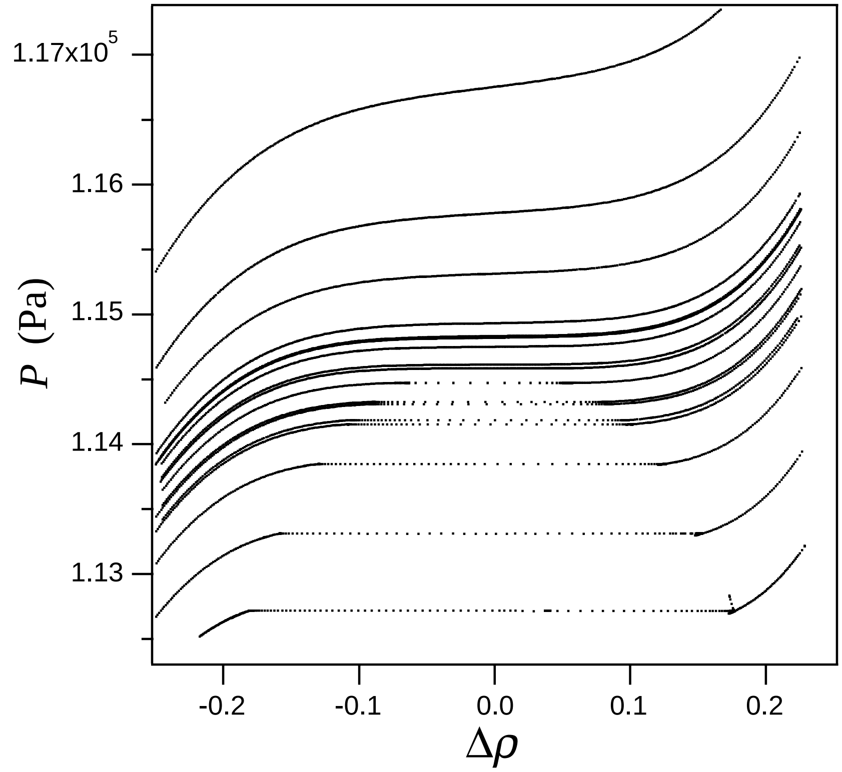

Fig. 19. P-ρ measurements along isotherms near the critical point of ^{3}He.

the discontinuities in $(\partial P/\partial \rho)_T$, we can determine the coexistence curve to within ~ 0.1%. From asymptotic and crossover coexistence data obtained during the flight experiment, we should be able to determine the critical amplitudes B_0 and B_1. Also, by deriving $(\partial P/\partial \rho)_T$ in the single-phase region at the coexistence curve discontinuities, we can obtain the susceptibility along the coexistence curve, in the liquid and gas phases, from which the critical amplitudes Γ_0^- and Γ_1^- can be determined.

Figure 20 shows the calculated susceptibility obtained from *PVT* measurements at $t = 1.31\times10^{-3}$. The open circles, corresponding to the right axis in the plot, represent the susceptibility obtained from the slope of the *P*-*ρ* curve. The maximum value of the susceptibility, which occurs at the inflection point in the *P*-*ρ* curve, is within 0.1% of the critical density. On the ground, the critical density is determined at a smaller reduced temperature of ~ 6×10^{-4}, which is close to the onset of the gravity rounding effect (see subsection 3.6). This *P*-*ρ* inflection point method has been used in previous studies [26]. However, a better determination of the critical density will be possible during the flight experiment where the gravity effect will be minimized.

Figure 21 shows the calculated susceptibility along the critical isochore obtained from *PVT* measurements over the range of $2.5\times10^{-5} < t < 1.5\times10^{-1}$. As can be seen from the figure, the data are consistent with the earlier work of Meyer's group [18,42]. The improved leveling of the experimental cell permitted gravity-free measurements to be performed closer to the transition (see subsection 3.6). The data are now being analyzed to determine the leading asymptotic critical amplitude Γ_0^+ and first Wegner correction-to-scaling amplitude Γ_1^+. We are also using this

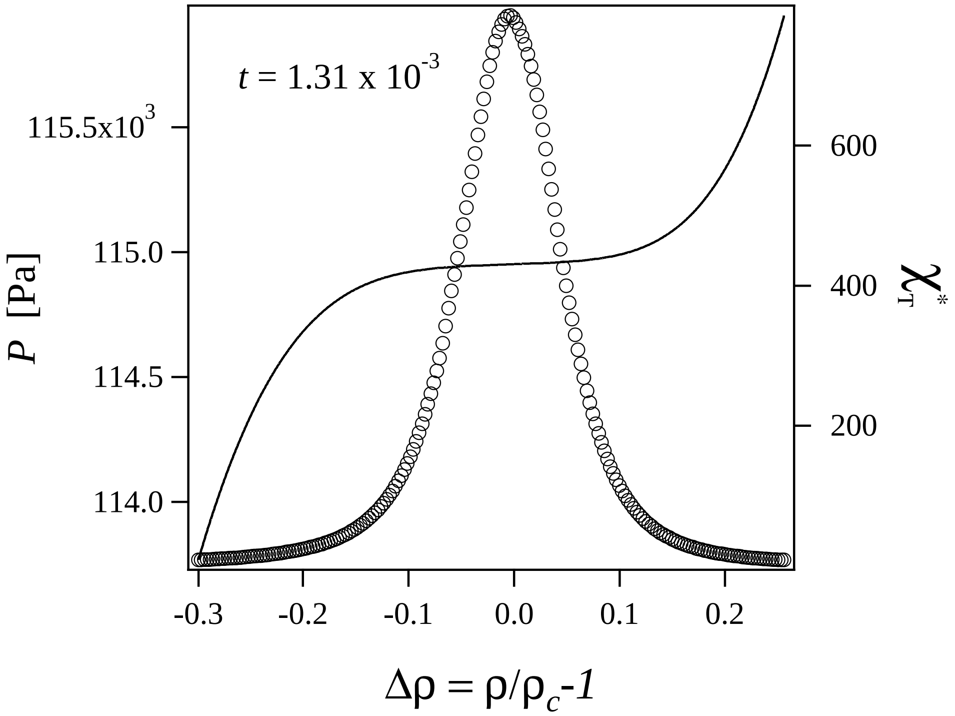

Fig. 20. Calculated susceptibility from *P*-*ρ* measurements along an isotherm.

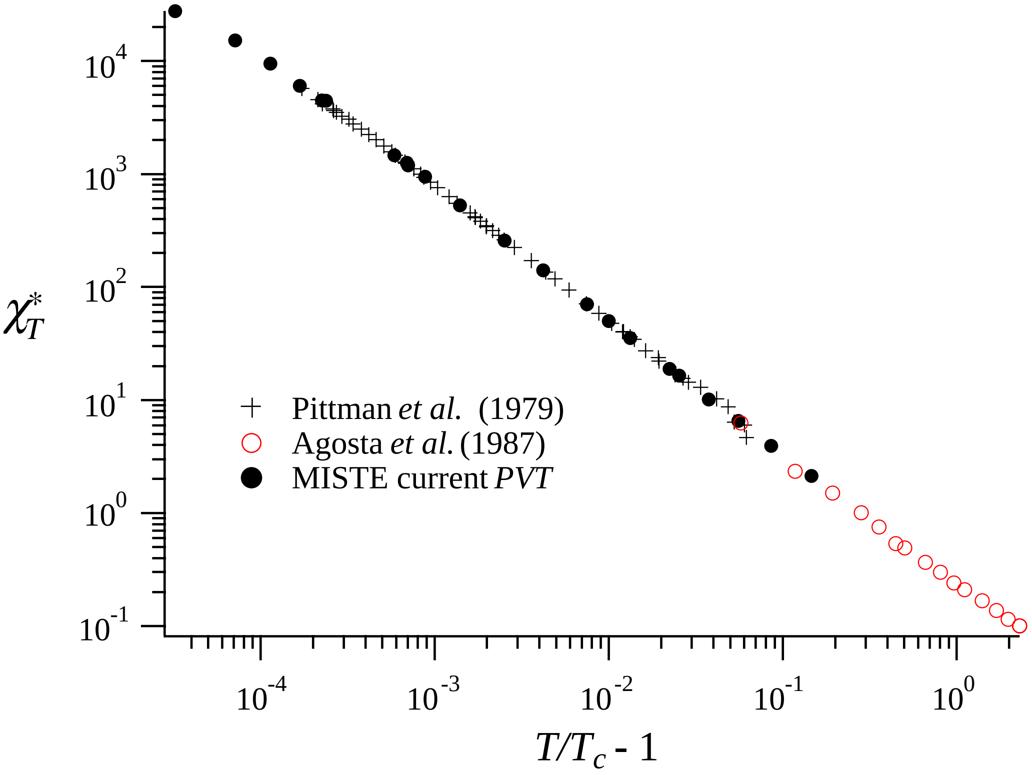

Fig. 21. Calculated susceptibility along the critical isochore from P-ρ measurements.

data set to test the application of an RG crossover model [23].

B. Electrostriction technique

While the susceptibility χ_T along the critical isochore can be derived from *PVT* measurements, a pressure resolution of $\delta P/P \approx 1{:}10^{10}$ is required to measure χ_T with 1% uncertainty at $t \approx 10^{-6}$ (see Appendix B). This pressure resolution is very difficult to attain using conventional means. We have been evaluating a new electrostrictive technique to attain this required pressure resolution [41]. This technique takes advantage of the fact that an electric field gradient can produce an equivalent pressure gradient within a dielectric fluid. A DC voltage, V, is applied across the density sensing capacitor to create an electric field in the capacitor gap. The induced pressure produces a density change. This density change can be detected by a capacitance change ΔC.

An example of the electrostriction effect near the ^{3}He critical point is shown in Fig. 22. Density changes are shown for a DC bias ranging from 10 - 40 volts. After the DC bias is turned on or off, the capacitance initially experienced an abrupt change followed by a transient that in the final equilibration stage can be fit by an exponential function. The equilibrium capacitance was extrapolated from the fit. The capacitance change for a particular DC bias was corrected for the structural capacitance change caused by the DC voltage applied across the gap. By plotting

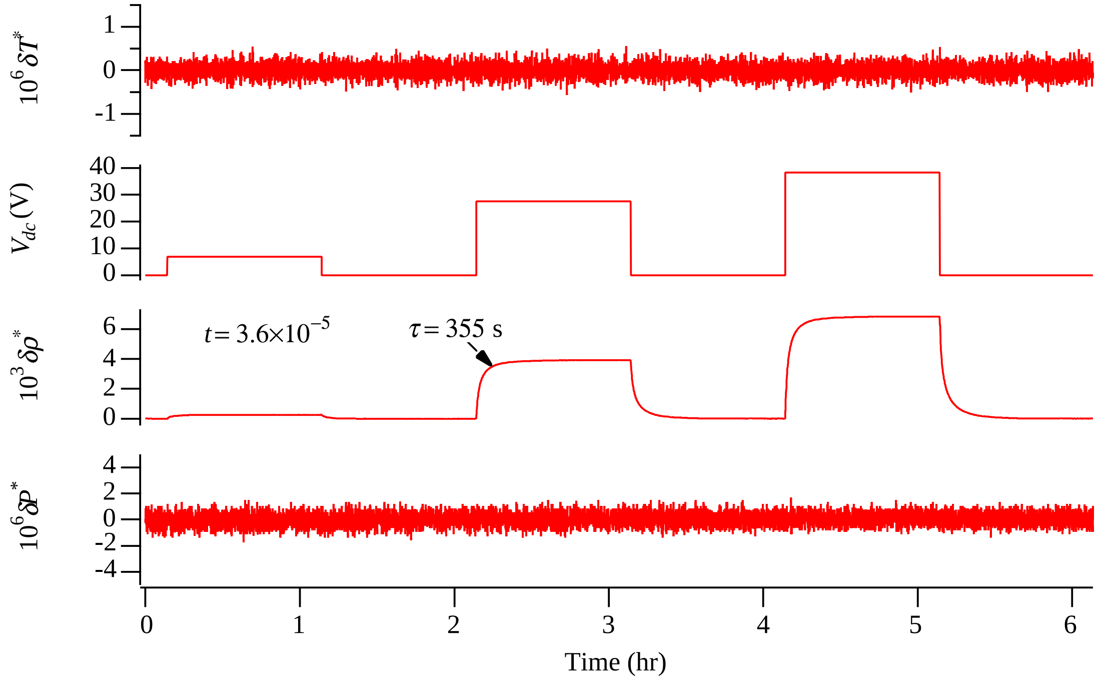

Fig. 22. Electrostriction effect at $t = 6.6\times10^{-5}$.

the measured capacitance change ΔC versus the square of the total rms voltage, including both the DC bias and the excitation voltage across the capacitor, we obtain $\lim_{V_{\text{total}}\to 0} \Delta C / V_{\text{total}}^2$, which is used to calculate the susceptibility without the systematic error caused by nonlinear effects close to T_c. For the details on the data analysis of the electrostrictive technique see Appendix B. The susceptibility measured using the electrostriction technique agrees with the one measured using the *PVT* technique to within 10% in the region where the two overlap, which is consistent with the expected uncertainty in the absolute value of the capacitance gap used to calculate the electric field. The data shown in Fig. 22 have a rather long relaxation time to reach the final equilibrium state after the application or removal of a DC bias. We have taken this equilibrium time constant into account in developing the experimental measurement scenario for the flight experiment.

Figure 23 shows a log-log plot of the effective susceptibility versus reduced temperature. The rounding at $t < 10^{-4}$ is consistent with the prediction given in Table II. An additional contribution to this rounding could be due to a slight tilt of the cell. In the presence of gravity, such a tilt leads to an increased density deviation from ρ_c at the capacitor location as T_c is approached. However, this tilt effect was significantly reduced for this study by applying the leveling procedure described in subsection 3.6. An initial study demonstrated the viability of using this electrostriction technique for future microgravity experiments very near the transition [44].

In Fig. 24 we show a summary of important factors associated with the measurement of the susceptibility along the critical isochore. In the flight experiment, we plan to use two techniques to measure χ_T, the electrostrictive (ES) technique, and a conventional *PVT* technique. The electrostrictive technique will be the main method for measuring the susceptibility close to T_c.

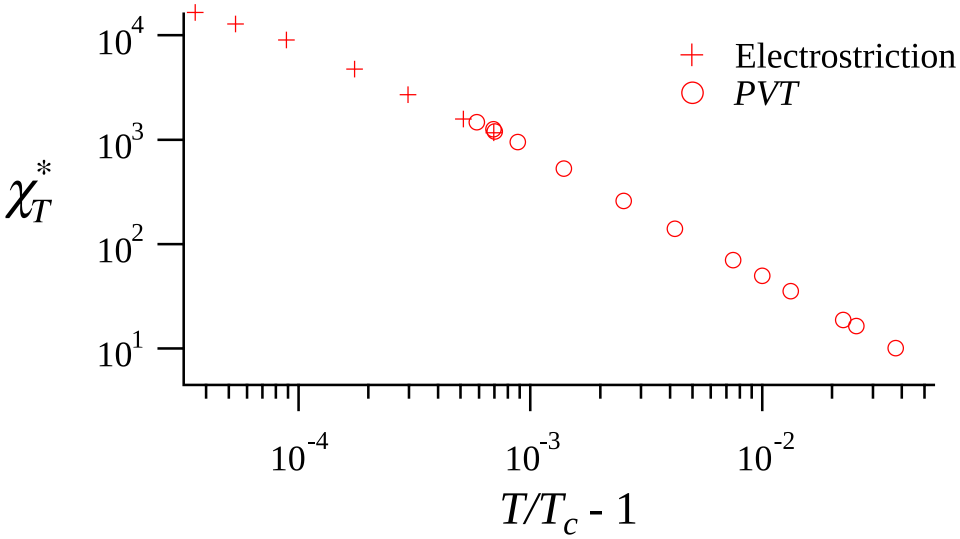

Fig. 23. Effective susceptibility versus reduced temperature.

The conventional technique will primarily be used to measure the susceptibility farther away from the transition, and to calibrate the electrostrictive technique within the temperature range where the two methods overlap. The smallest reduced temperature, for which the ES technique can be used, was determined from the expected systematic error associated with being off the critical isochore. From that analysis we find that the ES technique is capable of covering the reduced temperature range $6\times10^{-7} \leq t \leq 4\times10^{-3}$. The reduced temperature ranges for the *PVT* and electrostriction techniques are shown in Fig. 24.

A capacitor with a gap of d = 50 µm will be used to measure the density in the flight cell. The dependence of the theoretical diffusive relaxation time associated with density changes in the capacitor gap is shown in Fig. 24 as a function of reduced temperature. It is seen that this diffusive relaxation time is expected to be only a few minutes even at $t \sim 10^{-7}$. However, the present measurements using the electrostriction technique show a much longer relaxation time after the application or removal of a DC bias. An investigation of this long relaxation time was initially performed using a density sensor that was essentially thermally isolated from the cell walls. That study indicated the measured relaxation time was consistent with an effective height equal to the cell height and not the capacitor gap. A new density sensor design, having a significantly improved thermal link to the cell walls, has recently been tested. The measured time constant for the new density sensor is ~ 5 times smaller than the previous sensor. We have taken these experimental time constants into account in developing our flight measurement scenario to fit within the allotted experimental timeline.

The reduced temperatures associated with a 1% error in χ_T due to gravity effects (see Fig. 4a) are also shown in Fig. 24 under 1g and 3µg conditions for the cases of the present 0.05 cm high cell and the proposed maximum 4 cm high flight cell. For the proposed 4 cm high flight cell, the gravity-free reduced temperature range is limited to $t > 7\times10^{-7}$.

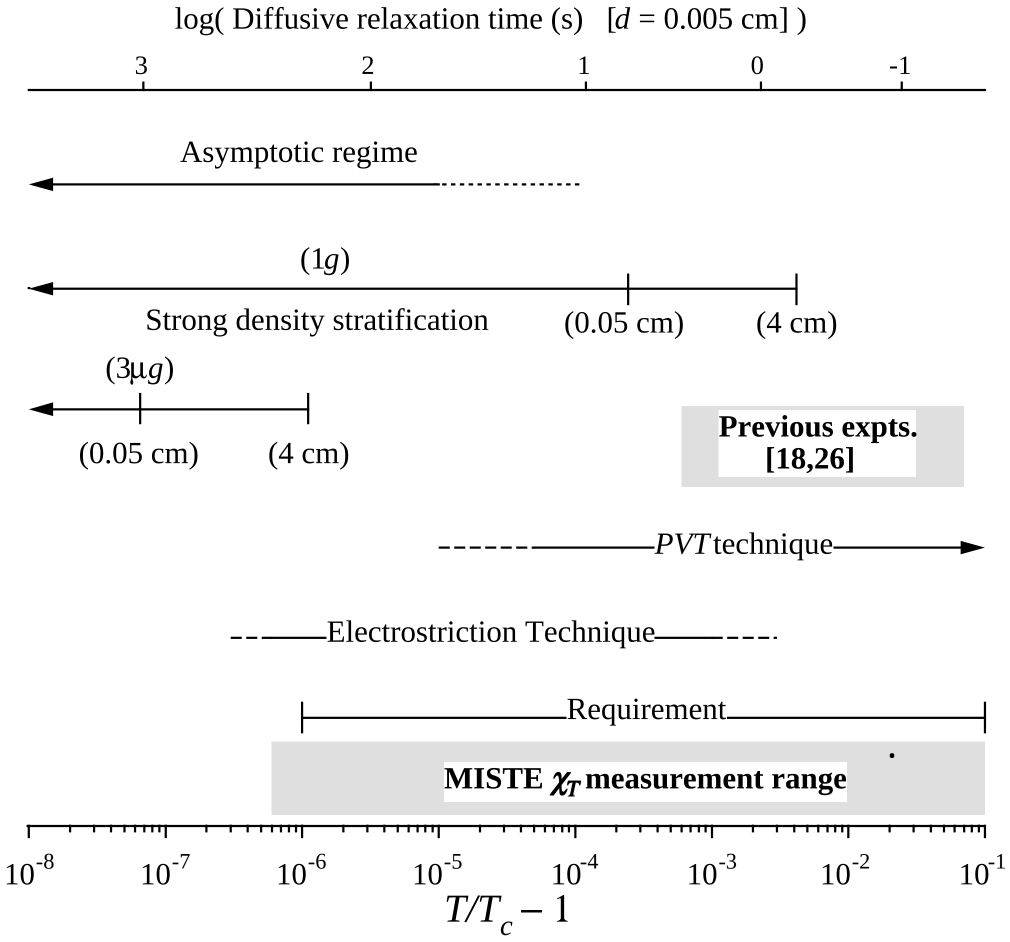
log(Diffusive relaxation time (s) [d = 0.005 cm])
3
2
1
0
-1
Asymptotic regime
(1g)
Strong density stratification
(0.05 cm)
(4 cm)
(3μg)
(0.05 cm)
(4 cm)
Previous expts. [18,26]
PVT technique
Electrostriction Technique
Requirement
MISTE χT measurement range
10-8
10-7
10-6
10-5
10-4
10-3
10-2
10-1
T/Tc – 1

Fig. 24. Factors affecting the measurement of susceptibility along the critical isochore.

An experimental estimate of the onset for the asymptotic region can be quite uncertain because it is based on the data outside the asymptotic region and the gravity effect excludes measurements close into the transition. The dashed line in Fig. 24 reflects this uncertainty in the onset of the asymptotic region.

Taking into account the various factors influencing the susceptibility measurement leads to a required MISTE flight experimental measurement range of $10^{-6} \leq t \leq 10^{-1}$, which is shown at the bottom of Fig. 24. It is seen that the flight experiment is expected to provide accurate susceptibility measurements for approximately two and a half additional decades in reduced temperature closer to the critical point than previous ground-based measurements [18,26].

A. Measurements Along the Critical Isotherm

The asymptotic critical exponent δ and critical amplitude D will be determined from measurements of P and ρ along the critical isotherm. Susceptibility measurements will yield an exponent whose value equals δ - 1 (see Appendix B). Again we plan to use the electrostriction technique as the main method for measuring the susceptibility along the critical isotherm close to the critical point.

A summary of the important factors that affect these measurements along the critical isotherm is shown in Fig. 25. Shown in this figure is the electric field E as a function of the reduced density $\Delta\rho$ that is required to induce a density change $\delta\rho = 5\times10^{-4}$ at each reduced density. This density change was chosen to keep the uncertainty in the susceptibility measurement under 1%. The required rms voltage across a capacitor with a gap size of d = 50 μm is also shown in the figure. We anticipate using a maximum of 200 V for the electrostriction technique, which implies experimental measurements can be performed up to a reduced density

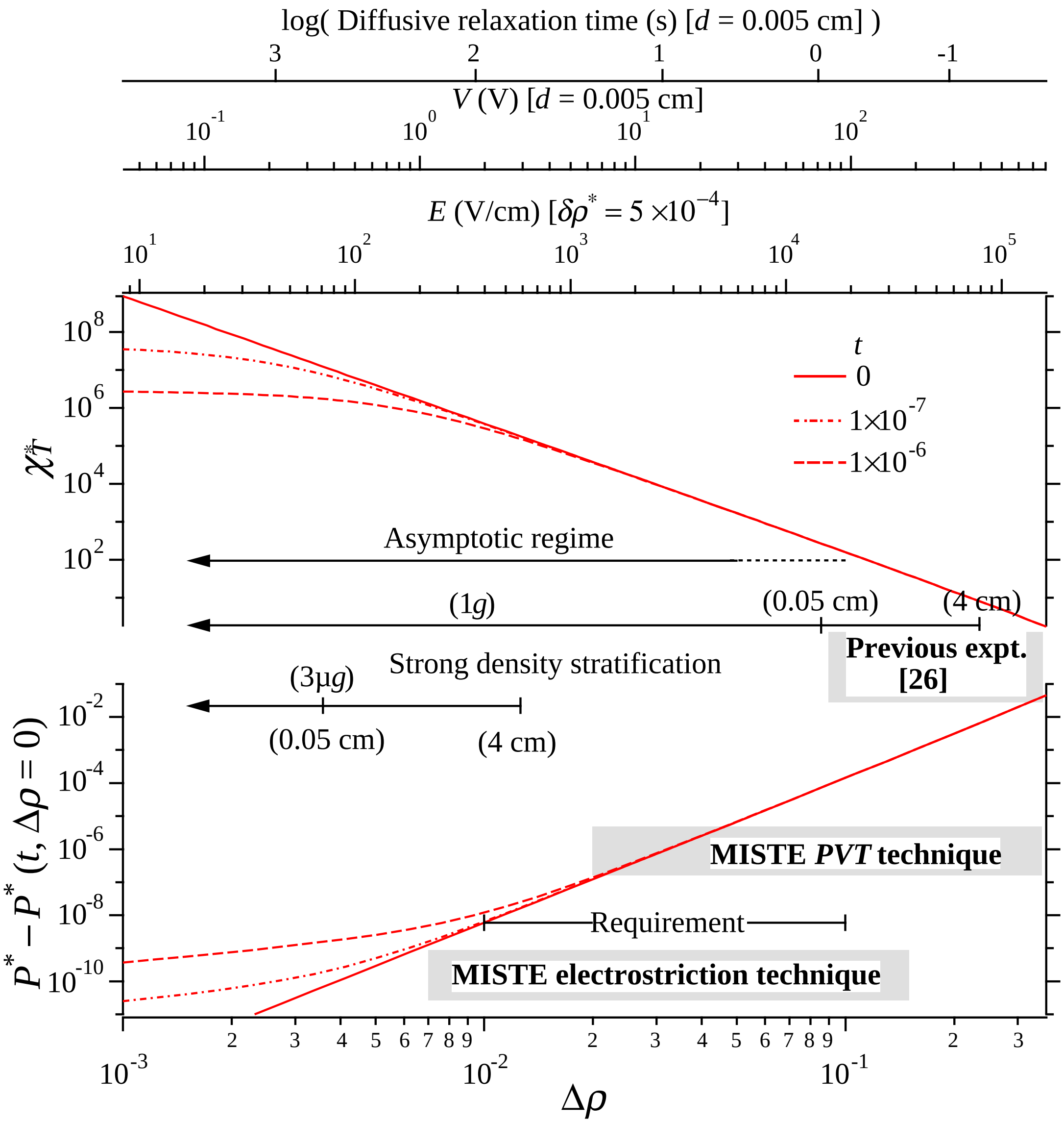

Fig. 25. Factors affecting P, ρ measurements along the critical isotherm. The * indicates a dimensionless quantity.

of $\Delta\rho$ = 0.15. The dielectric breakdown of ^{3}He occurs at $E = 4\times10^5$ (V/cm) based on the information obtained for ^{4}He. Since the maximum E field for a 200 V DC bias applied on a gap of 50 μm is 3×10^4 V/cm, the breakdown should not be a concern for the proposed critical isotherm measurements. Possible interference from cosmic ray particles on dielectric breakdown is being investigated. For $\Delta\rho < 7\times10^{-3}$ and within $t = 3\times10^{-7}$, the systematic error in determining δ will be more than 1% (see also Fig. 8). Therefore, the limit of the ES technique ($\Delta\rho = 7\times10^{-3}$) is set by the uncertainty in the MISTE goal to determine the critical isotherm within $t \approx 3\times10^{-7}$. If the critical temperature, T_c, could only be determined within $|t| \leq 8\times10^{-7}$ from the susceptibility and specific heat measurements along the critical isochore, a conservative lower limit of $|\Delta\rho| \geq 10^{-2}$ is required for using the electrostriction technique. As it can be seen from Fig. 25, even for an isotherm at $t = 8\times10^{-7}$, the susceptibility measurements will be essentially equivalent to that of the critical isotherm for $\left|\Delta\rho\right| \geq 10^{-2}$.

The conventional *PVT* method will be used primarily for the critical isotherm measurement for $\left|\Delta\rho\right| \geq 5\times10^{-2}$. It will also be used to calibrate the ES technique where the two overlap. The dependence of the diffusive relaxation time is shown at the top of Fig. 25, now as a function of reduced density. This relaxation time is again expected to be only a few minutes even at $\Delta\rho = 7\times10^{-3}$. As stated above, a much longer relaxation time was observed in our ground-based measurements, and these long time constants are taken into account in developing the flight experiment scenario.

The reduced densities associated with a 1% error in χ_T due to gravity effects (see Fig. 4b) are also shown in Fig. 25 for 1g and 3μg conditions for the case of the present 0.05 cm high cell and the proposed maximum 4 cm high flight cell. For the present cell, a μg environment would permit susceptibility measurements to be extended by approximately one and a half decades in reduced density closer to the critical point without gravity rounding effects. The gravity-free reduced density range is limited to $|\Delta\rho| \geq 10^{-2}$ for the proposed 4 cm high flight cell. The dashed line in Fig. 25 reflects the uncertainty in the onset of the asymptotic region.

Taking into account all of the factors discussed above, one can see that the required reduced density range of $10^{-2} \leq |\rho/\rho_c - 1| \leq 10^{-1}$ for the MISTE flight experiment will enable measurements approximately one additional decade closer to the critical point than previous ground-based measurements [26].

4. EXPERIMENT TIMELINE AND DATA ACQUISITION

4.1 Measurement Plan

This section contains an outline of our baseline measurement scenario. This baseline plan will meet all the MISTE science data requirements and some of the goals within a planned 4.5 month LTMPF data-taking period. The plan can also be extended or compressed if the on-orbit lifetime is different than expected or if station environments are not as predicted. After the LTMPF is launched and positioned on the JEM-EF, initial turn on will be followed by about 5 days of functional checks, calibrations, and orbital environment characterization (charged particle effects and vibration) before scientific studies commence.

The experimental cell will initially be filled to a near-critical density on the ground using the techniques we have already developed (see subsection 3.5). The first microgravity measurements will be made along this near-critical isochore. Full sets of specific heat and electrostriction susceptibility measurements will provide a significant initial data set. The data will be used to determine the critical temperature, T_c, and provide preliminary data on the asymptotic critical amplitudes, A_0^+ and Γ_0^+, and critical exponents, α and γ. These measurements will be followed by investigations of any unexpected effects.

In the next phase, the low-temperature valve will be opened and remain open for a complete set of measurements along isotherm paths. The sample density will be controlled using an in-situ transfer system (see Section 3.5). These measurements will produce a wealth of equation-of-state data throughout the critical region, including susceptibility information along the critical isochore, critical isotherm, and coexistence curve. Isotherms below the critical temperature will probe the coexistence curve. The baseline plan calls for a full set of isotherm data to be completed, followed by investigations of any observed anomalies before the valve is closed again. A much more accurate, microgravity-determined value for the critical density will be obtained from an analysis of the early flight isotherm data. In the next phase, the cell will be filled to the newly determined ρ_c value and the valve will be closed again.

A complete set of heat capacity data in the one- and two-phase regions and electrostriction data will be taken at ρ_c next. As a contingency, if the preflight fill density turns out to be far from the true ρ_c, these critical isochore measurements may be shifted earlier in the schedule to a point before the bulk of the isotherm measurements. This will ensure that T_c is accurately known during the critical isotherm experiments.

During the final period of the measurement schedule, the low-temperature valve will be exercised many more times to probe isochores progressively farther above and below ρ_c. In this way degradation of the valve with cycling will have minimal impact. Along each isochore, drift and pulse specific heat data will be taken. Electrostriction measurements will also be taken at and near T_c along most of the isochores.

In this measurement plan, all science activities are counted with a minimum of 10% allowance for SAA passes. For some of the data nearest the critical point we allowed up to a factor of two increase in the time required because of possible charged particle heating disturbances. Our current plan assumes that the ISS will be completely assembled at the time of the LTMPF-M1 flight. Calculations show that MISTE is not extremely sensitive to vibrations (see subsection 3.8), so we have assumed that data can be taken during 80% of the "nonmicrogravity-mode" station time (which is about half of the total time). Given this, we should be able to take a considerable amount of data even if the experiment begins in the more vibration-plagued period before station completion. The plan for the initial period of system checkout and calibration contains significant allowance for loss of telemetry contact with the ISS, since these activities will probably be done near-real-time to watch for anomalies. After this initial period, the system is expected to be automated enough that no significant loss of time due to telemetry blackout is anticipated.

With these allowances for disturbances, our baseline data set will be completed within 4.5 months, including time specifically held for investigating anomalies or unexpected and interesting effects. The baseline scenario meets all MISTE experimental data requirements and some of the desired goals. In the event of a reduced available measurement period, the range of the data at temperatures and densities farther from the critical point will be restricted. On the other hand, additional time could become available either because of better-than-expected dewar performance or less charged particle or vibration impact than anticipated. Under these circumstances, the baseline data measurements could be repeated for statistical error reduction, and data acquisition could be extended to regions farther from the critical point. Other effects such as supercooling into the two-phase region could also be investigated if time permits.

4.2 Data Requirements

This section addresses the three different types of data requirements.

A. Instrument Data

In order to optimize data collection during the mission, it is important to maintain real-time command and data telemetry with the experiment. Unfortunately, the coverage of the relevant Ku communication band for the ISS is expected to be much lower than similar coverage for the shuttle, approximately 70% per orbit, on average. Therefore, it is extremely important to establish optimum data collection and command strategy for the experiment as early as possible during the mission. For previous space shuttle experiments (LPE, CHeX), the decisions regarding the data acquisition strategy could be made by evaluating data inputs after about 3 days of flight time. It is obviously impossible to simulate everything about the mission because proposed functionality of the ISS is still in transition and may not be available before the flight. In the flight experiment we plan to optimize the command and telemetry sequence for the data collection after about 1 week of flight time. This early flight study will provide appropriate inputs regarding ISS telemetry capabilities/coverage and the regions of the orbit where environmental effects are at a minimum. We believe that this strategy is quite adequate for the experiment on ISS because of the expected long duration (~ 3 - 6 months).

B. Environmental Data

It is very important to obtain environmental data during each orbit. Charged particle data should be monitored during the experiment to optimize the data acquisition plan and to look for sources of heat input to the experimental cell. It will also be necessary to perform checks of the acceleration environment to look for the possible adverse effects on the experiment, such as vibration heating effects during the heat capacity measurements. In addition to a full spectrum of the vibration environment, it is desirable to have the real-time peak acceleration vector amplitude data transmitted to the instrument computer system to be correlated with the main science data.

C. ISS Data

For the post-flight data analysis activity, it will be desirable to have data on the ISS location and attitude as a function of mission elapsed time. It is also important to know the actual direction and magnitude of the gravity vector at the LTMPF on JEM as a function of time. Also, records should be kept on the time of high-acceleration events such as docking events on the ISS and attitude control reboosting events. These events will need to be cross-correlated with the main science data.

4.3 Mission Success Criteria

A. 100% Science Return

A 100% science return will require:

(a) Two measurement scans (each containing at least 5 data points per decade in reduced temperature) of the specific heat at constant volume and the isothermal susceptibility along the critical isochore ($|\Delta\rho| \leq 10^{-3}$) over the reduced temperature range $|t| \leq 10^{-3}$. The critical point should be approached to within a reduced temperature of $t = 10^{-6}$ in the one-phase region and within $t = -10^{-5}$ in the two-phase region.

(b) Two measurement scans (each containing at least 30 data points) of the isothermal susceptibility along the critical isotherm ($|t| \leq 8\times10^{-7}$) over the reduced density range $|\Delta\rho| \leq 10^{-1}$. The critical point should be approached to within a reduced density of $|\Delta\rho| \leq 10^{-2}$.

(c) Measurements of the specific heat at constant volume and the isothermal susceptibility in the critical region along non-critical paths. The specific heat at constant volume should be measured along at least four non-critical isochores in the reduced density range $|\Delta\rho| \leq 10^{-1}$. The isothermal susceptibility should be measured along at least twelve non-critical isotherms (six in the one-phase region over the reduced temperature range $5\times10^{-5} \leq |t| \leq 5\times10^{-4}$ and six in the two-phase region over the reduced temperature range $1\times10^{-5} \leq |t| \leq 5\times10^{-4}$). At least 20 data points each for the specific heat at constant volume and the isothermal susceptibility are required along each path.

(d) At least six isothermal susceptibility and density measurements along the liquid and gas sides of the coexistence curve obtained from the six two-phase isotherms in (c) above.

B. Minimum Science Return

For the minimum science return, the 100% requirements above will be reduced as follows:

(a) Only one measurement scan will be required with the critical point being approached to within a reduced temperature of $t = -3\times10^{-5}$ in the two-phase region.

(b) Only one measurement scan will be required with the critical point being approached to within a reduced density of $|\Delta\rho| = 2\times10^{-2}$.

(c) Only two non-critical isochores will be required for specific heat at constant volume measurements, and only eight non-critical isotherms will be required for the isothermal susceptibility measurements.

(d) Only four isothermal susceptibility and density measurements along the liquid side of the coexistence curve will be required.

5. *REFERENCES*

1. Wilson, K.G., *Phys. Rev*., **B4**, 3174, 3184 (1971); Wilson, K.G. and Kogut, J., *Phys. Rev*., **12C**, 75 (1974).
2. Fisher, M.E., *Phys. Rev. Lett.* **16**, 11 (1966); Kadanoff, L.P., in *Phase Transitions and Critical Phenomena*, edited by C. Domb and M.S. Green (Academic, New York), Vol. 5A, Chap. 1 (1976).
3. Widom, B.J., *Chem. Phys*. **43**, 3898 (1965); Griffith, R.B., *Phys. Rev*. **158**, 176 (1967); Stanley, H.E., *Introduction to Phase Transitions and Critical Phenomena*, (Oxford University Press, New York (1971)).
4. Guida, R., and Zinn-Justin, J., *J. Phys. A Math. Gen.* **31**, 8103 (1998) and references therein.
5. Chen, J.H., Fisher, M.E., and Nickel, B.G., *Phys. Rev. Lett.* **48**, 630 (1982).
6. Fisher, M.E., and Zinn, S.-Y., *J. Phys. A Math. Gen.* **31**, L629 (1998) and references therein.
7. Fisher, M.E., and Zinn, S.-Y., *Phys. Rev. B* **59**, 14533 (1999).
8. Wegner, F., *Phys. Rev*., **B5**, 4529 (1972).
9. Le Guillou, J.C., and Zinn-Justin, J., *J. Phys. (Paris)* 48, 19 (1987).
10. George, M.J. and Rehr, J.J., *Phys. Rev. Lett.*, **53**, 2063 (1996).
11. Zinn, S.-Y., and Fisher, M.E., *Physica, A* **226**, 168 (1996).
12. Patashinskii, A.Z., and Pokrovskii, V.L., *Fluctuation Theory of Phase Transitions*, Pergamon, Oxford (1979).
13. Ley-Koo, M., and Green, M.S., *Phy. Rev. Lett.*, **26**, 1155 (1971).
14. Bagnuls, C., and Bervillier, C., *Phys. Lett.* **107A**, 299 (1995).
15. Anisimov, M.A., Kiselev, S.B., Sengers, J.V., and Tang, S., *Physica A* **188**, 487 (1992).
16. Brown, G. R. and Meyer, H., *Phys. Rev.* **A6**, 364 (1972).
17. Straub, J., and Haupt, A., *Phys. Rev. E* **59,** 1795 (1999); Straub, J., Eicher, L., and Haupt, A., *Phys. Rev. E* **51,** 5556 (1995).
18. Pittman, C., Doiron, T., and Meyer, H., *Phys. Rev. B***20**, 3678 (1979).
19. Tang, S., Sengers, J.V., and Chen, Z.Y., *Physica A* **179**, 344 (1991); Nickel, B., and Dixon, M., *Phys. Rev. B* **26**, 3965 (1982).
20. Anisimov, M.A., Gorodetskii, E.E., Kulikov, V.D., and Sengers, J.V., *Phys. Rev. E*, **51**, 1199 (1995).
21. Dohm, V., *Z. Phys.* B **61**, 61 (1985); Schloms, R., and Dohm, V., *Nucl. Phys.* B **328**, 636 (1989); Krause, H.J., Schloms, R., and Dohm, V., *Z. Phys.* B **79**, 287 (1990).

22. Dohm, V., *J. Low Temp. Phys.* **69**, 51 (1987); Dohm, V., *Proceedings of the 1997 NASA/JPL Workshop on Fundamental Physics in Microgravity*, Santa Barbara, May 7-9, 1997.

23. Haussmann, R., private communication.

24. Hocken, R.J., and Moldover, M.R., *Phys. Rev. Lett.* **37**, 29 (1976); Levelt Sengers, A., Hocken, R., and Sengers, J.V., *Physics Today* **30**, (12), 42 (1977).

25. Fisher, M.E., *Phys. Rev. Lett.* **16**, 11 (1966).

26. Wallace, B. Jr., and Meyer, H., *Phys. Rev. A***2**, 1563 (1970).

27. Zhong, F., and Meyer, H., *Phys. Rev. E,* **51**, 3223 (1995); Zhong, F., and Meyer, H., *Phys. Rev. E,* **53**, 5935 (1996) and references therein.

28. Moldover, M.R., Sengers, J.V., Gammon, R.W., and Hocken, R.J., *Rev. Mod. Phys.*, **51**, 79 (1979).

29. Barmatz, M., Hahn, I, Zhong, F., and Rudnick, J, *Proceedings of the 1997 NASA/JPL Workshop on Fundamental Physics in Microgravity*, JPL internal Document D-15677, p. 80 (1998) and Rudnick, J., private communication.

30. Barmatz, M., and Hahn, I, *Proceedings of the 1996 NASA/JPL Low Temperature Microgravity Physics Workshop*, JPL internal Document D-13845, p. 53 (1997).

31. Doiron, T., and Meyer, H., *Phys. Rev. B***17**, 2141 (1978).

32. Berg, R. F., Moldover, M. R., and Zimmerli, G. A., *Phys. Rev. E.*, **60** , 4079 (1999).

33. Straty, G.C., and Adams, E.D., *Rev. Sci. Instrum.* **40**, 1393 (1969).

34. Sprague, D.T, and Smith, E.N., *J. Low Temp. Phys* **113**, 975 (1998).

35. Straub, J., Eicher, L., and Haupt, A., *Phys. Rev. E* **51**, 5556 (1995); Boukari, H., Pego, R., and Gammon, R., *Phys. Rev. E,* **52**, 1614 (1995); Kogan, A.B., and Meyer, H., JLTP **112 (5/6)**, 417 (1998).

36. Cohen, L.H., and Meyer, H., *Phys. Rev. A***38**, 2081 (1988).

37. Onuki, A., Hao, H. and Ferrell, R.A., *Phys. Rev. A* **41**, 2256 (1990).

38. Private communication from Steve Boyd.

39. *LTMPF Science Requirements Envelope Document* (SRED), JPL internal Document D-16322, (1999).

40. Cowan, M., Rudnick, J., and Barmatz, M., *Phys. Rev. E,* **53**, 4490 (1996).

41. Barmatz, M., Hahn, I., and Zhong, F., *J. Low Temp. Phys.* **113**, 891 (1998); Barmatz, M., Hahn, I, and Zhong, F., *Proceedings of the 1999 NASA/JPL International Conference on Fundamental Physics in Space,* (to be published).

42. Agosta, C.C., Wang, S., Cohn, L.H., and Meyer, H., *J. Low Temp. Phys.* **67**, 237 (1987).

43. Zimmerli, G.A., Wilkinson, R.A., Ferrell, R.A., and Moldover, M.R., *Phys. Rev. Lett.* **26**, 5253 (1999); Zimmerli, G.A., Wilkinson, R.A., Ferrell, R.A., and Moldover, M.R., *Phys. Rev. E* **59**, 5862 (1999).

44. Barmatz, M., Zhong, F., and Hahn, I., *Proceedings of the 22nd International Conference on Low Temperature Physics* (1999), to be published in *Physica B.*

45. Zinn, S.-Y., Ph.D Thesis, University of Maryland (1997).

46. Guida, R. and Zinn-Justin, J., Nucl. Phys. B489[FS], 626 (1997).

47. Campostrini, M., Pelissetto A., Rossi, P., and Vicari, E., *Phys. Rev. E***60**, 3526 (1999).

48. Kiselev, S.B., and Sengers, J.V., *Int. J. Thermophys.* **14**, 1 (1993).

49. Levelt Sengers, J.M.H., Kamgar-Parsi, B., Balfour, F.W., and Sengers, J., *J. Phys. Chem. Ref. Data* **12**, 1 (1983).

50. Belyakov, M.Yu., and Kiselev, S.B., *Physica A*, **190**, 75 (1992).

51. Bagnuls, C., and Bervillier, C., *Phys. Rev. B* **32**, 7209 (1985).

52. Bruce, A.D., and Wallace, D. J., *J. Phys. A* **9**, 2208 (1976).

53. Nicoll, J.F. and Bhattacharjee, J.K., *Phys. Rev. B* **23**, 289 (1981); Nicoll, J.K., and Albright, P.C., *Phys. Rev. B* **31**, 4576 (1985).

54. Sengers, J.V., in *Supercritical Fluids: Fundamentals for Applications*, E. Kiran and J.M.H. Levelt Sengers (eds.), Kluwer, Dordrecht (1994), p. 231.

55. Anisimov, M.A., Luijten, E., Agayan, V.A., Sengers, J.V., and Binder, K., *Physics Lett. A*, **261**, 89 (1999).

56. Kostrowicka Wyczalkowska, A. and Sengers, J.V., *J. Chem. Phys*, **111**, 1551 (1999).

57. Kostrowicka Wyczalkowska, A., Abdulkadirova, Kh. S., Anisimov, M.A., and Sengers, J.V., *Proceedings of the 13th International Conference on the Properties of Water and Steam*, to be published.

58. Anisimov, M.A., Povodyrev, A.A., and Sengers, J.V., *Fluid Phase Equilibria*, **158-160**, 537 (1999).

59. Kierstead, H., *J. Low Temp. Phys.* **23**, 791 (1976).

60. Chan, M., Ryschkewitsch, M., and Meyer, H., *JLTP*, **26**, 211 (1977).

61. Gallegher, T.J., *Simple Dielectric Liquids, Mobility, Conduction, and Breakdown,* Oxford UP, London, p. 77 (1975).

62. Bruch, L.W., Cole, M.W., and Zaremba, E., *Physical Adsorption: Forces and Phenomena*, Clarendon Press, Oxford University Press, (1997).

6. APPENDICES

Appendix A. Equations-of-State

Asymptotic Parametric Scaled Equation-of-State

The asymptotic scaling form of the equation-of-state is simply and elegantly displayed in the parametric representation. This representation, which has been shown to be consistent with field-theoretical Renormalization Group results, expresses thermodynamic parameters and functions in terms of two variables. The first of these variables quantifies the "distance" of the system from the critical point. This quantity is directly related to the correlation length of the system. The second quantity is an "angular" variable that fixes the pressure and temperature (or cognate thermodynamic parameters) on the phase diagram. Calling the first parameter r and the second one θ, a set of relationships describes the order parameter, ψ, the reduced temperature, t, and the ordering field, h. In the case of the liquid-gas critical point, the order parameter is the difference between the system's density, ρ, and the density at the critical point, ρ_c. The "reduced temperature" is actually a combination of the reduced temperature and the reduced pressure that takes the system along the coexistence curve in the two-phase region and extrapolates to the critical isochore in the one-phase region. The ordering field is another linear combination of the reduced temperature and reduced pressure that takes the system away from the critical point in a different direction on the phase diagram. In the parametric representation, the following equations describe the quantities ψ, t, and h:

$$\psi = r^{\beta}\Psi(\theta) \tag{A1}$$

$$t = rT(\theta) \tag{A2}$$

$$h = r^{\beta\delta}l(\theta) \tag{A3}$$

The relations (A1) - (A3) replace the equation-of-state, in that the thermodynamics of the system are defined in terms of two independent variables, r and θ. The details of the equation-of-state are contained in the precise forms of the functions $\psi(\theta)$, $T(\theta)$, and $l(\theta)$. A variety of proposals exist. Among the simplest are the cubic models, for which

$$\Psi(\theta) = \Psi_0\theta\left(1 + c\theta^2\right) \tag{A4}$$

$$T(\theta) = T_0\left(1 - b^2\theta^2\right) \tag{A5}$$

$$l(\theta) = l_0\theta\left(1 - d_1\theta^2 + d_2\theta^4\right). \tag{A6}$$

When the coefficient c in Eq. (A4) is equal to zero, the model is called the linear model. Interestingly, the linear version of the parametric equation-of-state is consistent with the results of epsilon expansion calculations to order ε^3. To this order in the expansion parameter, $\varepsilon = 4 - d$, where d is the system's spatial dimensionality, the parameters in Eqs. (A4) - (A6) are explicitly determined. Thus, there is a Renormalization-Group-based prediction for the homogeneous equation-of-state of a system near its critical point. The results of measurements in the MISTE experiments will provide a test of this equation-of-state.

There are, in addition, a number of other versions of the parametric equation-of-state that can be compared with the data to be collected in the proposed MISTE experiments. It is hoped that this comparison will shed light on the exact form of the equation-of-state, and that one will be able to discriminate between the various candidates for the description of the relationships between thermodynamic parameters near the critical point of an $O(1)$ model.

The parametric equation-of-state can be easily connected to the general homogeneous dependence of thermodynamic quantities. For simplicity we will use the language of magnetic systems. The parametric formulas for the reduced temperature, t, the ordering field h and the order parameter, ψ, are

$$t = t_0 r T(\theta) \tag{A7}$$

$$h = h_0 r^{\beta\delta} l(\theta) \tag{A8}$$

$$\psi = m_0 r^{\beta} \Psi(\theta), \tag{A9}$$

where t_0, h_0 and m_0 are nonuniversal metrical factors determined from experiment. For this analysis, these metrical factors are set equal to 1 except where specified. Dividing Eq. (A8) by Eq. (A7) raised to the $\beta\delta$ power leads to the relationship

$$h/t^{\beta\delta} = l(\theta)/[T(\theta)]^{\beta\delta} \equiv W(\theta) \tag{A10}$$

Inverting this equation gives

$$\theta = W^{-1}(h/t^{\beta\delta}), \tag{A11}$$

which shows that the angular variable θ is a function of the combination $h/t^{\beta\delta}$. Substituting into Eq. (A9) gives

$$\psi = r^{\beta}\Psi\left(W^{-1}(h/t^{\beta\delta})\right) \equiv r^{\beta}\Phi(h/t^{\beta\delta}). \tag{A12}$$

Now, by dividing both sides of Eq. (A7) by $T(\theta)$ and using Eq. (A11), we again obtain an expression for r as a function of $h/t^{\beta\delta}$. By substituting this expression for r in Eq. (A12), one ends up with the equation

$$\psi = t^{\beta}\Omega(h/t^{\beta\delta}). \tag{A13}$$

In this way the singular part of any thermodynamic function that has the form $r^p G(\theta)$ can be rewritten in the generalized homogeneous form $t^p \Gamma(\theta)$. Thus, by plotting a measured thermodynamic function by its corresponding t^p throughout the critical region, one obtains a universal curve as a function of $h/t^{\beta\delta}$ that can be tested against any parametric equation-of-state prediction.

As a first step in the theoretical preparation for the investigation of the universal equation-of-state, we present here the predictions of four contenders for the asymptotic equation-of-state of a liquid-vapor system in the critical regime. We then compare the predictions from those equations for the specific heat and isothermal susceptibility along a noncritical isochore and a noncritical isotherm. All the equations-of-state take into account the most recent techniques for the calculation of critical-point thermodynamics, and all have been formulated with an eye to the reproduction of universal amplitude ratios. It is interesting, but not entirely surprising, that the predictions of these equations-of-state are more or less consistent with each other, at least in the instances that are considered here. There are small variations, and it is important to see whether or not experiments can distinguish between them. Additionally, it would be interesting to discover whether or not there are any experimental configurations that are more sensitive to the differences between the various equations-of-state.

The four equations-of-state are

1. The extended cubic model of Zinn and Fisher [45]
2. The extended sine model of Fisher and Zinn [7]
3. The field-theoretical equation-of-state of Guida and Zinn-Justin [46]
4. The high-temperature-series-based equation-of-state of Campostrini, et al. [47]

Noncritical paths

The conventional approach to the measurement of critical phenomena is to choose a path on the phase diagram that terminates on the critical point. The asymptotic behavior of a thermodynamic function is, then, a pure power law in the distance in parameter space from the critical point. It is possible to envision an experiment in which the path passes near to, rather than through, the critical point. Along such a path, the behavior of the susceptibility will be controlled by features of the equation-of-state that go beyond the power law limits associated with critical exponents. In this appendix we consider two noncritical paths: a noncritical isochore and a noncritical isotherm. The paths are illustrated as dashed lines in Fig. A1, which locates them on the phase diagram in the density-temperature plane. Figure A1 illustrates the two noncritical paths relevant to the plots below. The horizontal path shown as a dashed line is a noncritical isochore, along which the density of the system is fixed at a value not equal to the critical density. The vertical dashed line is a noncritical isotherm, along which the system's temperature is at a fixed value, different from the critical temperature.

The nonuniversal metrical factors, t_0, m_0 and h_0 in Eqs. (A7-A9) can be determined from experimental measurements of the isothermal susceptibility and the specific heat along the critical isochore, along with a determination of the isothermal susceptibility along the critical isotherm. The extraction of those quantities is made possible by the following two relationships, which hold along the critical isochore

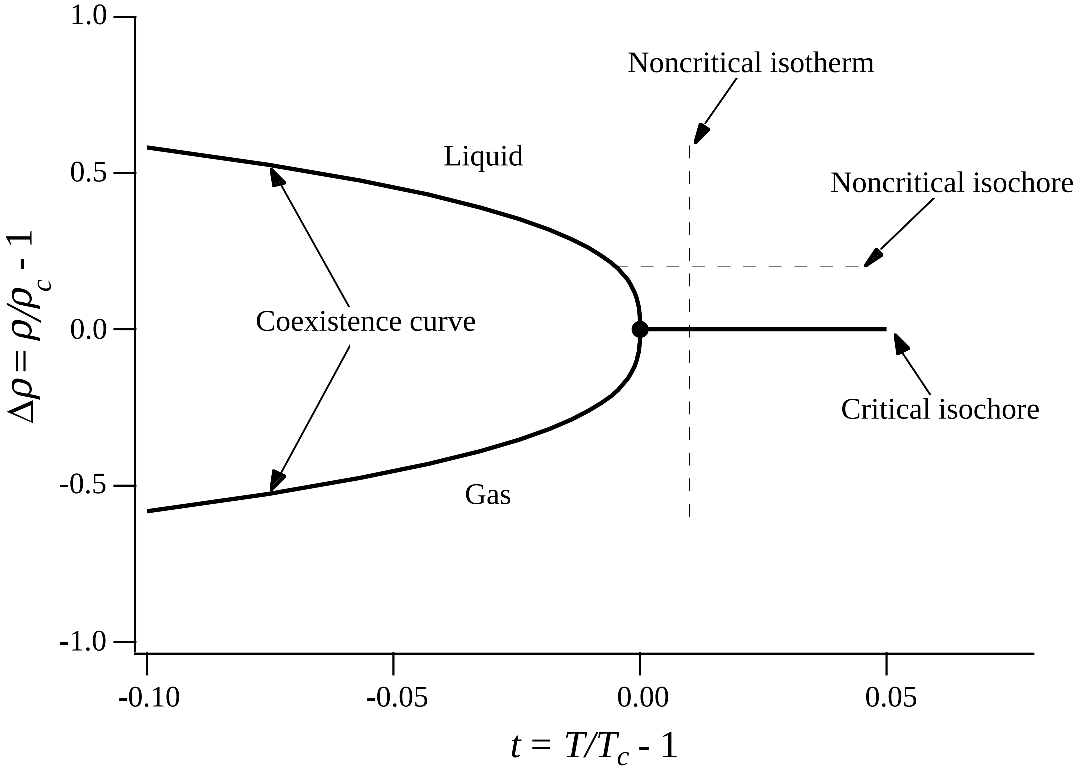

Fig. A1. Density-temperature phase diagram of a liquid-vapor system.

$$
\begin{aligned}
C_V^* &= \frac{h_0 m_0}{t_0^{2-\alpha}} t^{-\alpha} C_1(0) \\
&\equiv A_0^+ t^{-\alpha}
\end{aligned}
\qquad \text{(A14)}
$$

$$
\begin{aligned}
\chi_T^* &= \frac{m_0}{h_0} t_0^{\gamma} t^{-\gamma} X_1(0) \\
&\equiv \Gamma_0^+ t^{-\gamma}
\end{aligned}
$$

and the additional relationship, which holds on the critical isotherm

$$
\begin{aligned}
\chi_T^* &= \frac{m_0^{1+\frac{\gamma}{\beta}}}{h_0} \psi^{-\gamma/\beta} X_2(\theta_c) \\
&\equiv D\psi^{-\gamma/\beta}
\end{aligned}
\qquad \text{(A15)}
$$

In the above equations, the functions $C_1(\theta)$, $X_1(\theta)$, and $X_2(\theta)$ are universal within a particular equation-of-state and are readily derived from the parametric functions defined above. The value θ_c of the parametric angular variable places the system on the critical isotherm. With the use of Eqs. (A14) and (A15), the metrical factors can be expressed in terms of the asymptotic amplitudes A_0^+, Γ_0^+, and D. These amplitudes will be determined from the MISTE flight measurements in the asymptotic region. It is also anticipated that precision measurements performed in an earthbound setting outside the gravity-affected region will permit an initial exploration of the predictions of crossover equations-of-state.

Before proceeding with a discussion of the predictions of the various equations-of-state, we describe the way in which the curves for the susceptibility along a noncritical isochore are normalized so that they fall along the same asymptotes at both ends. The methods described here are straightforwardly extended to the case of the other curves plotted in this appendix. We start with the expression, Eq. (A14), for the susceptibility along the critical isochore. The actual version of the susceptibility that is plotted is that expression divided by the coefficient Γ_0^+. Now, the equation that governs the variation of the temperature along a curve in the phase diagram of the system along which the order parameter is a constant is

$$t = t_0 \left(\frac{\Psi}{m_0 m(\theta)} \right)^{1/\beta} k(\theta) . \tag{A16}$$

Let θ_k be the value that the angular variable takes on the coexistence line. Again, making use of the parametric expression, Eq. (A14), for the susceptibility, we end up with the following result for the magnitude of this quantity at the coexistence curve

$$\left(t_0 \left(\frac{\Psi}{m_0 m(\theta_k)} \right)^{1/\beta} \right)^{-\alpha} \frac{X_1(\theta_k)}{X_1(0)} . \tag{A17}$$

The values of the order parameter Ψ are adjusted for the various equations-of-state so that this quantity is equal in all cases. As is clear from Eqs. (A14) and (A15), in order to compare these theoretical curves to experiment, we must scale the horizontal and vertical axes using the experimentally determined metrical factors.

The Isothermal Susceptibility

We start with the isothermal susceptibility, χ_T. This thermodynamic response function corresponds to the compressibility in the case of the liquid-vapor system. First, we display the susceptibility, as predicted by the various models, along a noncritical isochore. Figure A2 displays a plot of the isothermal susceptibility in the liquid-vapor system for a noncritical isochore. The temperature is “reduced” with respect to the temperature at the coexistence curve, T_K. Shown in this graph are the predictions for this quantity of the four equations-of-state discussed in this appendix. The curves have been adjusted so that they lie on top of each other along the power-law tail to the right and the horizontal asymptote to the left. This adjustment allows the viewer to discern differences in the essential shapes of the curves. It is unlikely that experiments will distinguish between the four equations-of-state on the basis of a measurement of the quantity depicted here.

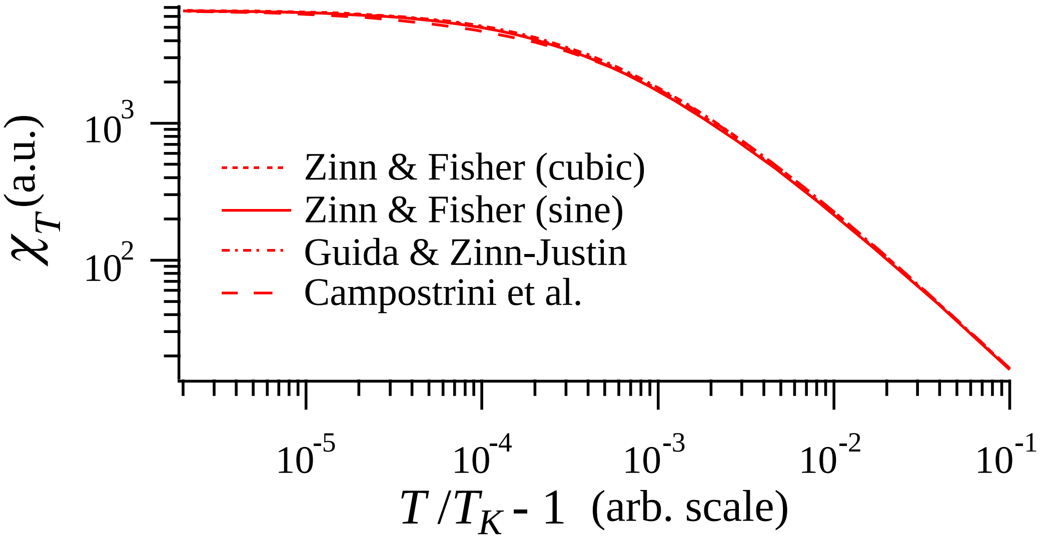

Fig. A2. Plot of the susceptibility along a noncritical isochore.

Figure A3 below displays plot of the susceptibility plotted along a noncritical isotherm. The density is "reduced" with respect to the critical density, $\rho_{c.}$. The graph shows the predictions of the four equations-of-state discussed in this appendix. As in the case of the plot along a noncritical isochore, the curve interpolates between a power law in the rightmost region and a horizontal asymptote at the far left. There is no clearly visible distinction between the four predicted curves.

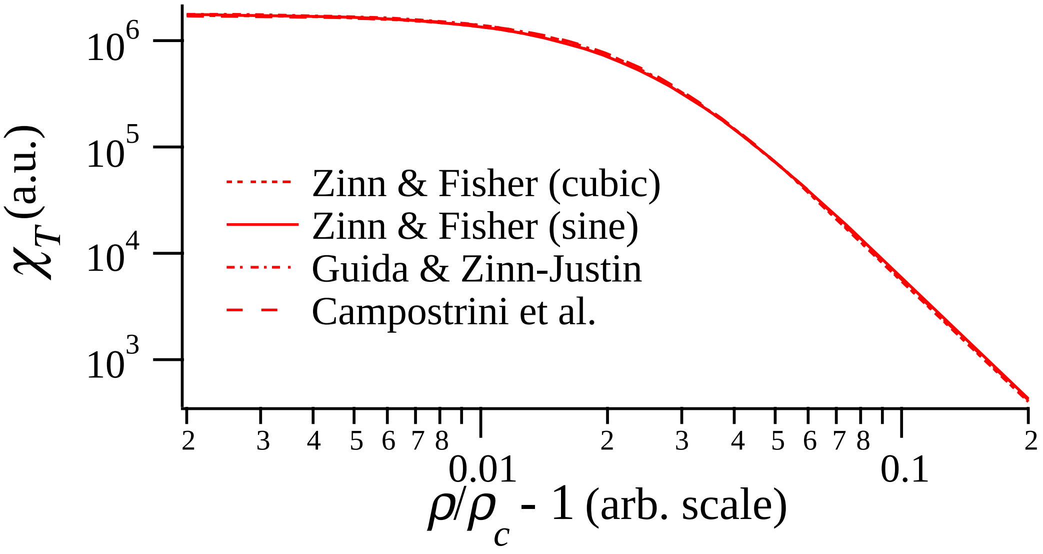

Fig. A3. Plot of the susceptibility along a noncritical isotherm.

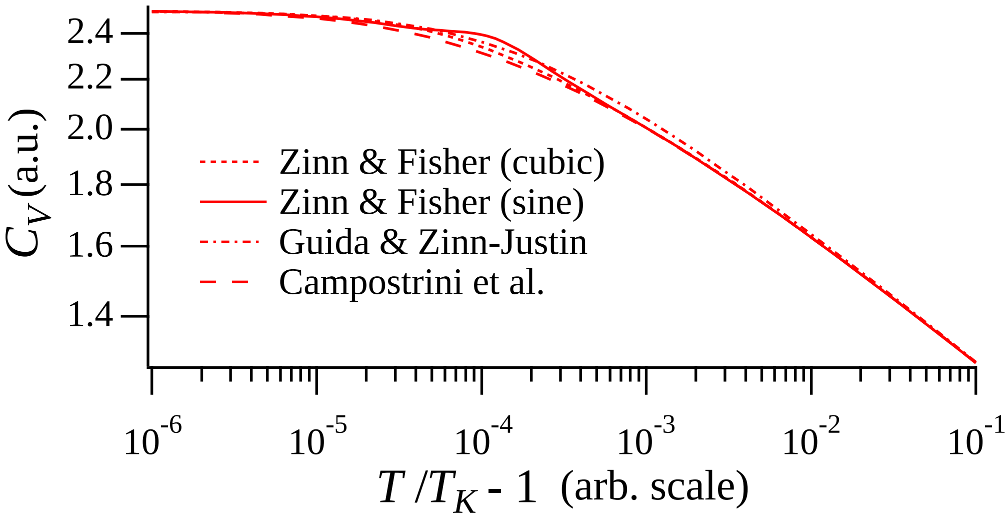

Fig. A4. Plot of the specific heat along a noncritical isochore.

The Specific Heat

Corresponding curves can be drawn for the specific heat. Figure A4 is a plot of the specific heat at constant density, equivalent to the specific heat at constant volume, for the liquid-vapor system, for a noncritical isochore. The temperature is “reduced” with respect to the temperature at the coexistence curve, T_K. The graph displays the predictions of the four equations-of-state discussed in this appendix. The curves have been adjusted as described for the previous figures. In this case, there is a visible distinction between what one equation-of-state predicts and the results that follow from the three others. The extended sine model of Fisher and Zinn [7] gives rise to a small, but distinctive, feature on the shoulder separating the power law and the horizontal asymptote. We have in this case a possibly experimentally significant divergence between one equation-of-state and the others in the group being compared. To what extent this ought to be taken seriously is not at all clear. We are now evaluating whether this feature can be determined experimentally.

The final set of curves, shown in Fig. A5, shows a plot for the specific heat at constant volume plotted along a noncritical isotherm. The density against which the specific heat is plotted is “reduced” with respect to the critical density, $\rho_{c.}$. The graph displays the predictions of the four equations-of-state discussed in this appendix. The curves have been adjusted as described earlier. Again, there is no clearly visible distinction between the four predicted curves.

In all the plots except the one shown in Fig. A4, we have a set of predictions that coincide to within differences that probably cannot be distinguished experimentally. It thus appears that the four recent universal equations-of-state surveyed here provide predicted behaviors for the specific heat at constant volume and the isothermal susceptibility along noncritical paths that are in near-perfect agreement. Experimental measurements will serve to test this consensus on the implications of the universal critical equation-of-state.

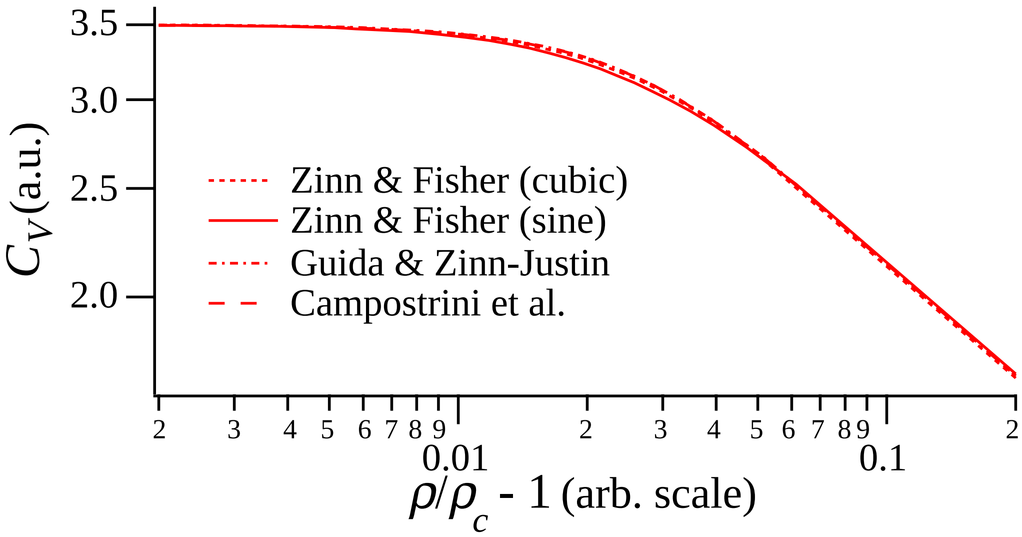

Fig. A5. Plot of the specific heat along a noncritical isotherm.

The MISTE experiment will also be able to probe the crossover from noncritical to critical behavior, both along paths ending at the critical point and along the noncritical paths discussed here. In this way, MISTE should be able to assess the way in which crossover to asymptotic critical behavior is manifested in the equation-of-state. There has been theoretical and experimental discussion of crossover in the equation-of-state in the vicinity of the critical point, and the connection of this behavior with the results of the Renormalization Group has been explored (see discussion in the next subsection). We are planning to extend the RG analysis and to adapt it to the ^{3}He system by taking into account currently available results, including crossover of the all-important four-point coupling constant. Additionally, an assessment is underway of the effects on the equation-of-state of the asymmetry of the liquid vapor system, as manifested in the rectilinear diameter of the coexistence curve. This effect is expected to be quite small in ^{3}He, as experimental evidence tells us that the coexistence curve of this system is remarkably symmetric. The outcome of the analysis will be expressions that will facilitate the extraction of crossover information from measurements of the type described above.

Nonasymptotic Equations-of-State

The asymptotic scaled equation-of-state cannot be used in practice because the range of its validity does not exceed $t \sim 10^{-4}$ and $\Delta\rho \sim \pm 0.05$ from the critical point. This estimate is based on the expected values of the first corrections to the asymptotic scaling for simple fluids (Γ_1^+/Γ_0^+ is of order unity) and on the expected accuracy in the measurement of the second derivatives of the free energy (about 1%). Hence, nonasymptotic corrections to scaling need to be introduced into the equation-of-state in order to compare results to ground-based experimental data.

In the first approximation one can consider only one correction term (the first Wegner correction). The first correction can be implemented into the linear parametric model by using two alternative forms of the thermodynamic potential. Kiselev and Sengers [48] formulated the linear model using density and temperature as independent variables, whereas Levelt Sengers et al. [49] used a field-dependent thermodynamic potential as a function of chemical potential and temperature. The asymptotic equation-of-state appears to be identical for these two formulations, whereas the correction amplitudes are different. As a result, the universal correction-amplitude ratios are not the same, both differing from the theoretical predictions (which themselves have considerable uncertainties).

Moreover, there are two other factors that contribute to the uncertainties of the nonasymptotic parametric equation-of-state. First, the nonasymptotic critical exponent Δ is not accurately known. Its predicted universal value varies from 0.50 to 0.54, depending on the method of calculation. Second, there is a correction to the asymptotic scaling associated with liquid-vapor asymmetry. In the lattice gas (Ising model), this correction is absent. The liquid-gas asymmetry can be taken into account through the so-called mixing of the field variables (temperature and chemical potential). This is a rigorous way for accounting for the asymmetry, but it requires an additional adjustable system-dependent parameter.

In principle, including higher-order terms in the Wegner expansion might help in extending the range of validity of the scaled equation-of-state. However, such a procedure involves additional adjustable parameters, which are difficult to control. The Wegner corrections drive properties of simple fluids to mean-field (classical, van der Waals-like) behavior, although the classical limit is never reached within the critical domain. The larger the correction amplitudes, the more pronounced a “crossover” to the classical behavior. As the convergence of the Wegner series is in doubt, a fit to the Wegner expansion is dangerous, and a closed-form crossover equation-of-state is needed to determine the values of the correction amplitudes and to describe the properties of fluids in an extended critical region.

Theoretical approaches to deal with the crossover problem have been considered by many investigators (see, e.g., a list of references in [15]). Most of these approaches are based on the RG theory of critical fluctuations. Although the exact solution of this problem for 3-dimensional Ising-like systems is still not available, the main physical features of crossover phenomena have been clarified. An explicit expression for the crossover susceptibility in zero field has been obtained by Belyakov, Yu, and Kiselev [50] in the first order of the ε-expansion. Bagnuls and Bervillier have obtained an alternative solution for the susceptibility from a field-theoretical approach [51]. These solutions did not yield the equation-of-state. Another solution of the crossover problem that does yield a scaled equation-of-state (i.e., it is not restricted to systems in zero field) can be obtained as an approximation to a more general approach based on a so-called match-point method of the Renormalization Group theory [52] as developed by Nicoll and co-workers [53] and further implemented by Sengers and co-workers [54].

The phenomenological equation-of-state developed from the Nicoll theory was called the “crossover Landau model” because it was based on the classical Landau expansion renormalized by fluctuations. A comparison between these three alternative solutions has been made by Anisimov et al. [15]. It has been shown that in the infinite cutoff approximation, which neglects the discrete microscopic structure of fluids, all approaches mentioned above give the same crossover behavior of the susceptibility in zero field. In this approximation the crossover between Ising-like asymptotic critical behavior and mean-field (classical) behavior is controlled by a single parameter, the crossover scale, also called the "Ginzburg number." The correction-to-scaling amplitudes, as well as the fluctuation corrections to mean-field behavior, can be calculated through the Ginzburg number. However, if cutoff effects are included, the crossover equation-of-state contains two crossover parameters; namely, a scaled coupling constant and the cutoff wave number.

Recently, the two-parameter crossover Landau model has been successfully applied to describe the crossover susceptibility obtained by computer simulation of the 3-dimensional Ising model with a variety of interaction ranges [55]. The crossover Landau model of the scaled equation-of-state has been applied to many fluids and fluid mixtures [54,56] and to light and heavy water in the critical region [57]. It has also been shown that cutoff effects play a crucial role in understanding the crossover phenomena in complex fluids [58].

Although the crossover Landau model of the scaled equation-of-state represents the current, experimental and simulation data within their accuracy, it yields values of the asymptotic amplitude ratios that do not perfectly match the most accurate Ising values. The discrepancy is 4% for the A_0^+/A_0^- ratio and about 10% for $A_0^+\Gamma_0^+/B_0^2$, which is significantly larger than the accuracy of the theoretical values (about 2% for both ratios). The crossover scaled equation-of-state needs to be improved to satisfy the theoretical amplitude ratios. A possible step in this direction would be the formulation of the crossover equation-of-state in a parametric form. Work towards developing such a parametric crossover equation-of-state is currently in progress.

Accurate experimental data of the properties of ^{3}He in the extended critical region become crucial for testing alternative approaches to the crossover problem in general and to a crossover scaled equation-of-state in particular. Accurate experimental data within the extended critical region ($|t| < 10^{-2}$ and $\Delta\rho \leq \pm\ 0.1 - 0.2$ from the critical point) should be used to test different versions of the nonasymptotic scaled equation-of-state. The MISTE flight experiment will provide experimental measurements in the asymptotic region that can be used to more accurately determine the leading critical amplitudes. These new measurements coupled with ground-based crossover data will permit a stringent test of equation-of-state models.

Appendix B. Analysis of Susceptibility Measurements

In this appendix we discuss in detail the proposed techniques to measure the susceptibility along the critical isochore and critical isotherm. These techniques will also be valid along other isochores and isotherms. In the following discussion, we define $\Delta P = P/P_c - 1$. We also scale variables with corresponding critical parameters and denote them with asterisks. In many of the following analyses, we extensively use the restricted cubic model given by:

$$t = r\left(1 - b^2\theta^2\right), \tag{B1}$$

$$\Delta\rho = r^{\beta} k\theta\left(1 + c\theta^2\right), \tag{B2}$$

$$\Delta\mu = \mu\left(\rho, T\right) - \mu\left(\rho_c, T\right) = \frac{\rho_c}{P_c}\Delta\mu^* = \frac{\rho_c}{P_c} r^{\beta\delta} a\theta\left(1 - \theta^2\right), \tag{B3}$$

$$\chi_T = \frac{\rho_c^2}{P_c}\chi_T^* = \frac{\rho_c^2}{P_c}\frac{k}{a} r^{-\gamma} = \frac{\rho_c^2}{P_c}\frac{k}{a}\left(\frac{t}{1 - b^2\theta^2}\right)^{-\gamma}, \tag{B4}$$

where the effective critical exponents and fluid-dependent fitting parameters, *a* and *k*, are given in reference [27].

Conventional Technique

In the conventional technique, one measures the changes in density and pressure directly along an isotherm, and then deduces the susceptibility as $\chi_T = \rho\left(\partial\rho/\partial P\right)_T$. The dependence of reduced *P* and χ_T on the reduced density for ^{3}He is illustrated in Fig. B1 for $t = 1\times10^{-4}$.

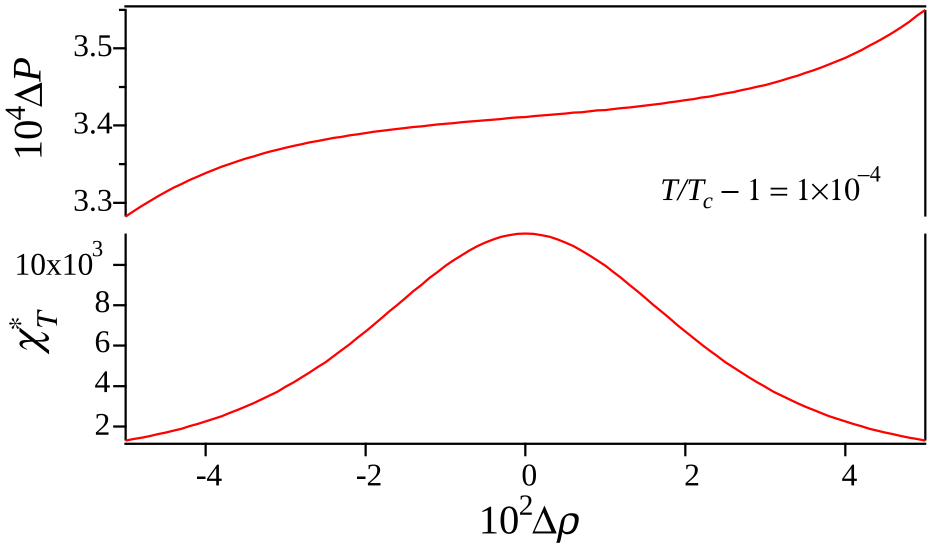

Fig. B1. Reduced pressure and susceptibility versus reduced density for ^{3}He at $t = 1\times10^{-4}$. The ΔP versus $\Delta\rho$ curve was derived using the restricted cubic model [27].

The uncertainty in the measured isothermal compressibility is determined from

$$\delta\chi_T = \sqrt{\left(\frac{\partial\chi_T}{\partial P}\delta P\right)^2 + \left(\frac{\partial\chi_T}{\partial\rho}\delta\rho\right)^2 + \left(\frac{\partial^2\chi_T}{\partial P^2}(\delta P)^2\right)^2 + \left(\frac{\partial^2\chi_T}{\partial\rho^2}(\delta\rho)^2\right)^2 + \left(\frac{\partial^2\chi_T}{\partial P\partial\rho}\delta P\,\delta\rho\right)^2}\,. \quad \text{(B5)}$$

Along the critical isochore, the first derivatives $\left(\partial\chi_T/\partial P\right)_\rho$ and $\left(\partial\chi_T/\partial\rho\right)_P$ equal zero since χ_T peaks at $\Delta\rho = 0$. The second derivatives in Eq. (B5) can be calculated for any given reduced temperature along the critical isochore using the restricted cubic model,

$$\frac{\partial^2\chi_T^*}{\partial P^{*2}} = -\frac{2b^2k\,\gamma\,t^{-\gamma-2\beta\delta}}{a^3}, \quad \text{(B6)}$$

$$\frac{\partial^2\chi_T^*}{\partial\rho^{*2}} = -\frac{2b^2\,\gamma\,t^{-\gamma-2\beta}}{ak}, \quad \text{(B7)}$$

$$\frac{\partial^2\chi_T^*}{\partial P^*\partial\rho^*} = -\frac{2b^2\,\gamma\,t^{-\gamma-2+\alpha}}{a^2}. \quad \text{(B8)}$$

The relative uncertainty in χ_T along a near-critical isochore is given by

$$\left(\frac{\delta\chi_T}{\chi_T}\right)_\rho = \frac{2b^2\,\gamma\,t^{-2\beta\delta}}{a^2}\left(\delta P^*\right)^2 = 0.18\,t^{-3.09}\left(\delta P^*\right)^2, \quad \text{(B9)}$$

$$\left(\frac{\delta\chi_T}{\chi_T}\right)_P = \frac{2b^2\,\gamma\,t^{-2\beta}}{k^2}\left(\delta\rho^*\right)^2 = 4.4\,t^{-0.71}\left(\delta\rho^*\right)^2. \quad \text{(B10)}$$

Equations (B9) and (B10) can be used to determine the experimental resolutions of pressure δP^* and density $\delta\rho^*$ required to obtain a given uncertainty $\delta\chi_T/\chi_T$. Figure B2 shows the pressure and density resolutions as a function of reduced temperature for $\delta\chi_T/\chi_T = 1\%$.

Using a Straty-Adams type capacitance pressure gauge [33], we find that the pressure resolution is related to a capacitance resolution by

$$\frac{\delta P}{P} = \left(\frac{P_{\max}}{P} - 1\right)\frac{\delta C}{C}, \quad \text{(B11)}$$

where $P_{\max}$ is the pressure when the capacitor gap decreases to zero. In practice, an AC capacitance bridge can achieve a capacitance resolution of $\delta C/C \sim 4\times10^{-8}$, and a ratio $P_{\max}/P \sim 3$ is also achievable. Thus, we can attain a pressure sensitivity $\delta P/P \sim 8\times10^{-8}$.[1] It can be seen from Fig. B2 that this limits the experimental range to $t > 6\times10^{-5}$ using the conventional technique.

The experimental density resolution $\delta\rho/\rho$, required to obtain a given uncertainty $\delta\chi_T/\chi_T$ along the critical isochore, can be determined using Eq. (B10). The dashed curve in Fig. B2 shows the

---

[1] Our current Straty-Adams type capacitance pressure gauge has $P_{\max}/P \sim 11$, resulting in a pressure resolution of $\delta P/P \sim 4\times10^{-7}$.

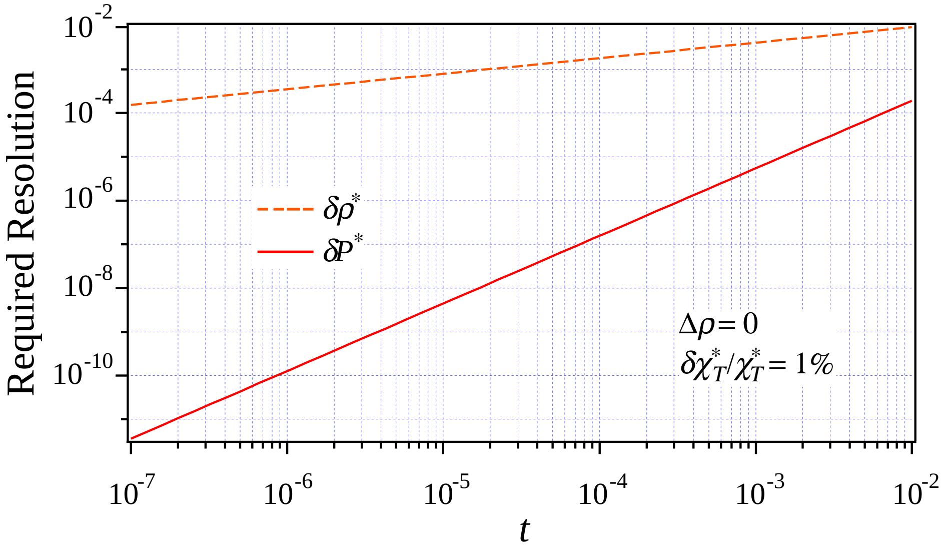

Fig. B2. Required resolution in pressure and density measurements as a function of reduced temperature in order to achieve $\delta\chi_T/\chi_T$ = 1% along the critical isochore.

density resolution as a function of reduced temperature again for the case of $\delta\chi_T/\chi_T$ = 1%. The Clausius-Mossotti equation,

$$\frac{\varepsilon - 1}{\varepsilon + 2} = \frac{4\pi}{3}\alpha\,\rho = \zeta\,, \tag{B12}$$

will be used to deduce a density from a measured capacitance. Kierstead [59] gave the expression for the ^{3}He polarizability as

$$\alpha = 0.123413 - 0.007166\,\rho\,. \tag{B13}$$

The critical density of ^{3}He is $\rho_c = 0.01374$ mole/cm^3. Therefore, in ^{3}He at $\rho = \rho_c$, $\alpha = 0.12331$ cm^3/mole, $\zeta_c = 0.007097$, and $\varepsilon_c = 1.02144$. The density will be changed by less than 30% about the critical density in the planned MISTE experiments. As a result, the ^{3}He polarizability will vary about 0.02%, and a systematic error in derived density will be less than 0.02% if $\alpha = 0.12331$ cm^3/mole is used throughout. In ground-based studies, we have achieved $\delta C/C \sim 7\times10^{-8}$ with an excitation voltage of 15 V, excitation frequency of 2.7 kHz, and time constant of 0.3 s. This leads to a density resolution of $\delta\rho^* = 3\times10^{-6}$ that will be quite sufficient for the conventional technique in its applicable range.

Electrostriction Technique

We have been evaluating an electrostriction technique for performing susceptibility measurements very near to the transition. This technique indirectly measures the pressure gradient from the expression

$$\nabla P = \frac{\varepsilon_0 \rho}{2}\nabla\left(E^2\frac{\partial\varepsilon}{\partial\rho}\right). \tag{B14}$$

Under an isothermal condition, we have

$$\mu(\rho_2,T)-\mu(\rho_1,T)=\int_{\rho_1}^{\rho_2}\frac{dP}{\rho}=\frac{\varepsilon_0}{2}E^2\frac{d\varepsilon}{d\rho}, \tag{B15}$$

which links the chemical potential gradient to the electrical field gradient. When a DC or equivalent rms AC voltage is applied across a capacitor gap, the ^{3}He fluid density increases in the gap. With the pressure gradient in Eq. (B14) written in terms of the density gradient via the susceptibility, we have a formula that links the density change and the inducing electric field within the capacitor gap:

$$\int_{\rho_1}^{\rho_2}\frac{d\rho}{\chi_T}=\frac{\varepsilon_0(\varepsilon-1)(\varepsilon+2)}{6\rho_2}E^2=\zeta_c\frac{\varepsilon_0(\varepsilon+2)^2}{6\rho_c}E^2=\frac{3\zeta_c\varepsilon_0}{2\rho_c(1-\zeta_c\rho_2^*)^2}E^2. \tag{B16}$$

Here ρ_1 is the fluid density outside the capacitor gap. When $E \neq 0$, the change in ρ_1 is negligible since the volume within the capacitor gap is much smaller than the cell volume. The fluid dielectric constant ε on the right-hand side of the equation is linked to the fluid density inside the capacitor gap ρ_2 via the Clausius-Mossotti equation. When the density change $\delta\rho = \rho_2 - \rho_1$ is small, χ_T can be taken as a constant, and one obtains

$$\chi_T=\frac{6\rho\delta\rho}{\varepsilon_0(\varepsilon-1)(\varepsilon+2)E^2}=\frac{6\rho_c\delta\rho}{\zeta_c\varepsilon_0(\varepsilon+2)^2E^2}=\frac{2\rho_c^2(1-\zeta_c\rho_2^*)^2}{3\zeta_c\varepsilon_0}\frac{\delta\rho^*}{E^2}. \tag{B17}$$

Therefore, the application of the electrostrictive technique for measuring χ_T requires an accurate experimental measurement of the ratio of density change over the square of the inducing electric field.

Critical Isochore

For a parallel plate capacitor with a gap d, the electric field in the gap is $E = V/d$ with V being the applied voltage across the gap. Since χ_T diverges strongly as T_c is approached, the required voltage across the capacitor gap will decrease if one requires the induced density change to remain a constant (see Fig. B3a.). At $t = 6\times10^{-7}$, this required voltage is ~ 0.8 V for a capacitor gap of $d = 5\times10^{-3}$ cm and $\delta\rho^* = 5\times10^{-4}$; a 1% resolution in χ_T at this reduced temperature translates into a required voltage resolution of 8 mV, which is easily achievable.

An AC bridge circuit is used to measure capacitance. Since the density change is proportional to V^2, the rms AC excitation voltage across the capacitor will have the same effect as an external DC voltage. Model calculations (see Fig. 7) show that at $t = 1\times10^{-6}$, the measured susceptibility will have less than 1% systematic error from its value along the critical isochore if the measurement is taken in a sample with $\Delta\bar{\rho} < 5\times10^{-4}$. From Fig. B3a, we see that for a density change of $\Delta\rho = 5\times10^{-4}$, a capacitance resolution of $\delta C/C = 1\times10^{-7}$ must to be achieved with an AC excitation voltage across the capacitor of $\leq$ 1V at $t = 1\times10^{-6}$.

Chan et al. [60] used two identical capacitors to form an AC capacitance bridge with an excitation voltage of 16 V rms (8 V rms across the detecting capacitor), and they achieved a resolution of about $\delta C/C = 3\times10^{-9}$ with a lock-in time constant of 4s. Since $\delta C/C$ is linearly proportional to the excitation voltage, a reduction in the excitation voltage from V_{exc} = 16 V to 1.6

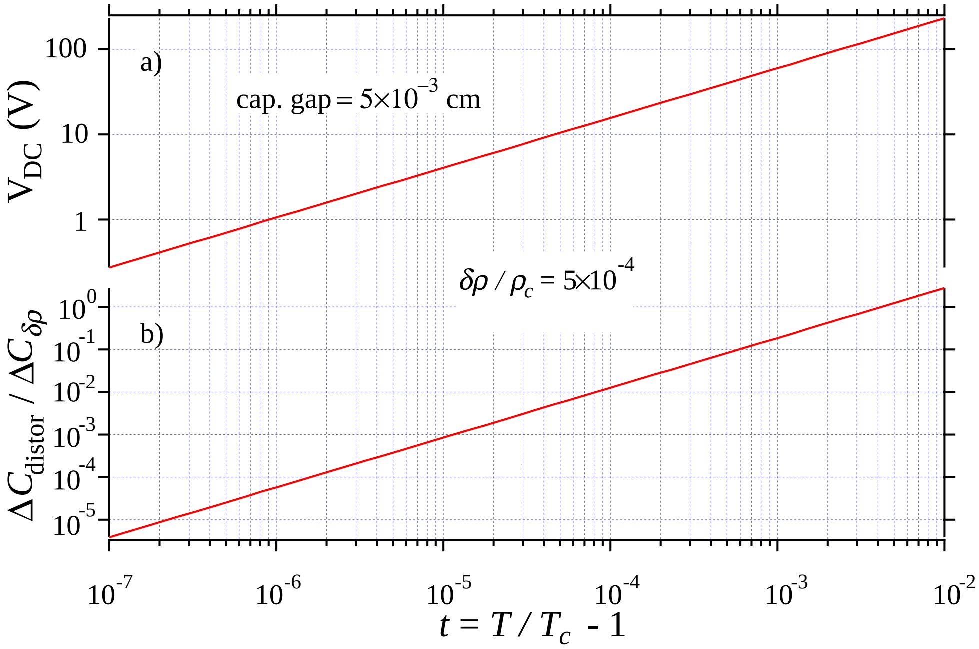

Fig. B3. a) Required voltage for inducing $\delta\rho/\rho_c = 5\times10^{-4}$ versus reduced temperature. The calculation is made along the critical isochore. b) The ratio of calculated capacitance deformation due to electrical force over true electrostriction effect versus *t*.

V (0.8 V rms across the detecting capacitor), leads to a factor of 10 resolution reduction from $\delta C/C = 3\times10^{-9}$ to 3×10^{-8}. Our analysis shows that a resolution of $\delta C/C = 5\times10^{-8}$, with V_{exc} = 1V rms across the capacitor and a signal-to-noise ratio of 1, can be achieved using a 1s time constant by making several changes in the ground-based AC capacitance bridge system.

As *t* increases, the susceptibility χ_T decreases. At $t = 1\times10^{-2}$, the required electric field *E* for inducing $\delta\rho^* = 5\times10^{-4}$ is $E = 3.6\times10^6$ V/m (V = 181 V in Fig. B3a), which is about 10 times smaller than that needed for the dielectric break down of fluid ^{3}He [61]. On the other hand, the mechanical deformation of the capacitor gap by the high electric field will introduce uncertainty in the density measurement. The attractive electric force decreases the effective capacitor gap and therefore increases the measured capacitance in addition to that caused by the electrostriction in the fluid.

The deformation of a capacitor plate is proportional to R^4/δ^3, where *R* is the radius and δ is the thickness of the plate. The calculation in Fig. B3b uses the geometry of the currently employed capacitor (R = 0.5 cm, δ = 0.0028 cm); it shows that capacitance change due to the gap distortion equals the capacitance change due to the electrostriction at $t = 4\times10^{-3}$. A reduction in *R* and/or an increase in δ can reduce the deformation. However, the minimum radius of the capacitor plate is set by the requirement of a good signal-to-noise ratio. The maximum thickness of the plate is set by the sample cell gap, since one plate has to be emerged completely in the ^{3}He fluid in order to avoid any pressure effect. For the MISTE ground-based studies, the cell height is h = 0.05 cm, which limits the capacitor plate thickness to δ = 0.0028 cm. For the flight experiment, the capacitor plate suspended in the sample will be made of 0.2 cm thick sapphire. The gap distortion will be negligible. Since the DC power requirement is 200 V in the LTMPF design, this defines the upper limit for the electrostriction technique at $t = 1\times10^{-2}$ for a gap of 50 μm.

Since the conventional technique is adequate for $t > 6\times10^{-5}$ and the electrostriction technique is adequate for $t < 1\times10^{-2}$, we can use the conventional technique to calibrate the electrostriction technique over the range where the two overlap. The capacitor gap used to calculate the electric field is either 50 or 150 μm. It would be difficult to measure such a small gap with an accuracy of 1%. However, this uncertainty in the capacitor gap can be reduced through calibration, and the gap should change very little at smaller reduced temperature.

Very close to the critical temperature, χ_T becomes a strong function of the density. When the density change inside the capacitor gap is not small, χ_T cannot be taken as a constant out of the integral in Eq. (B16). Since the integration in Eq. (B16) is the chemical potential difference between the fluids within and outside the capacitor gap, we can solve θ_2 numerically for a given t and E from

$$E^2 = \frac{2P_c}{3\varepsilon_0\zeta_c}\left[\Delta\mu^*(r_2,\theta_2) - \Delta\mu^*(r_1,\theta_1)\right]\left[1-\zeta_c\rho^*(r_2,\theta_2)\right]^2. \qquad \text{(B18)}$$

Here $\Delta\mu^*$ is given by Eq. (B3), r is derived from Eq. (B1), and $\rho^* = 1 + \Delta\rho$ is from Eq. (B2). Once E and ρ_2 are known, we have $\delta\rho = \rho_2 - \rho_1$ and can evaluate an effective susceptibility using Eq. (B17) and compare it with the one for $E = 0$. The results for two reduced temperatures and $\rho_1 = \rho_c$ are shown in Figs. B4 and B5.

Let us take the rms excitation voltage across the detecting capacitor to be 0.500 V, which is close to the lower experimental limit. For $t = 1\times10^{-6}$, the ^{3}He fluid is already compressed by $\delta\rho_0^* = 2.24\times10^{-4}$ from ρ_c by this rms excitation voltage even before a DC bias is applied. An applied $V_{dc} = 0.47$ V will be required to produce a 1% density change ($\delta\rho^* = 2\times10^{-4}$) assuming a density resolution $\delta\rho^* = 2\times10^{-6}$. The total change from the ambient density is equal to the one induced by an equivalent rms $V = 0.69$ V.

The theoretical model developed above is being used to analyze the electrostriction technique data. The experimental procedure for measuring the density versus applied voltage squared is as follows: 1) accurately determine the rms V_{exc} across the detecting capacitor; 2) measure ρ before applying an additional DC voltage; 3) measure a series of $\delta\rho_{\text{meas}}(V_{dc} \neq 0)$. We choose to fit $\delta\rho_{\text{meas}}(V_{dc} \neq 0)$ versus $V_{\text{tot}}^2 = V_{exc,rms}^2 + V_{dc}^2$ with a polynomial,

$$\delta\rho_{\text{meas fit}} = A_0 + A_1 V_{\text{tot}}^2 + A_2 V_{\text{tot}}^4 + A_3 V_{\text{tot}}^6 + \cdots. \qquad \text{(B19)}$$

Here A_0 has a negative value that corresponds to the density change due to the pre-compression by the rms V_{exc}. By definition,

$$A_1 = \lim_{V_{\text{tot}}\to 0} \frac{\delta\rho_{\text{tot}}}{V_{\text{tot}}^2} = \lim_{V_{\text{tot}}\to 0} \frac{\delta\rho_{\text{meas}}(V_{dc} \neq 0) + |A_0|}{V_{exc,rms}^2 + V_{dc}^2} \propto \chi_T(\rho_1). \qquad \text{(B20)}$$

Thus, by deriving A_1 we can determined χ_T at the ambient density ρ_1 using Eq. (B17).

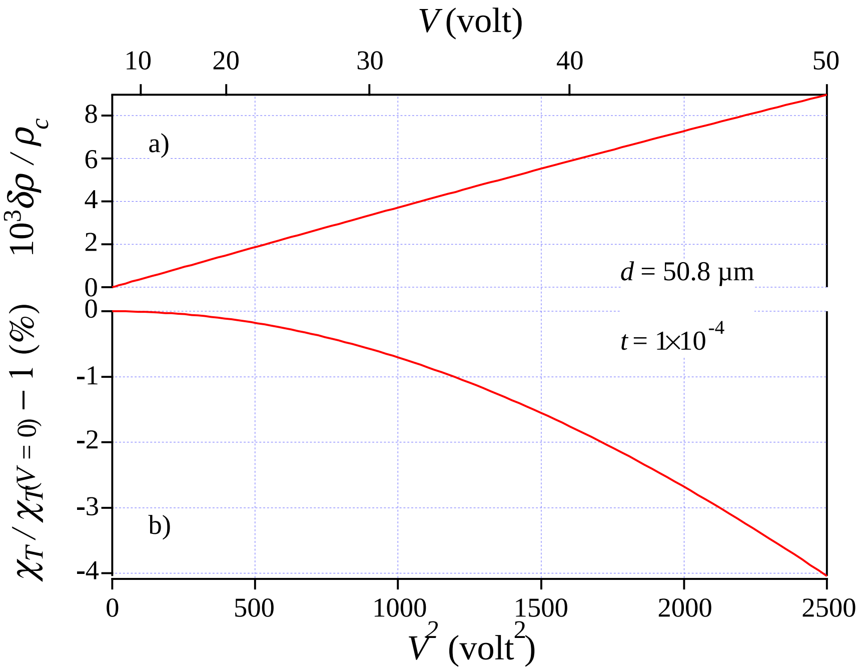

Fig. B4. a) Density change versus applied rms voltage in a capacitor of 50.8 µm gap size, b) Difference in percentage between effective χ_T ($E \neq 0$) and true χ_T ($E = 0$). The calculation is for $t = 1\times10^{-4}$.

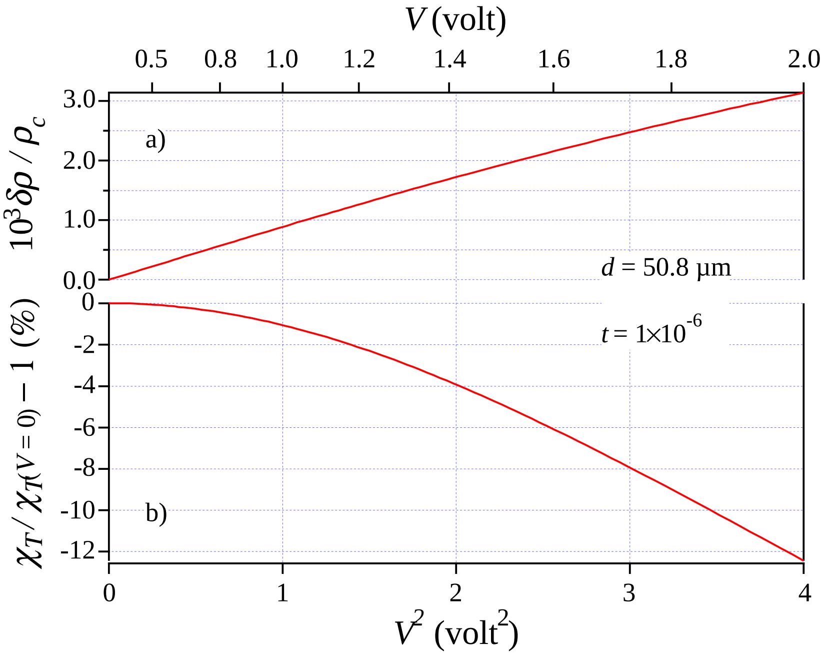

Fig. B5. a) Density change versus applied rms voltage in a capacitor of 50.8 µm gap size, b) Difference in percentage between effective χ_T ($E \neq 0$) and true χ_T ($E = 0$). The calculation is for $t = 1\times10^{-6}$.

Critical Isotherm

The electrostriction technique can also be used to measure the susceptibility along the critical isotherm. Along the critical isotherm the changes in pressure and density are related by the expression

$$\Delta P = D\Delta\rho\left|\Delta\rho\right|^{\delta-1}. \tag{B21}$$

Taking into account the most important correction to scaling term, the relationship above becomes

$$\Delta\rho = (\Delta P)^{1/\delta} A\left(1 + B\Delta P^{\zeta}\right), \tag{B22}$$

where $A = D^{1/\delta}$ and B are nonuniversal amplitudes and

$$\zeta = \frac{2\omega}{d + 2 - \eta} \approx 0.3218. \tag{B23}$$

Here $\omega \sim 0.5/\nu$ with ν and η being critical exponents and d = 3 being the system dimension. The expression for the derivative of the density with respect to pressure derived from Eq. (B22) is

$$\left(\frac{\partial\rho}{\partial P}\right)_T = \frac{A}{\delta}(\Delta P)^{-\frac{\delta-1}{\delta}}\left[1 + B(1 + \delta\zeta)\Delta P^{\zeta}\right]. \tag{B24}$$

By multiplying Eq. (B24) by (1 + $\Delta\rho$), one can obtain the susceptibility. However, the multiplication of (1 + $\Delta\rho$) distorts the single power law divergence of the susceptibility since $\Delta\rho$ will vary by up to 20% in the range where the critical isotherm is planned to be measured. As a first order approximation, we write

$$\chi_T^* = \frac{A}{\delta}(\Delta P)^{-\frac{\delta-1}{\delta}}\left[1 + B(1 + \delta\zeta)\Delta P^{\zeta}\right]. \tag{B25}$$

To carry out a theoretical calculation along the critical isotherm, we neglect the correction to scaling term and continue to use the restricted cubic model, in which $\theta = \Delta\rho/|\Delta\rho|/b$ from Eq. (B1). Using Eqs. (B2) and (B4), we have

$$\chi_T = \frac{\rho_c^2}{P_c}\frac{k}{a}r^{-\gamma} = \frac{\rho_c^2}{P_c}\frac{k}{a}\left(\frac{\Delta\rho}{k\theta(1 + c\theta^2)}\right)^{-\gamma/\beta} = \frac{\rho_c^2}{P_c}\frac{k^\delta}{a}\left(\frac{b^2 + c}{b^3}\right)^{\delta-1}\left|\Delta\rho\right|^{-(\delta-1)}. \tag{B26}$$

Here we use $\delta = \gamma/\beta + 1$. Therefore, by using the electrostriction technique to measure χ_T versus $\Delta\rho$ along the critical isotherm, we can obtain the leading nonuniversal amplitude and an exponent with its value equal to $\delta - 1$. Combining Eqs. (B17) and (B26), we have a relation between the applied electrical field E and induced density change $\delta\rho^*$ for a given reduced density $\Delta\rho$:

$$E^2 = \frac{2P_c}{3\zeta_c\varepsilon_0}\frac{a}{k^\delta}\left(\frac{b^3}{b^2 + c}\right)^{\delta-1}\left|\Delta\rho\right|^{(\delta-1)}\left[1 - \zeta_c(1 + \Delta\rho + \delta\rho^*)\right]^2\delta\rho^*. \tag{B27}$$

In Fig. B6 we show the required DC bias as a function of reduced density $\Delta\rho$ for an induced density change of $\delta\rho^* = 5\times10^{-4}$. Assuming an experimental voltage range of 1 – 200 V, the electrostriction method will be viable over the range of $7\times10^{-3} < \Delta\rho < 0.15$.

We should be able to perform measurements along the critical isotherm over the range $|\Delta\rho| > 7\times10^{-3}$ assuming the MISTE goal of determining the critical temperature T_c with an uncertainty of $\Delta T/T_c \approx 3\times10^{-7}$ (see Fig. 25). Figure B7 shows the calculated density change in the capacitor, using Eq. (B18), as a function of the total applied rms voltage for $t = 3\times10^{-7}$ and ambient density $\Delta\rho_1 = 1\times10^{-2}$. This analysis shows that a DC bias voltage ~ 0.8V is required to measure the susceptibility to ~ 1% for the MISTE goals along the critical isotherm. This can be achieved using a modified version of the existing ground-based capacitance bridge.

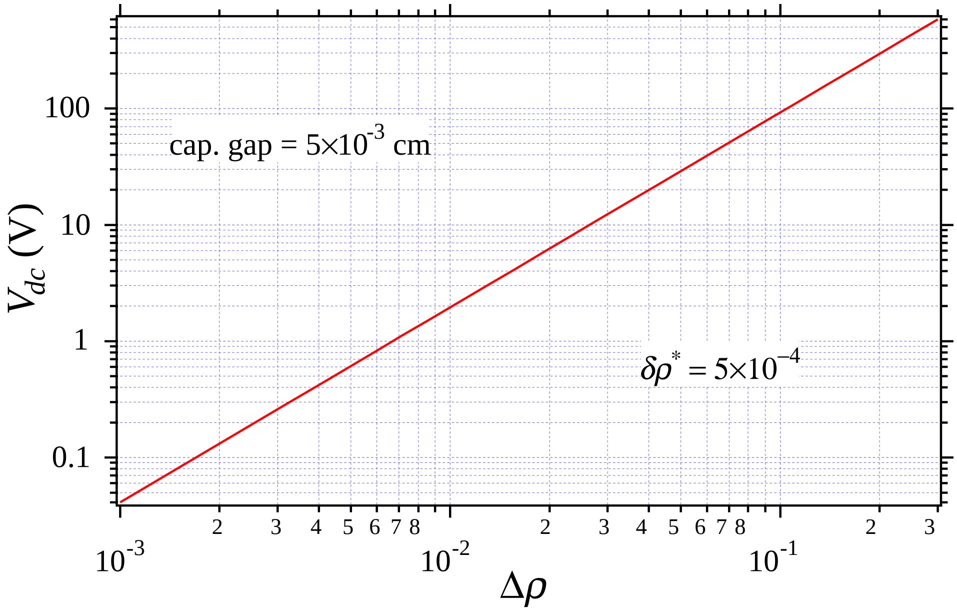

Fig. B6. Required voltage for inducing $\delta\rho^* = 5\times10^{-4}$ versus reduced density. The calculation is made along the critical isotherm using Eq. (B26).

Isotherm Measurements by Electrostriction

Figures B4, B5, and B7 essentially show the measurements of three isotherms at different temperatures with ambient density $\rho_1 = \rho_c$. These measurements require an extrapolation to zero voltage in order to obtain $\chi_T(\rho_c)$. Since the flight cell will be filled at the critical density before the launch to the space station, the initial electrostriction measurements will be performed with $\rho_1 = \rho_c$. We plan to also perform electrostriction measurements with the ambient density of the cell slightly below ρ_c. Under this condition, an isotherm curve of the measured $\Delta\rho_2$ versus V^2 will include an inflection point that is associated with ρ_c. Thus, we can determine $\chi_T(\rho_c)$ very close to T_c with much higher accuracy from these electrostriction measurements. Figure B8 shows the prediction for such measurements along the critical isotherm and $t = 5\times10^{-6}$.

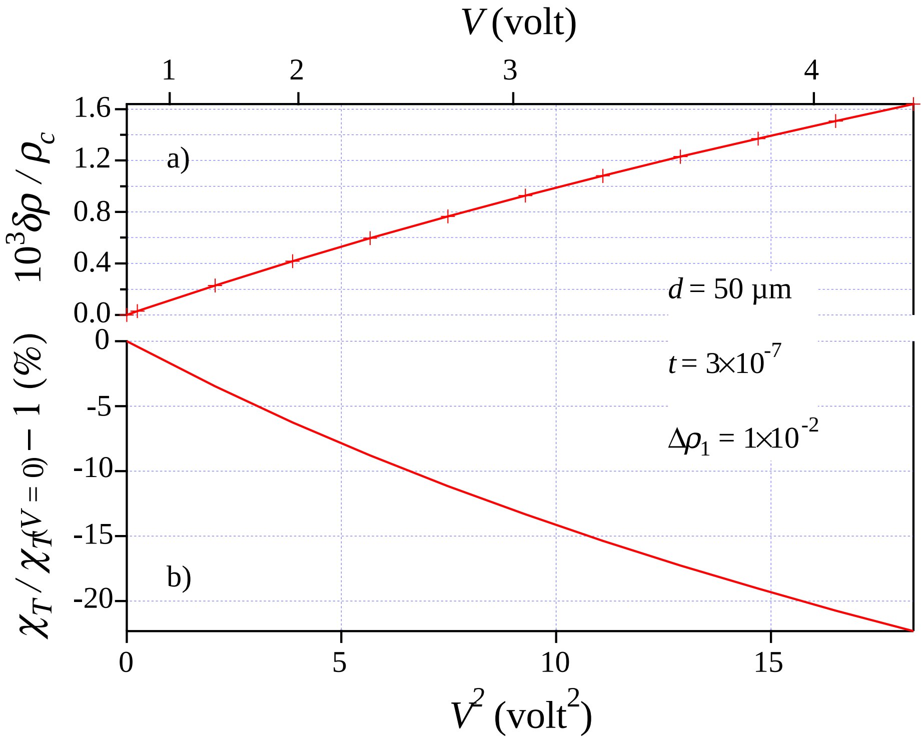

Fig. B7. a) Density change versus applied rms voltage in a capacitor with a 50 µm gap, b) Difference in percentage between effective χ_T ($E \neq 0$) and true χ_T ($E = 0$). The calculation is made for $t = 3\times10^{-7}$ and ambient density $\Delta\rho_1 = 1\times10^{-2}$.

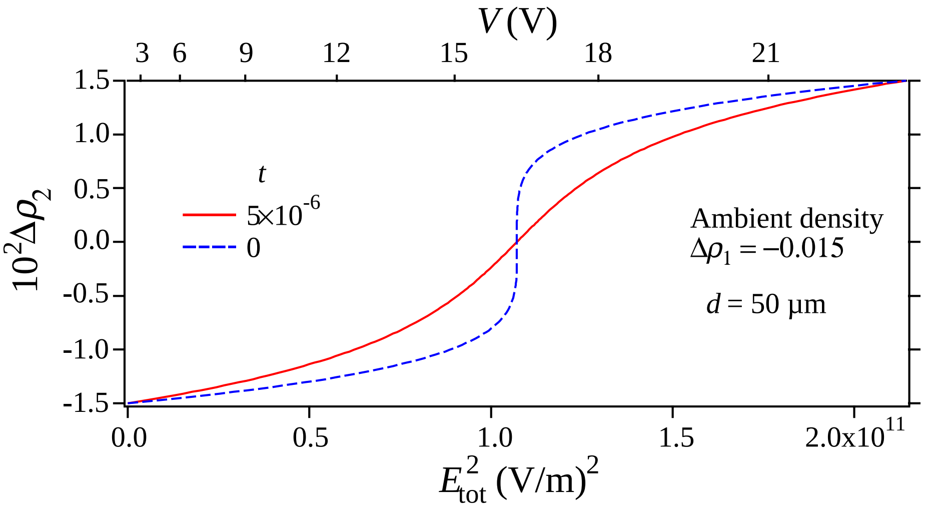

Fig. B8. Measured density change versus applied total electrical field squared in a capacitor with a 50 µm gap for $t = 5\times10^{-6}$ and $t = 0$. The predicted isotherms contain an inflection point corresponding to $\rho_2 = \rho_c$.

Appendix C Density Stratification

In this appendix we discuss additional causes of density stratification within the measurement cell that can lead to errors in experimental measurements. We have already discussed the effects of the gravity induced density gradient (see subsection 1.2) and the effects of a temperature gradient (see subsection 3.7). In this Appendix we investigate surface induced density profiles associated with van der Waals forces and the diverging correlation length. The diverging correlation length leads to two different effects. One is from the boundary condition of order parameter and the other is from the confinement of a fluid in a narrow gap. The resultant density profiles associated with these effects can produce significant errors in susceptibility measurements close to T_c performed by the electrostriction technique discussed in Appendix B. These density profiles lead to smaller error (~ 0.1% at $t = 10^{-6}$) in the measurement of the heat capacity at constant volume. We will also present an analysis of a typical microgravity heat capacity measurement along the critical isochore in the single-phase region. This analysis will estimate the maximum accumulative density stratification generated by the temperature steps required for the heat capacity measurements.

Influence of Surface Interactions and Finite Size Effects on Susceptibility Measurements

We have both an experimental and theoretical plan for addressing the influence of surface interactions on the MISTE susceptibility measurements performed using the electrostriction technique. In this technique, measurements are performed in a small capacitance gap where surface effects can account for a non-negligible contribution to the measured susceptibility. We are developing theoretical approaches to calculate surface interaction contributions so that our experimental measurements can be corrected for these effects.

The theoretical analysis of surface interactions given below indicates that the measured susceptibility using electrostriction consists of three contributions. The first one (van der Waals) is from a high density (dead) layer next to each plate, a second one (correlation length) is associated with the boundary condition of the order parameter), and a third one (finite size) is due to the confinement of the bulk fluid in the middle. The finite size effect contribution is found to be completely negligible for this experiment. For the first two cases, the fractional difference between the measured susceptibility, χ_T, and the bulk susceptibility, χ_T^B, is proportional to a boundary layer thickness scaled by the capacitor gap, d. As T_c is approached, the boundary layer thickness grows, and the difference between χ_T and χ_T^B increases. For a capacitor gap of 50 μm and at a reduced temperature $t = 10^{-6}$, the boundary layers caused by the van der Waals force and the diverging correlation length are estimated to cause a ~5% and ~6% maximum fractional error in the susceptibility respectively.

One way of minimizing these errors is to increase the size of the capacitor gap. We plan to have two density sensors with 50 and 150 μm capacitor gaps for the flight experiment. The use of a 150 μm capacitor gap should reduce these surface interaction errors by a factor of three (i.e., ~1.7% for van der Waals and ~2% for correlation length). An advantage of having two different size capacitors is that boundary effects associated with both van der Waals and diverging correlation length can be corrected experimentally. Our theoretical analysis shows that the dead layer thickness does not depend on the capacitor gap. Therefore, its effect can be determined from the measurements by using two capacitors of difference gap sizes. Combining these experimental and theoretical approaches should allow us to perform accurate isothermal susceptibility measurements to a reduced temperature $t \approx 10^{-6}$.

Experimental Minimization of Surface Effects

Here we describe how to calculate the dielectric constant of a bulk fluid by using two capacitors with gaps of d_1 and d_2. When the dielectric constant varies across the gap, d, of a parallel plate capacitor, the total capacitance is

$$\frac{1}{C} = \frac{1}{C_0} \int_0^1 \frac{d\tilde{z}}{\varepsilon(\tilde{z})}, \tag{C1}$$

where C_0 is the empty cell capacitance, and $\tilde{z}$ is the distance from one boundary scaled by the gap d. Assuming that the dead layer has a thickness of δ and dielectric constant of ε_S, then Eq. (C1) becomes

$$\frac{1}{C} = \frac{1}{C_0}\left[\frac{2\delta}{\varepsilon_S d} + \frac{1-2\delta/d}{\varepsilon_B}\right] = \frac{1}{\varepsilon_B C_0}\left[1 + \frac{2\delta}{d}\left(\frac{\varepsilon_B}{\varepsilon_S} - 1\right)\right], \tag{C2}$$

where ε_B is the dielectric constant of the bulk fluid. Since the dead layers are the same, δ and ε_S are the same for the two capacitors. We can further assume ε_B to be the same when the electrical field is the same within the capacitor gaps. By eliminating the dielectric constant of the dead layer from Eq. (C2) for each capacitor, we obtain

$$\varepsilon_B = \frac{\dfrac{d_1}{d_2} - 1}{\dfrac{d_1}{d_2}\dfrac{C_{10}}{C_1} - \dfrac{C_{20}}{C_2}} = \frac{2}{3\dfrac{C_{10}}{C_1} - \dfrac{C_{20}}{C_2}}\ , \tag{C3}$$

where we have chosen $d_1 = 3\,d_2$. Therefore, we can correct for the boundary layers associated with van der Waals and diverging correlation length effects.

For a first order approximation, we can explicitly write the measured susceptibility as

$$\chi_T = \left(1 - \frac{2\delta}{d}\right)\chi_T^B + \frac{2\delta}{d}\chi_T^S\ , \tag{C4}$$

where χ_T^S is the surface contribution. This expression can be simplified to give

$$\chi_T = \chi_T^B\left[1 - \frac{2\delta}{d}\left(1 - \frac{\chi_T^S}{\chi_T^B}\right)\right]. \tag{C5}$$

By solving Eq. (C4) for χ_T^S and equating for both capacitors 1 and 2, we can solve for χ_T^B, obtaining,

$$\chi_T^B = \frac{\frac{d_1}{d_2}\chi_{T1} - \chi_{T2}}{\frac{d_1}{d_2} - 1} = \frac{3\chi_{T1} - \chi_{T2}}{2} \ . \tag{C6}$$

Here we have again chosen $d_1 = 3\ d_2$. In the case of using electrostriction to measure susceptibility, we have to take into account the fact that the correlation length is density dependent. To make sure that the dead layer thickness is the same, the electrical field will be adjusted to be the same, so that the density change is the same. In reality, both the van der Waals field and the diverging correlation length effect exist in the same boundary, and it is unclear at this stage how they interplay and affect each other. However, Eqs. (C3) and (C6) remain valid as long as the equilibrium thickness of the dead layers resulting from both effects is the same for the two capacitor gaps. Thus we can experimentally correct for these surface effects.

Mean Field Calculation of van der Waals Surface Interactions

It is possible to perform an initial, mean-field-theoretical analysis of the effect of the van der Waals surface interaction on the susceptibility of an $O(1)$ system. The interaction has the same effect as a gravitational field has on a liquid gas system. There is no precedence for this analysis, in that there is no published discussion of a symmetry-breaking field that is localized to the immediate vicinity of the bounding surface of a system, but that is not strictly delta-function-like. In particular, there are no published results relating either to the mean field approximation to the influence, or to the renormalized effect of such a symmetry-breaking field. As it turns out, the mean-field analysis is relatively complicated. In fact, some results cannot be obtained without recourse to numerical methods. Here, we will summarize the results of this analysis, and we will infer a simple formula for the effect of the sort of surface interaction thought to be present in the case of ^{3}He. We will then postulate a renormalized version of the results that we will obtain here. These will form the basis of our estimation of the effect of van der Waals surface interactions on the susceptibility of ^{3}He in the immediate vicinity of its liquid-vapor critical point.

According to standard approaches to the fully-retarded van der Waals interaction between a liquid-vapor system, that interaction has the form [62]

$$\frac{3\hbar c\alpha(0)}{8\pi(x+x_0)^4} \ , \tag{C7}$$

where, in the case of ^{3}He,

$$\begin{aligned}\alpha(0) &= 1.384 \times 0.1483\ \text{Å}^3 \\ &= 0.205\ \text{Å}^3 \\ \hbar &= 10^{-27}\ \text{erg sec} \\ c &= 3\times 10^{10}\,\text{cm / sec}\end{aligned}$$

The quantity $\alpha(0)$ is related to the polarizability of He atoms. The variable x in Eq. (C7) is the distance from the surface, and x_0 is the order of an interatomic distance. The way in which this field enters into the general theory of the critical point of an $O(1)$ system is in the Ginzburg-Landau-Wilson effective Hamiltonian

$$\mathsf{H} = \int \left[\frac{1}{2} \left| \frac{ds(x)}{dx} \right|^2 + \frac{r}{2} s(x)^2 + \frac{u}{4} s(x)^4 - h(x)s(x) \right] dx \ , \tag{C8}$$

where we are assuming that the order parameter,

$$s(x) = \frac{\rho(x) - \rho_c}{\rho_c} \ , \tag{C9}$$

the reduced density, depends only on the distance from the bounding surface. The field $h(x)$ is replaced by the van der Waals interaction in Eq.(C7).

Key portions of the mean field calculation are unavoidably numerical, in that there is no analytical solution to the equations that must be solved in order to obtain a response. However, the strategy of the calculation is fairly straightforward. We start with the mean field equation of state,

$$\begin{aligned} 0 &= \frac{\delta \mathsf{H}}{\delta s(x)} \\ &= -\frac{d^2 s(x)}{dx^2} + rs(x) + us(x)^3 - h(x) - h_0 \ . \end{aligned} \tag{C10}$$

Here, we have added a constant ordering field, which will allow us to calculate the bulk susceptibility, defined as

$$\chi_T^B = \frac{\partial}{\partial h_0} \int s(x) dx dy dz \ . \tag{C11}$$

If the system is infinite in extent, then this extensive quantity, which increases as the system's volume, is also infinite. However, we are interested in the alteration of the susceptibility, which grows as the area. The modification of the susceptibility will ultimately be parameterized in terms of the thickness of a "dead layer." This notion will be developed and defined shortly.

The calculation of the susceptibility proceeds as follows. We begin by solving Eq. (C10) with $h_0 = 0$. This yields an order parameter profile $s_0(x)$. We then introduce an infinitesimal h_0 into the equation of state (C10). The order parameter profile suffers an infinitesimal change $s_1(x)$ in response. The equation satisfied by $s_1(x)$ is

$$\begin{aligned} -\frac{d^2 s_1(x)}{dx^2} + rs_1(x) + 3us_0(x)^2 s_1(x) &\equiv Ls_1(x) \\ &= h_0 \ , \end{aligned} \tag{C12}$$

where the operator L is given by

$$L = -\frac{d^2}{dx^2} + r + 3us_0(x)^2 \ . \tag{C13}$$

The solution to this equation is, symbolically,

$$s_1(x) = L^{-1}h_0 \ . \tag{C14}$$

The susceptibility is the integral of $s_1(x)$, divided by h_0. The alteration of the susceptibility is this integral, minus the integral of the susceptibility as given by the integral of $s_1^0(x)$ divided by h_0, where

$$s_1^0(x) = L_0^{-1}h_0 \tag{C15}$$

with

$$L_0 = -\frac{d^2}{dx^2} + r \ . \tag{C16}$$

The calculations are all carried out in the presence of appropriate boundary conditions. Here, we will assume that Neumann boundary conditions hold at the surfaces of the system. These boundary conditions are termed "special" in the parlance of surface critical phenomena, in that they imply a particular combination of surface parameters, and are, in fact, not expected to be generic to $O(1)$ systems in general. However, these are the boundary conditions for which a surface ordering field has the greatest impact on the bulk susceptibility.

Because of the nontrivial nature of the surface ordering field, the solution of the equation of state (C10) with $h_0 = 0$, and the subsequent solution of the response equation (C12) are both necessary numerical. There are relatively straightforward algorithms for the extraction of solutions to those equations, and they have been utilized in the analysis that follows.

In order to ascertain the effective strength of the surface ordering field associated with the van der Waals interaction, we make use of the following parameters, characteristic of the ^{3}He liquid-vapor critical point.

Parameter	Value of the parameter
Critical density, ρ_c	4.145×10^{-2} g/cm^3
Susceptibility, χ_T	2.25×10^{-10} g sec^2/cm$^5 \times t^{-1.24}$
Correlation length, ξ	2.56×10^{-8} cm $\times\, t^{-0.63}$

Inserting these values into the Ginzburg-Landau free energy, and adjusting them so that the amplitude of the isothermal susceptibility is correct when calculated from the susceptibility of this order-parameter-based model, we end up with the following effective strength of the effective van der Waals surface interaction

$$\frac{1856}{(x+1)^4} \ , \tag{C17}$$

where the expression is now dimensionless, and the length is expressed in "fundamental" correlation length units, 2.56 Å.

The remainder of the calculation makes use of this expression for $h(x)$ in the effective Hamiltonian and the equation-of-state. Before proceeding, we note that it is possible to obtain an exact expression for the modification of the susceptibility of a system in which there is a surface-ordering field of the form

$$h(x) = h_s\,\delta(x), \tag{C18}$$

then the excess susceptibility is given by

$$\begin{aligned}\Delta\chi_T &= \chi_T - \chi_T^0 \\ &= \left[\frac{1}{\sqrt{r^2+2uh_s^2}}+\frac{1}{r}\right]\frac{1}{\sqrt{\frac{1}{2}\left[r+\sqrt{r^2+2uh_s^2}\right]}}-\frac{2}{r^{3/2}}\ .\end{aligned} \tag{C19}$$

Recall that this is the difference between the net change in the order parameter induced by a constant external field that results from the presence of a surface-ordering field. The fractional change in the susceptibility is obtained by dividing this expression by the bulk susceptibility. The end result of this renormalization of the susceptibility is

$$\frac{\Delta\chi_T}{\chi_T^0} = \left[\frac{r}{\sqrt{r^2+2uh_s^2}}+1\right]\frac{1}{\sqrt{\frac{1}{2}\left[r+\sqrt{r^2+2uh_s^2}\right]}}-\frac{2}{r^{1/2}}\ . \tag{C20}$$

As the critical point is approached – that is, as $r \rightarrow 0$ – this correction goes to $-2/r^{1/2}$, or as twice the correlation length, in the mean field approximation ($\xi \propto t^{1/2} \propto r^{1/2}$). This can be interpreted in terms of a "dead layer" in which the order parameter is immobilized by the surface-ordering field. The width of the dead layer saturates at twice the correlation length. Equation (C20) will provide the reference for our calculations. In particular, we will see how the calculated susceptibility modification compares with the asymptotic form 2ξ.

The mean field calculation for the case of a realistic van der Waals surface interaction has been performed, using Eq. (C17) for the magnitude of the effective surface-ordering field. Figure C1 shows the relative change of the susceptibility as a function of reduced temperature. The numerically calculated relative change, shown as solid circles in Fig. C1, can be recast into the following expression,

$$\frac{\Delta\chi_T(t)}{\chi_T^B(t)} = -\frac{4\xi(t)\times 5.6t^{0.1}}{d} = -\frac{2\delta}{d}\ . \tag{C21}$$

The additional power-law dependence on reduced temperature in Eq. (C21) is not anticipated in our approach, but was found to provide an excellent fit to the numerical results over six decades in reduced temperature. We can interpret the above expression in terms of the existence of a "dead layer", the thickness of which is equal to $\delta = 11.2t^{0.1}\xi(t)$, where $\xi(t)$ is the bulk correlation length. Using the expression for the experimental correlation length in the table above, we obtain the following estimate for the width of the dead layer,

$$\delta = 28.6\, t^{-0.53} \ \ \text{Å} \ . \tag{C22}$$

We wish to emphasize that the above expression is essentially phenomenological, in that it is based on a power-law fit to data generated in a numerical mean field calculation. The genesis of this unexpected power-law behavior is currently under study. Early indications are that it ought to hold in general, but results of this investigation are, as yet, preliminary. Figure C2 shows the width of this dead layer, in Angstroms, compared with twice the bulk correlation length, the limiting width of the effective dead layer in the case of a surface ordering field that is confined entirely to the bounding surface, according to a mean field calculation.

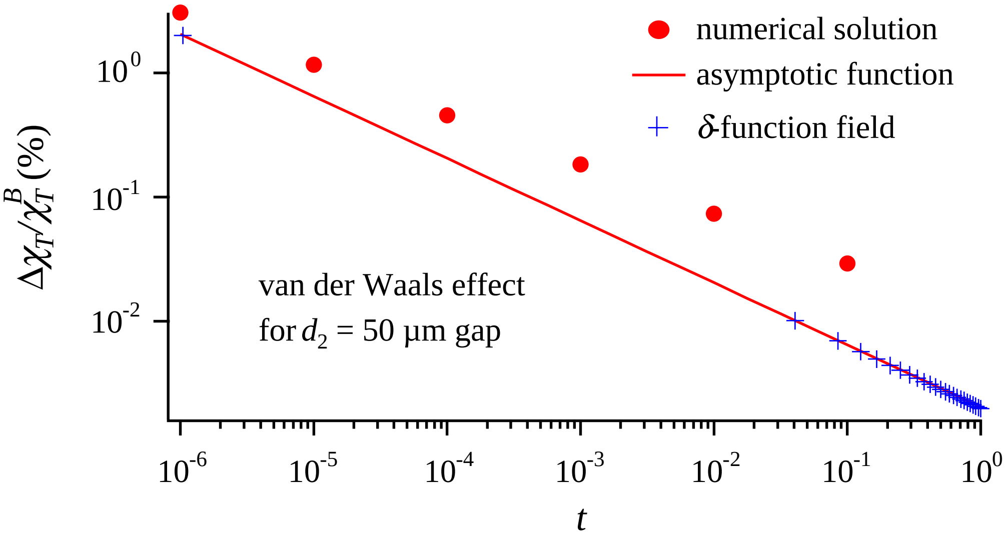

Fig. C1. The relative change in the susceptibility as a function of the reduced temperature. The solid circles are from numerical calculations. The cross is calculated from a δ–function surface interaction, and the solid line is the asymptotic form of the cross.

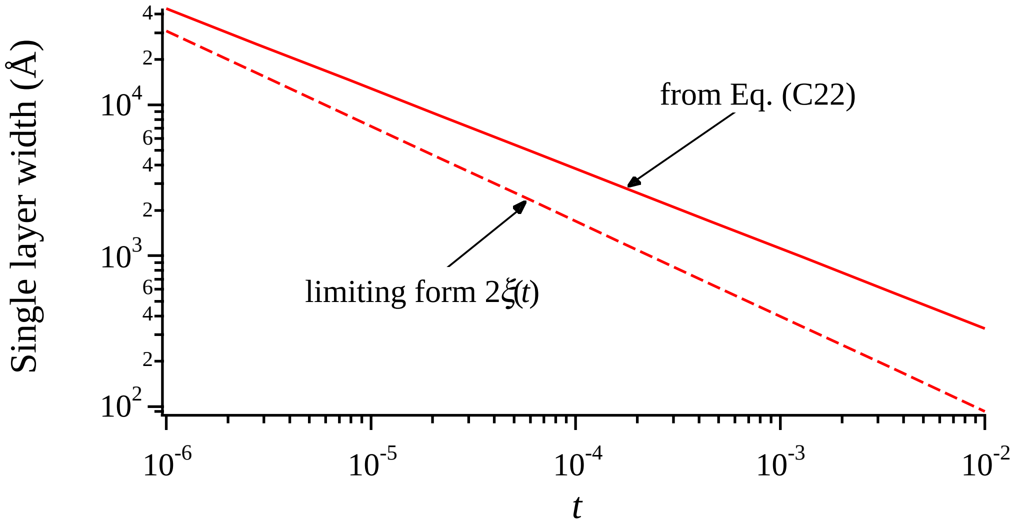

Fig. C2. The width of a single dead layer in Angstroms, as a function of reduced temperature, t, shown as a solid curve. The dashed curve is the size of

The graph in Fig. C2 is summarized in this table:

Reduced temperature, *t*,	Single dead layer width, in Å
10^{-1}	97
10^{-2}	3.25×10^{2}
10^{-3}	1.11×10^{3}
10^{-4}	3.75×10^{3}
10^{-5}	1.27×10^{4}
10^{-6}	4.33×10^{4}

At $t = 10^{-6}$, the dead layer width is about 4.33 μm. The width of the two dead layers at both plates is about 17% and 6% of the 50 and 150 μm capacitor gaps respectively. Therefore, we expect that the fractional changes in the measured susceptibility using the 50 and 150 μm gap capacitors will also be 17% and 6% respectively. These numbers are different from the data shown in Fig. C1 since the experimental correlation length is used for Eq. (C22) while the mean-field expressions are used in Fig. C1. The total dead-layer width is compared with capacitor gaps of 50 and 150 μm in Fig. C3.

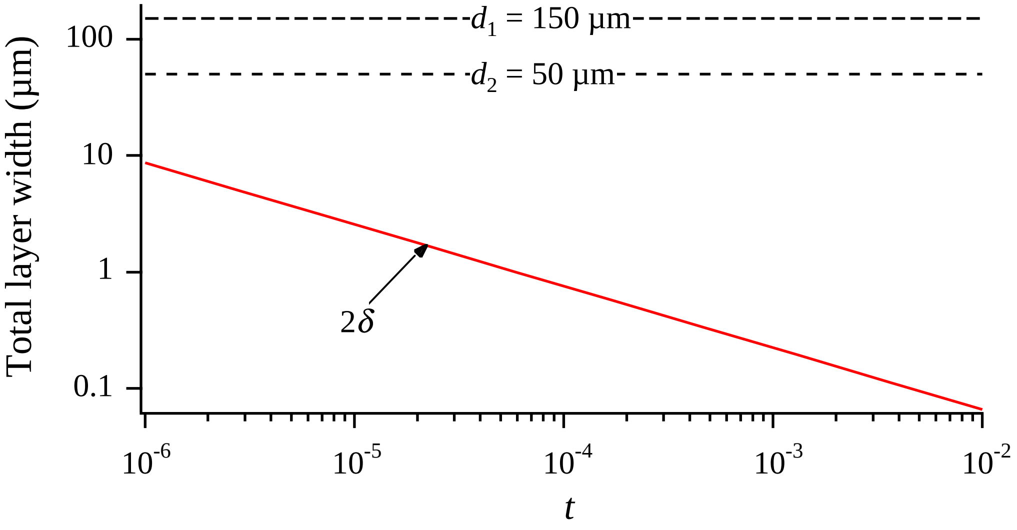

Fig. C3. The total width of the dead layers between capacitor plates, based on the formula in Eq. (C22) versus reduced temperature. For comparison, the two dashed lines are the capacitor gaps of 150 and 50 μm.

In the present calculations, the derived density profile in the dead layer is very large ($\Delta\rho^{*}_{\text{layer}} = \Delta\rho_{\text{layer}}/\rho_c > 100\%$). This large value is inconsistent with the Ginzburg-Landau-Wilson effective Hamiltonian. By introducing a cut-off density, the dead layer thickness will be reduced. We have estimated the effect of a cut-off density by introducing a ϕ^6 term in the effective Hamiltonian. This calculation leads to a thickness reduction of a factor of 1.8 for one dead-layer, which in turn infers that the fractional changes in the measured susceptibility using the 50 and 150 μm gap capacitors will be ~5% and ~2% respectively. Other approaches to determine the cut-off density and the effects of renormalization due to critical point fluctuations will also be the subject of theoretical work in the near future. In addition, we plan to collaborate with Professor Efstratios Manousakis who can perform Monte Carlo calculations that will provide an alternative approach to elucidate boundary layer effects.

Effects due to a Diverging Correlation Length

The diverging correlation length affects the measured susceptibility in two aspects when a narrow gap capacitor is used in the electrostriction technique. The first has to do with the effect of boundary conditions on the order parameter while the second is associated with the confinement of the fluid in a narrow gap where finite size effects become important.

With regard to a "standard" boundary condition, one can perform a mean field theory calculation of the susceptibility in the given mixed boundary conditions of the form

$$\left.\frac{dm(x)}{dx}\right|_{x=0} = cm(0) \; . \tag{C23}$$

The calculation is carried out in much the same way as in the case of the evaluation of the effects of a surface ordering field. One solves the equation of state (C10) with non-zero h_0, but in the absence of a surface field, $h_s(x)$. The susceptibility is the derivative of the integrated order parameter with respect to h_0. Here, the surface has its maximum effect in the limit of Dirchlet boundary conditions ($c \to \infty$). When $c = 0$, the boundary conditions are Neumann, and the susceptibility, in the mean field limit, is unaltered. The general result for the relative change in the susceptibility is

$$\frac{\Delta\chi_T}{\chi_T^B} = -2\frac{\xi}{d}\frac{c\xi}{1+c\xi} \; , \tag{C24}$$

where ξ is the correlation length. This is consistent with a dead layer whose width is equal to $\delta = c\xi/(1+c\xi)$. This width is always smaller than the correlation length, although $c\xi/(1+c\xi) \to 1$ as the critical point is approached.

With regard to the confinement in a small capacitor gap, there is a simple calculation that yields the change in the susceptibility of a region with finite width. Again, making use of mean field theory, and assuming Dirichlet boundary conditions, which maximize the influence of the boundary in the absence of a surface ordering field, we obtain the relative change between the measured and bulk susceptibility,

$$\frac{\Delta\chi_T}{\chi_T^B} = -2\frac{\xi}{d}\tanh\frac{d}{2\xi} \; . \qquad \text{(C25)}$$

Equation (C25) can be interpreted as the combined effects of boundary conditions, $2\xi/d$, and confinement, $\tanh(d/2\xi)$. In the limit of infinite width, Eq. (C25) displays the result of there being two dead layers with a thickness equal to the correlation length, one at each bounding surface. The confinement effect is proportional to $1 - \tanh(d/2\xi)$, which vanishes as $2\exp(-d/\xi)$ for large d/ξ. This gives us a means for gauging the possible relevance of finite size effects to the analysis of MISTE data. At $t = 10^{-6}$, the correlation length is about 1.54 µm. This is to be compared with a width of 50 µm for the smaller capacitor gap. The fractional influence of finite size effects will be on the order of 2×10^{-15} and is effectively infinitesimal for a gap of 50 µm. Therefore, we conclude that the confinement by the capacitor gap will not give rise to complications in the experiment as presently configured. However, the effect of the boundary condition will cause errors in the measured susceptibility. In Fig. C4, we plot the relative change in the measured susceptibility, calculated from Eq. (C25), versus reduced temperature. At $t = 10^{-6}$, the boundary condition effect will lead to about 6% and 2% errors for capacitor gaps of 50 and 150 µm respectively. In reality, the parameter c is finite, and thus the dead layer will be smaller than the correlation length, leading to errors smaller than shown in Fig. C4. We are planning to perform a more precise calculation of this effect in the near future.

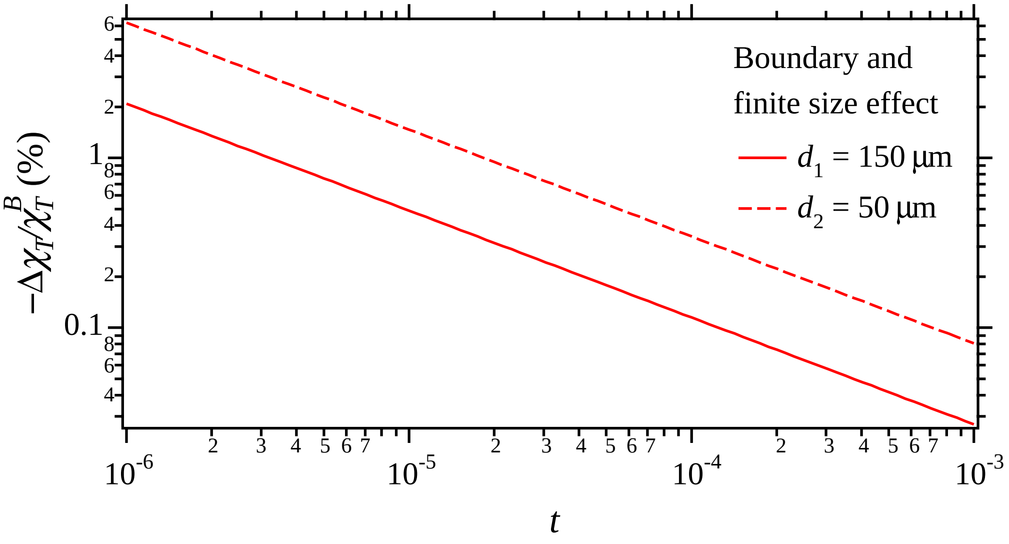

Fig. C4. The relative changes in measured susceptibility versus reduced temperature. The calculation is based on Eq. (C25).

Influence of Surface Interactions and Finite Size Effects on Heat Capacity Measurements

Finite size effects in the heat capacity can be estimated by using the Gaussian approximation formula for the entropy. According to this approximation, the entropy is given by

$$\sum_{\vec{q}} \frac{1}{r+q^2} \ , \tag{C26}$$

where r is the inverse square of the correlation length in the Gaussian approximation. The sum is over the allowed values of the wave vector $\vec{q}$. By assuming a slab geometry where the slab width is d, the allowed values parallel to the slab will be continuous, while the allowed values of the component of the wave vector perpendicular to the walls around it will be given by

$$q_x = \frac{n\pi}{d} \ , \tag{C27}$$

where n is an integer not equal to zero. The reason that q_x is not allowed to be zero is that Dirichlet boundary conditions are assumed, requiring the mode to have the form sin $q_x x$ in the x-direction. The sum in Eq. (C26) is performed by first doing the portion of it that is over n. Making use of standard summation tricks, the sum of interest is

$$\sum_{n=1}^{\infty} \frac{1}{r+Q^2+\left(\frac{n\pi}{d}\right)^2} = \frac{d}{2\sqrt{r+Q^2}} \frac{1}{\tanh\left(\sqrt{r+Q^2}\,d\right)} - \frac{1}{2\left(r+Q^2\right)} \ , \tag{C28}$$

where Q is the wave vector component parallel to the slab. The difference between the first term on the right hand side of Eq. (C28) and its $d = \infty$ limit is the finite size correction that is exponentially small. The second term is the surface interaction correction to the specific heat. In the following we will consider the two contributions separately. First, we look at the confinement effects. The evaluation of this contribution to the change in the entropy of the slab system involves the summation, actually the integration, over the wave-vector Q. By performing the sum over parallel components of the wave vector, the difference mentioned above is given by

$$\int d^{d-1}Q \frac{1}{\sqrt{r+Q^2}} \left(\frac{1}{\tanh\left(\sqrt{r+Q^2}\,d\right)} - 1 \right) . \tag{C29}$$

The proportionality factors have been left out. The ratio of this difference to the full entropy in the Gaussian approximation is given by

$$\frac{\int d^{d-1}Q \frac{1}{\sqrt{r+Q^2}} \left(\frac{1}{\tanh\left(\sqrt{r+Q^2}\,d\right)} - 1 \right)}{\int d^{d-1}Q \frac{1}{\sqrt{r+Q^2}}} \ . \tag{C30}$$

We are interested in the ratio of the specific heat correction to the full specific heat. To obtain this ratio, the derivatives of the numerator and denominator in Eq. (C30) are taken with respect to the reduced temperature that is proportional to r in the mean-field limit. This leaves the expression

$$\frac{\int d^{d-1}Q\left\{\left(r+Q^2\right)^{-3/2}\left(\frac{1}{\tanh\left(\sqrt{r+Q^2}\,d\right)}-1\right)+\frac{L}{\left(r+Q^2\right)\sinh^2\left(\sqrt{r+Q^2}\,d\right)}\right\}}{\int d^{d-1}Q\left(r+Q^2\right)^{-3/2}}\ . \tag{C31}$$

The denominator can be replaced by the standard leading order expression for the specific heat,

$$\frac{\nu}{\alpha}r^{-\alpha}\ , \tag{C32}$$

where α and ν are the critical exponent of C_V and ξ respectively. As for the numerator, one can obtain an expression that scales properly, while having the form that corresponds to the numerator in Eq. (C31) in the mean field limit. This scaling form is

$$r^{-\alpha}\int_0^\infty\left\{\left(1+y^2\right)^{-3/2}\left(\frac{1}{\tanh\left(\sqrt{1+y^2}\,d/\xi\right)}-1\right)+\frac{L/\xi}{\left(1+y^2\right)\sinh^2\left(\sqrt{1+y^2}\,d/\xi\right)}\right\}dy\ . \tag{C33}$$

This expression implies that the ratio of the finite size correction to the infinite system of the specific heat is

$$\frac{\Delta C_V^{fs}}{C_V}=\frac{\alpha}{\nu}\int_0^\infty\left\{\left(1+y^2\right)^{-3/2}\left(\frac{1}{\tanh\left(\sqrt{1+y^2}\,d/\xi\right)}-1\right)+\frac{L/\xi}{\left(1+y^2\right)\sinh^2\left(\sqrt{1+y^2}\,d/\xi\right)}\right\}dy\ . \tag{C34}$$

This is a complicated expression that is dominated by the exponentially small form exp(–2d/ξ). This term is as small as the corresponding term in the expression for the modification of the susceptibility (see after Eq. (C25)). Figure C5 shows the expected temperature dependence of the heat capacity corrections for the case of slabs having widths of d = 0.005 and 0.0005 cm. As it can be seen in Fig. C5, the finite size heat capacity correction is expected to be extremely small, ~ 0.13% for d = 0.0005 cm and the closest reduced temperature of $t = 10^{-6}$.

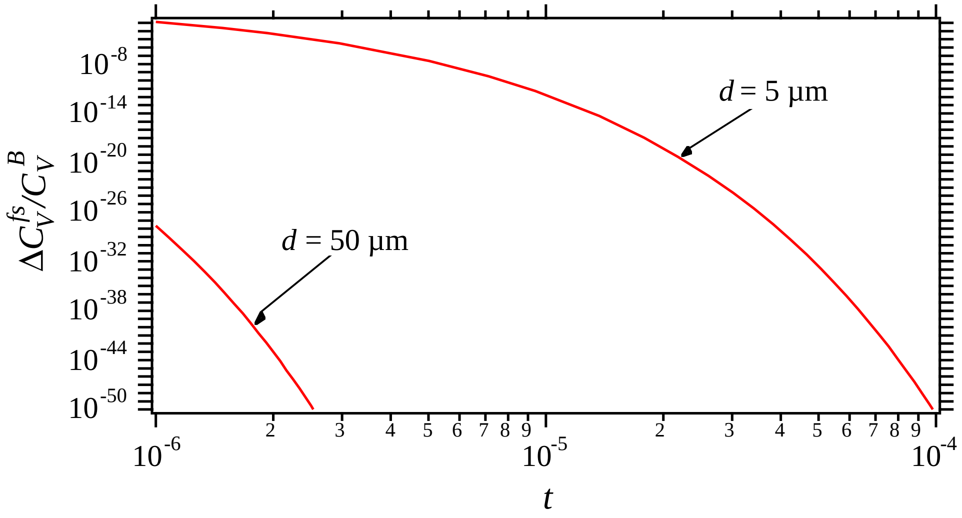

Fig. C5 The ratio of the finite size correction to the bulk specific heat as a function

In the same spirit used in determining the susceptibility change (see Eq.(C5)), we estimate that the expected change in heat capacity due to finite size effects can be given by

$$\frac{\Delta C_V^{meas}}{C_V^B} = \frac{V_{fs}}{V_{\text{tot}}} \frac{\Delta C_V^{fs}}{C_V^B} \ . \tag{C35}$$

The expected slab volume with $d < 0.0005$ cm for the MISTE flight cell is < 0.5% of the total volume. By taking into account the volume ratio using Eq. (C35), this alteration of the measured specific heat is reduced by another factor of 0.005, leading to a negligible correction of 6 ppm.

It is also possible to assess the surface-related reduction in the specific heat. Making use of standard scaling tricks as applied to the last term on the right hand side of Eq. (C28) we find that the ratio of the surface-related reduction in the specific heat to the bulk specific heat is given by

$$\frac{\Delta C_V^{\text{surf}}}{C_V} = \frac{\alpha}{\nu} \frac{\pi}{4} \frac{\xi(t)}{d} \tag{C36}$$

In Figure C6, we display this correction as a function of reduced temperature, t, for $d = 0.05$, 0.005, and 0.0005 cm.

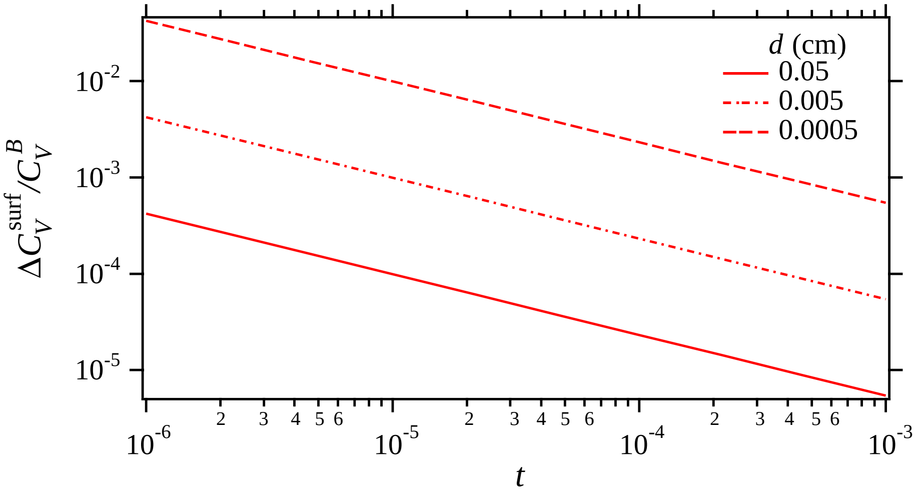

Fig. C6 The ratio of the surface-related reduction in the specific heat to the bulk specific heat for a surface thickness of $d = 0.05$, 0.005, and 0.0005 cm.

The maximum value of the ratio of the surface-related reduction in the specific heat to the bulk specific heat, as given by Eq. (C36) for $d = 0.0005$ cm and $t = 10^{-6}$. For these conditions, the ratio is equal to 4.2%. The expected surface volume within a distance $d < 0.0005$ cm for the MISTE flight cell is ~ 2.4% of the total volume. Again using Eq. (C35) for the case of surface interactions, we see that with the additional factor of 0.024 due to the volume ratio, we are left with a net change in the measured specific heat of 0.1%. This systematic error in the specific heat is less the 1% requirement at $t = 10^{-6}$ for the MISTE flight experiment.

Density Change Associated with Timeline for Typical C_V Measurement

The temperature and density in the MISTE cell will often need to be changed in performing experimental measurements. Near the critical point these changes will lead to a density stratification within the cell that will take a long time to dissipate, as discussed in subsection 3.7. These long equilibrium time constants must be taken into account in developing the experimental timeline for the flight experiment. For heat capacity measurements, we require a density homogeneity < 0.1 %. In this Appendix, we illustrate the expected density distribution in the cell during a typical set of C_V measurements taken along the critical isochore above the transition.

In developing the CVX experiment [32], Berg presented a thermodynamic expression for the maximum density change expected in the interior of a cell, $\Delta\rho_{\text{in}}/\rho_c$, corresponding to a temperature change from T_1 to T_2,

$$\Delta\rho_{in}\big/\rho_c = \left(\partial T^*\big/\partial P^*\right)_V \int_{t_1}^{t_2} C_V^* dT_{\text{wall}} \,. \tag{C37}$$

Here $T^* = T/T_c$, $P^* = P/P_c$, $C_V^* = (T_c/P_c)\rho C_V$ and t_1 and t_2 are reduced temperatures. Substitution of ^{3}He thermodynamic values for $\partial T^*/\partial P^*$ and C_V^*/T^* [27] into this expression gives

$$\Delta\rho_{\text{in}}\big/\rho_c = (1/3.41)\int_{t_1}^{t_2}\left(-0.615+3.56t^{-0.1}\right)(1+t)\,dt_{\text{wall}} \,. \tag{C38}$$

or

$$\Delta\rho_{\text{in}}\big/\rho_c = (1/3.41)\left[-0.615t-0.3075t^2+\left(3.956t+1.87t^2/t^{0.1}\right)\right]_{t_1}^{t_2} . \tag{C39}$$

For a large temperature quench of $t_1 = 6\times10^{-4}$ and $t_2 = 0$, we get $\Delta\rho^*_{\text{in}} = \Delta\rho_{\text{in}}/\rho_c = 0.08\%$ for ^{3}He that is smaller than the required maximum density homogeneity of 0.1 %. The heat capacity measurements will actually be performed at a large number of reduced temperatures as T_c is approached from above. The experimental cell will remain at each temperature until thermal equilibrium is approximately reached. The density stratification induced by each temperature change will be relaxing during the equilibration time. The accumulated equilibration times will lead to a total density inhomogeneity that is less than 0.08% determined from a one-shot quench.

A detailed time line for the C_V measurements in the single-phase region is being prepared to clearly determine the expected density stratification. We are also developing advanced modeling programs to estimate the expected equilibration time and the remaining density inhomogeneity for the C_V measurements using a pulse technique in the two-phase region.